공학박사학위논문

정지 비행하는 장수풍뎅이 주변의 유동 특성: 모델링 및 최적화

Flow around a hovering rhinoceros beetle: modeling and optimization

2020 년 2 월

서울대학교 대학원

기계항공공학부

오 세 형

정지 비행하는 장수풍뎅이 주변의 유동 특성: 모델링 및 최적화

Flow around a hovering rhinoceros beetle: modeling and optimization

지도교수 최 해 천

이 논문을 공학박사 학위논문으로 제출함

2019 년 10 월

서울대학교 대학원

기계항공공학부

오 세 형

오세형의 공학박사 학위논문을 인준함

2019 년 12 월

위 원 장 : 송 성진

부위원장 : 최 해천

위 원 : 김 호영

위 원 : 박 형민

위 원 : 이 정일 Jungil Lee

Flow around a hovering rhinoceros beetle: modeling and optimization

Sehyeong Oh
Department of Mechanical & Aerospace Engineering
Seoul National University

Abstract

The aerodynamic characteristics of a hovering rhinoceros beetle are numerically and theoretically investigated. Its wing kinematics is measured using high speed cameras and used for numerical simulation of flow around a flapping rhinoceros beetle in hovering flight. The numerical results show that the aerodynamic forces generated (especially for lift) and power required by the hind wing during a quasi-periodic state are quite different from those during the first stroke. This indicates that the wing-wake interaction significantly affects the aerodynamic performance of the hind wing during the quasi-periodic state. Also, twisting of the hind wing along the wing span direction does not much contribute to total force generation as compared to that of the flat wing, and the role of elytron and body on the aerodynamic performance is quite small at least for the present hovering flight. Based on a previous model (Wang *et al.*, *J. Fluid Mech.*, vol. 800, 2016, pp. 688-719), we suggest an improved predictive aerodynamic model without any ad hoc model constants for a rigid and flat hind wing by considering the effect of the wing-wake interaction in hovering flight. In this model, we treat the wake as a steady or unsteady non-uniform downwash motion and obtain its magnitude by combining

a quasi-steady blade element theory with an inviscid momentum theory. The lift and drag forces and aerodynamic power consumption predicted by this model are in excellent agreements with those obtained from numerical simulations.

Based on the developed quasi-steady aerodynamic model, the optimal planform shapes and motions of the hind wing of the hovering beetle for minimum power consumption are investigated. First, we optimize wing motions with the measured wing planform shape for minimum aerodynamic and positive mechanical power consumptions, respectively. We also optimize wing planform shapes with the measured wing motion, as done for the optimization of the wing motion. We find that the measured wing shape is not optimal in terms of aerodynamic power consumption and the optimal wing shape and motion minimizing positive mechanical power consumption are close to the measured ones. For minimum aerodynamic power consumption, the pitching axis of the wing should be located between the 1/4-chord and the mid-chord points, together with the radius of the first moment of wing area of around 0.5. For minimum positive mechanical power consumption, the wing area should be concentrated near the wing root rather than the aerodynamically optimal wing shape, and the pitching axis is between the leading edge and the 1/4-chord point.

Keywords: rhinoceros beetle, hovering flight, numerical simulation, quasi-steady blade element momentum theory, wing-wake interaction, optimization

Student number: 2014-21560

Contents

List of Figures

Part II Optimal wing geometry and kinematics of a hovering rhinoceros beetle for minimum power consumption

Appendix A

List of Tables

Part I.

A numerical and theoretical study of the aerodynamic performance of a hovering rhinoceros beetle (*Trypoxylus dichotomus*)

This part is based on "**Oh, S.**, Lee, B., Park, H., Choi, H. & Kim, S.-T. 2020 A numerical and theoretical study of the aerodynamic performance of a hovering rhinoceros beetle (*Trypoxylus dichotomus*). *J. Fluid Mech.* **885**, A18".

Chapter 1

Introduction: Why rhinoceros beetle?

Over the last three decades, flying insects have attracted great interest in the engineering and science fields because their length and velocity scales as well as the flight condition are similar to those of micro air vehicles (MAVs) (Shyy *et al.* 2008, 2013; see also Pennycuick (2008)). MAVs have typically a wing span of less than approximately 15 cm and mass of less than 100 g, and thus operate at low Reynolds numbers less than 10^5 (Spedding & Lissaman 1998; Ho *et al.* 2003; Shyy *et al.* 2008, 2013). In this flow regime, the aerodynamic performance of a fixed wing such as the lift-to-drag ratio significantly deteriorates (Lissaman 1983; Shyy *et al.* 2008, 2013), while a flapping flight becomes more efficient due to the unsteady flow mechanisms (Spedding & Lissaman 1998; Ho *et al.* 2003; Shyy *et al.* 2008, 2013). Therefore, the mechanisms of lift generation due to flapping flight of various flying insects such as the fruit fly, bumblebee, hawkmoth, cicada, rhinoceros beetle, and mosquito have been investigated by numerous researchers (Dudley & Ellington 1990; Willmott *et al.* 1997; Dickinson *et al.* 1999; Zheng *et al.* 2013; Le *et al.*

2013; Liu *et al.* 2016; Bomphrey *et al.* 2017). In this study, we focus on a rhinoceros beetle, *Trypoxylus dichotomus*, among various flying insects because it is one of the heaviest insects and has the highest wing loading among the biological flyers that satisfy the weight and size requirements of MAVs: e.g., the mass and wing loading are around 0.72 mg and 2.6 N/m^2 for fruit fly, 0.175 g and 16.2 N/m^2 for bumblebee (Sun & Du 2003), 1.39 g and 7.8 N/m^2 for hawkmoth (Zheng *et al.* 2013), 1.18 g and 11.8 N/m^2 for cicada (Wan *et al.* 2015), and 6 g and 38 N/m^2 for rhinoceros beetle (Lee *et al.* 2015*a*) (see also figure 1.1). Since high wing loading allows a flyer to carry larger payload and higher capacity of fuel, it can increase the range and economy of the mission of the MAVs (Ho *et al.* 2003). However, a flyer having high wing loading may require high weight-specific power or have low agility and maneuverability. Therefore, when designing a beetle-like flapping-wing MAV with high wing loading, optimizing the wing kinematics and geometry is necessary to reduce the energy cost of the flight or to improve the aerodynamic performance while generating sufficiently high wing loading.

For the purpose of optimizing the kinematics and geometry of a flapping wing, a predictive tool, which accurately predicts the aerodynamic performance, is required for a systematic design. Thus, a few aerodynamic models have been developed to predict the aerodynamic characteristics of flapping wings. According to Ansari *et al.* (2006*a*), aerodynamic modelings for flapping flight can be distinguished by three different approaches: steady-state, unsteady, and quasi-steady approaches. Steady-state approaches include actuator disk momentum theory (Ellington 1984*c*) and steady vortex theory (Rayner 1979), and provide information about the time-averaged downwash motion induced by vortical structures around a

flapping wing once a periodic state is reached. However, their applicability is limited when unsteady aerodynamic performance is required. On the other hand, unsteady approaches based on the potential flow condition consider the effects of the leading and trailing edge vortices (LEV's and TEV's, respectively) by applying Kutta-like boundary conditions at both edges (see, for examples, Ansari *et al.* (2006*b*) and Xia & Mohseni (2013)). As noted in Ansari *et al.* (2006*a*), however, the applicability of these boundary conditions is questionable during stroke reversal, because wing pitching motion is so acute that the fluid is more likely to turn around the trailing edge rather than leaving the edge smoothly. Quasi-steady approaches assume that each instantaneous aerodynamic characteristics of flapping wings is taken to be the steady-state solution obtained by fixing the corresponding wing motion in time. However, to improve their prediction performance, most of the existing quasi-steady approaches contain model constants that should be provided *a priori* by experiments or numerical simulations whenever the wing geometry changes (Sane & Dickinson 2002; Berman & Wang 2007; Whitney & Wood 2010; Nakata *et al.* 2015). For this reason, optimizations based on quasi-steady approaches have been limited only for the wing kinematics (Berman & Wang 2007; Zheng *et al.* 2013; Nakata *et al.* 2015). Recently, Wang *et al.* (2016) suggested a predictive aerodynamic model for flapping flight without any model constants by providing them based on theoretical approaches and observations. Nonetheless, their model has a limitation in that it neglects the effects of the fluid viscosity and wing-wake interaction.

Hovering flight in general requires more power than other flight modes because of no ambient wind to aid in lift generation (Berman & Wang 2007). Also, flapping wings in hovering flight interact with their own wake

generated by the previous strokes (Birch & Dickinson 2003; Aono *et al.* 2008), which should be considered in developing a quasi-steady aerodynamic model. So far, the aerodynamic performance of the hovering flight of various species of insects such as the fruit fly, bumblebee and hawkmoth has been extensively studied (Dickinson *et al.* 1999; Wang *et al.* 2004; Berman & Wang 2007; Aono *et al.* 2008; Zheng *et al.* 2013; Nakata *et al.* 2015). However, the hovering flight of a rhinoceros beetle (Truong *et al.* 2013*a*, 2017; Phan *et al.* 2017) has not received much attention compared to other flying insects, and further investigations are needed for understanding its aerodynamic mechanism. Therefore, the objectives of our study are (i) to investigate the aerodynamic characteristics of a hovering flight of a rhinoceros beetle using numerical simulations and (ii) to suggest an improved predictive aerodynamic model of flapping flight in hover without any *ad hoc* model constants. We also examine the aerodynamic role of the elytron (fore wing) and body and the effect of a twisted hind wing along the wing span. In §2, we provide the wing kinematics of a rhinoceros beetle in a hovering flight. The numerical details and results are given in §3 and §4. In §5, we suggest an improved predictive aerodynamic model of a flapping wing in hover, based on the previous model of Wang *et al.* (2016), by combining a quasi-steady blade element theory with a momentum theory to include the effect of the wing-wake interaction. This predictive model is validated by comparing the results with those from numerical simulation in §6 and §7, followed by conclusions in §8.

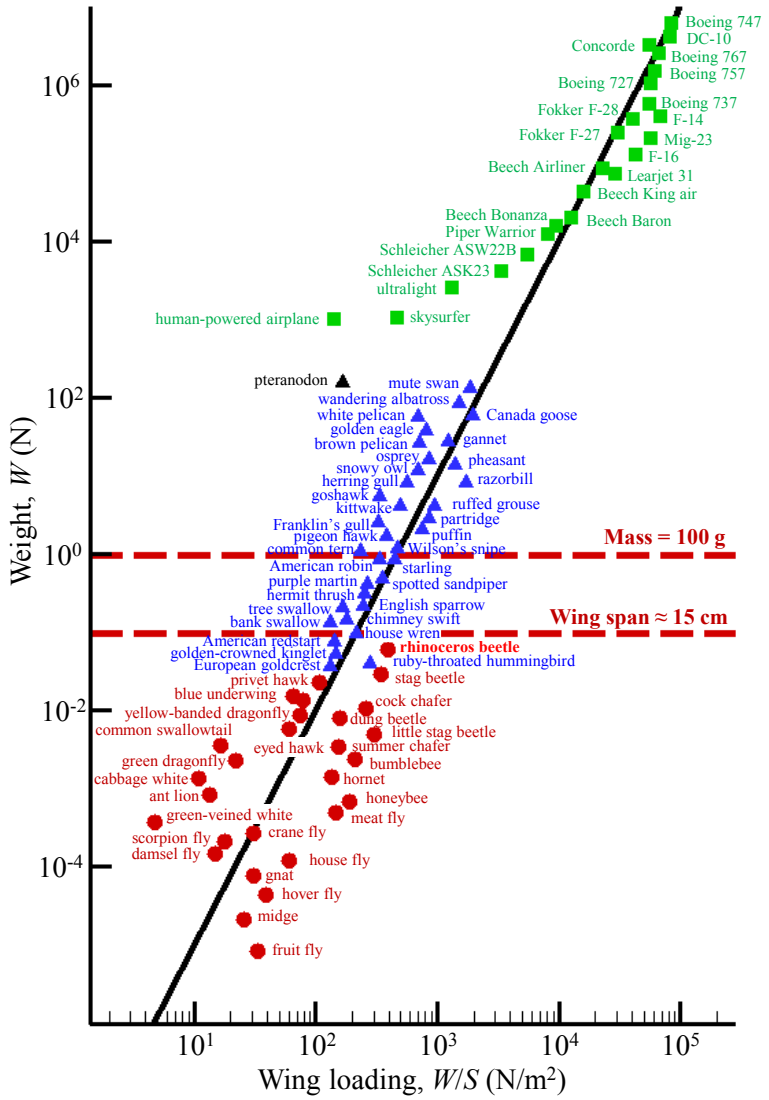

FIGURE 1.1. Wing loading and weight of various flyers from flying insects to commercial airplanes. The solid line is a fit line to the data for $W/S \sim W^{1/3}$. Two dashed lines separate light flyers ($W \leqslant 0.98$ N) from heavy ones, and flyers having short wing span ($\leqslant 15$ cm) from those having long wing span, respectively. Circles, triangles and squares indicate flying insects, birds (including pteranodon), and artificial flyers, respectively. Modified from Tennekes (1996).

Chapter 2

Wing kinematics and morphological parameters

2.1. Measurement of the wing kinematics

Experimental arrangements are the same as those of Lee *et al.* (2015*a*). A hovering flight of a *Trypoxylus dichotomus* is filmed in a customized studio frame (2 m $\times$ 2 m $\times$ 2 m) with three high-speed cameras (NX5-S2 MONO, Integrated Design Tools, Inc.) having maximum spatial resolution of 2336 $\times$ 1728 pixels at maximum sampling rate of 730 fps, as shown in figure 2.1(a). One camera is located on the top and the others are located at the sides of the frame. Also, two 2 kW-halogen portable lights are used for illumination. These cameras capture the images during two seconds at the rate of 2000 fps with a spatial resolution of 512 $\times$ 512 pixels and operate simultaneously via a synchronizer (miniHUB, Integrated Design Tools, Inc.). The sequential image analysis is used to separate captured images of the hovering beetle during two consecutive periods. We use seventeen soft markers that are morphologically discernible features to let the beetle fly without any external disturbance instead of

using hard markers. Figure 2.1(b) shows selected markers including three on the body, four on the right elytron and ten on the right hind wing. The cross-correlation of pixels is performed across the acquired image sequences, known as visual image correlation method, to track the soft markers (Hedrick 2008). With the visual image correlation method, we use modified direct linear transform (MDLT) algorithm for the reconstruction of three-dimensional wing kinematics (Hatze 1988; Hedrick 2008).

Figure 2.1(c) shows the measured body displacement in X- and Y-directions, where X- and Y-directions indicate the frontal and anti- gravitational directions, respectively. Also, linear regression lines are plotted to roughly estimate the mean velocity for both directions. With the least square method, the mean velocity is 0.14 and -0.05 m/s in X- and Y-directions, respectively. The advance ratio J is defined as the ratio of the forward velocity to the mean velocity of wing tip $U_h = 2\Phi_h f R_h$ (Ellington 1984*b*) (see also table 2.1), and the flight of $J < 0.1$ is regarded as a hovering flight. From the measured data, $J \approx 0.01$ and the motion in the vertical direction is much slower than that in the frontal direction. Thus, it is reasonable to assume that the present wing motions measured are indeed those of the hovering beetle.

2.2. Measured wing kinematic and morphological parameters

Wing motions of a hovering rhinoceros beetle (*Trypoxylus dichotomus*) are measured as described in the previous section, and their kinematics are averaged over two flapping periods. Figure 2.2 shows the wing kinematic parameters and coordinates, which are defined in a conventional way as done in Willmott & Ellington (1997), Fry *et al.* (2005), Aono

et al. (2008), and Zheng *et al.* (2013). The (X, Y, Z) coordinate is fixed at the shoulder of the right hind wing. The (X, Z) plane is the horizontal plane perpendicular to the gravity direction, and the Y-axis is opposite to the gravity direction. The X-axis is the forward direction and the Z-axis is the right lateral direction. The stroke plane angle (β) is defined as the angle between the horizontal (X, Z) and stroke planes, where the latter is the plane connecting the locations of the shoulder and wing tip at the ends of downstroke and upstroke. The (x_s, y_s, z_s) coordinate is defined such that y_s is the direction normal to the stroke plane, $z_s = Z$, and x_s is in compliance with the right hand rule. This coordinate is transformed to the (x, y, z) coordinate co-rotating with the wing by three consecutive rotations (sweeping, out-of-plane deviation, and pitching motions), where x, y, and z axes indicate the wing thicknesswise, chordwise, and spanwise directions, respectively. Here, the sweeping angle (ϕ) is defined as the angle between z_s-axis and the projection of z-axis on the stroke plane. The angle between the stroke plane and z-axis is defined as the out-of-plane deviation angle (θ). Finally, the pitching angle (η) is the angle of rotation about z-axis.

Figure 2.3 shows the measured wing kinematics of the right hind wing and elytron. To obtain smooth changes in the angular accelerations, all angles in time are connected using periodic quintic splines (Schurer 1968). The flapping frequencies for both wings are $f(= 1/T) = 37.04$ Hz, and the body inclination angle is 85.9° with respect to the horizontal plane (X, Z). The stroke plane angles for the hind wing and elytron are $\beta_h = 2.25^\circ$ and $\beta_e = 10.15^\circ$, where the subscripts of h and e denote the hind wing and elytron, respectively. The elytron moves in phase with the hind wing, but the sweeping amplitude of the hind wing ($\Phi_h = 175^\circ$) is about 5.6 times

that of the elytron ($\Phi_e = 31.3^\circ$). It is observed that both wings become closest to each other at $t/T \approx 0.37$ and 0.63, where $t/T = 0$ corresponds to the start of the upstroke. Also, the sweeping motions of both wings are almost simple harmonic. Therefore, the durations of both the upstroke ($0 \leqslant t/T \lesssim 0.5$) and downstroke ($0.5 \lesssim t/T \leqslant 1$) are nearly identical. Since the hind wing is highly flexible but the elytron is almost rigid, the pitching angles of the hind wing at four different spanwise positions ($r_h/R_h = 0.1, 0.3, 0.6$ and 0.9) are measured, but that of the elytron is measured only at the mid-span ($r_e/R_e = 0.5$), where r and R are the spanwise distance from the wing root (see figure 2.4) and the wing length (root to tip), respectively. The pitching motion of the hind wing is qualitatively similar to those of other insect wings measured by previous studies (Jensen 1956; Vogel 1967; Ellington 1984*b*). Although there are some humps in the pitching angles that may be associated with passive pitching motion due to the air-wing interaction, the pitching angle at each spanwise position remains roughly constant during most of the half stroke but rapidly changes near the start and end of the half stroke. At the end of upstroke ($t/T \approx 0.5$), $\eta \approx 0^\circ$ (indicating a symmetric rotation), whereas η is already positive at the end of downstroke ($t/T = 1$) (indicating an advanced rotation) (Dickinson *et al.* 1999). Also, the pitching amplitude near the wing tip is much larger than that near the wing root, indicating that the hind wing is significantly twisted during the stroke. When we define the amount of wing twist as the difference in the pitching angles at $r_h/R_h = 0.1$ and 0.9, the amounts of the hind wing twist are about 25° and 15° during most of the upstroke and downstroke, respectively. A similar amount of wing twist ($10 \sim 20^\circ$) was found for some other insects (Ellington 1984*b*). On the other hand, the pitching amplitude of

the elytron is much smaller than that of the hind wing and remains nearly constant ($\eta \approx -15^\circ$) throughout the full stroke. For both wings, the out-of-plane motions are negligible ($\theta \approx 0^\circ$).

For comparison, the sweeping and pitching (at $r_h/R_h = 0.6$) angles of a hind wing measured by Truong *et al.* (2011) are also provided in figure 2.3(a). In their study, the measured flapping frequency was about 37.7 Hz, which is almost the same as that of the present study ($f = 37.04$ Hz). The present sweeping motion (ϕ) of the hind wing is in an excellent agreement with that of Truong *et al.* (2011), and the present pitching angle (η) reasonably agrees with that of Truong *et al.* (2011). Note, however, that the present stroke plane angle of the hind wing ($\beta_h \approx 2.25^\circ$) is quite different from that ($\beta_h \approx 30^\circ$) of Truong *et al.* (2011). This might be caused by the difference between the body inclination angle of the present study and that of Truong *et al.* (2011).

To measure the morphological parameters of the beetle whose wing kinematics are recorded, the hind wing and elytron are detached from the body. The body and elytron are three-dimensionally scanned, but only the planform geometry is measured for the hind wing (see figure 2.4). Table 2.1 summarizes the measured morphological and kinematic parameters. The mean chord lengths, wing lengths, aspect ratios, and mass of the hind wing and elytron are $\bar{c}_h = 15.5$ mm and $\bar{c}_e = 16.1$ mm, $R_h = 51.2$ mm and $R_e = 34.0$ mm, $AR_h = 3.30$ and $AR_e = 2.11$, and $m_h = 60$ mg and $m_e = 80$ mg, respectively, where $AR = R/\bar{c}$. The total mass (including legs) and body length are $m = 5.94$ g and $l_b = 49.7$ mm. The Reynolds number is $Re = U_h\bar{c}_h/\nu = 12000$, where $U_h(= 2\Phi_h f R_h)$ is the time-averaged velocity of the hind wing at the tip and ν is the kinematic viscosity of air.

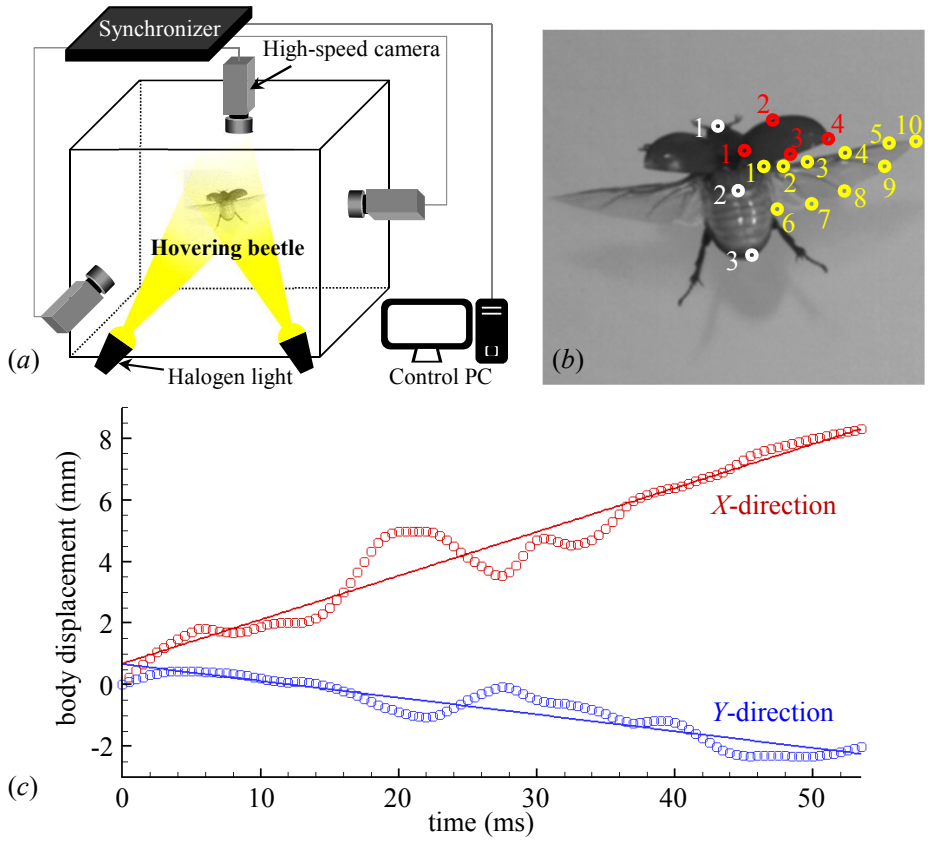

FIGURE 2.1. Measurement of the wing and body motions of a hovering rhinoceros beetle: (a) experimental setup; (b) distribution of morphological markers; (c) body displacement. In (b), white, red and yellow circles indicate tracking points on the body (1: mouth; 2: mass center; 3: pygidium), right elytron (1: shoulder; 2: leading edge at mid-span; 3: trailing edge at mid-span; 4: wing tip) and hind wing (1: shoulder; 2-5: leading edges at r_h=0.1R_h, 0.3R_h, 0.6R_h and 0.9R_h; 6-9: trailing edges at r_h=0.1R_h, 0.3R_h, 0.6R_h and 0.9R_h; 10: wing tip), respectively. Linear regression lines are also plotted in (c).

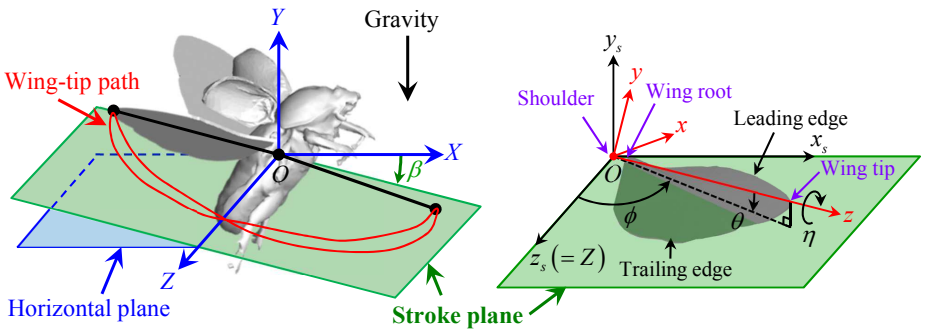

FIGURE 2.2. Wing kinematic parameters and coordinates.

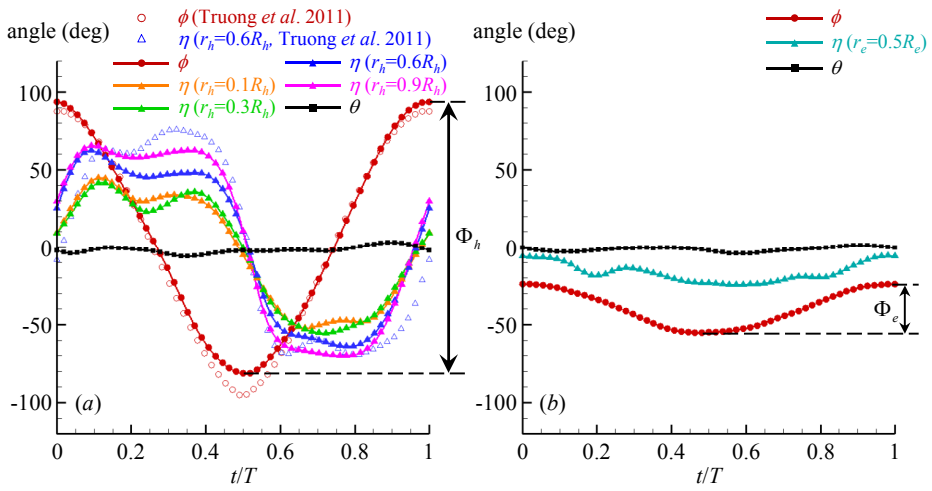

FIGURE 2.3. Wing kinematics measured: (a) hind wing; (b) elytron. In (a), sweeping and pitching angles of a hind wing measured by Truong *et al.* (2011) are also plotted.

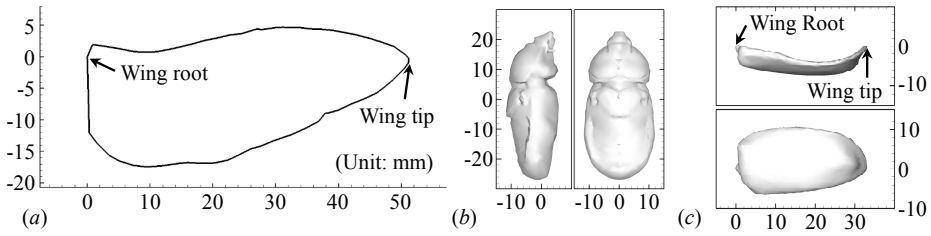

FIGURE 2.4. Wing and body geometries: (a) hind wing (planform view); (b) body; (c) elytron. Here, the legs are removed from the scanned body.

Parameters	Hind wing	Elytron
Stroke plane angle (β)	2.25°	10.15°
Sweeping amplitude (Φ)	175°	31.3°
Mean chord length ($\overline{c}$)	15.5 mm	16.1 mm
Wing length (R)	51.2 mm	34.0 mm
Aspect ratio ($AR = R/\overline{c}$)	3.30	2.11
Mass (m)	60 mg	80 mg
Frequency (f)	37.04 Hz	
Body inclination	85.9°	
Total mass (including legs)	5.94 g	
Body length	49.7 mm	
Mean tip velocity of the hind wing (U_h)	11.57 m/s	

TABLE 2.1. Measured kinematic and morphological parameters.

Chapter 3

Numerical details

For conducting numerical simulations, we use the measured wing kinematics and wing and body geometries shown in figures 2.3 and 2.4. We use an immersed boundary method in an inertial reference frame (Kim *et al.* 2001) to satisfy no slip on the body and wing surfaces. The governing equations for unsteady three-dimensional incompressible viscous flow are

$$\boldsymbol{\nabla} \cdot \boldsymbol{u} - q = 0, \tag{3.1}$$

$$\frac{\partial \boldsymbol{u}}{\partial t} + \boldsymbol{\nabla} \cdot (\boldsymbol{u}\boldsymbol{u}) = -\nabla p + \frac{1}{Re}\nabla^2 \boldsymbol{u} + \boldsymbol{f}, \tag{3.2}$$

where $\boldsymbol{u}$ is the flow velocity, p is the pressure, and q and $\boldsymbol{f}$ are, respectively, the mass source/sink and momentum forcing used for the immersed boundary method (see Kim *et al.* (2001) for the detail). A second-order semi-implicit time advancement scheme (a third-order Runge-Kutta method for the convection terms and the Crank-Nicolson method for the viscous terms) is used for time integration, and the second-order central difference is used for all spatial derivatives. The computations are performed at the maximum CFL number of 1. All variables are nondi-

mensionalized by U_h and $\bar{c}_h$.

The size of the computational domain is $-25 < X/\bar{c}_h < 25$, $-30 < Y/\bar{c}_h < 20$, and $-1 < Z/\bar{c}_h < 30$, where $Z/\bar{c}_h = -1$ corresponds to the symmetry plane at the body centre (see figure 3.1). We apply the Dirichlet boundary condition of $\boldsymbol{u} = 0$ at the outer boundary surfaces and the symmetry boundary condition of $\partial U/\partial Z = 0, \partial V/\partial Z = 0$ and $W = 0$ at $Z/\bar{c}_h = -1$, where U, V and W are the velocity components in the X, Y and Z directions, respectively. Table 3.1 summarizes the details of the grid resolutions and the total number of grids for grid dependence tests. To resolve the flow around the hind wing surfaces, the smallest grids $\Delta_{min}(= \Delta X_{min} = \Delta Y_{min} = \Delta Z_{min})$ are uniformly located at $-3.8 < X/\bar{c}_h < 3.8$, $-2.8 < Y/\bar{c}_h < 1.6$, and $-1 < Z/\bar{c}_h < 3.8$ for grids I and II, but at $-4 < X/\bar{c}_h < 4$, $-3 < Y/\bar{c}_h < 2$, and $-1 < Z/\bar{c}_h < 4$ for grid III, respectively, and stretched grids are used elsewhere: $449(X) \times 289(Y) \times 289(Z)$ with $\Delta_{min} = 0.02\bar{c}_h$ (grid I), $897 \times 577 \times 577$ with $\Delta_{min} = 0.01\bar{c}_h$ (grid II), and $545 \times 381 \times 321$ with $\Delta_{min} = 0.02\bar{c}_h$ (grid III), respectively. For all grids, the flows reach quasi-periodic states after four periods. Figure 3.2 shows the horizontal and vertical force and aerodynamic power coefficients from three different grids, where $C_{F_i} = 2F_i/\rho U_h^2 R_h \bar{c}_h$, $C_{P_{aero}} = 2P_{aero}/\rho U_h^3 R_h \bar{c}_h$, F_X and F_Y are the horizontal and vertical forces, P_{aero} is the aerodynamic power, and ρ is the density of air. These aerodynamic forces and power are evaluated by the method of Lee *et al.* (2011), and are given by

$$\begin{aligned} \frac{\boldsymbol{F}}{\rho U_h^2 \bar{c}_h^2} &= \int_{V_w} \left[-\boldsymbol{f} + \frac{\partial \boldsymbol{u}}{\partial t} + \boldsymbol{\nabla} \cdot (\boldsymbol{u}\boldsymbol{u}) \right] \mathrm{d}V, \\ \frac{P_{aero}}{\rho U_h^3 \bar{c}_h^2} &= -\int_{V_w} \boldsymbol{v} \cdot \left[-\boldsymbol{f} + \frac{\partial \boldsymbol{u}}{\partial t} + \boldsymbol{\nabla} \cdot (\boldsymbol{u}\boldsymbol{u}) \right] \mathrm{d}V, \end{aligned} \tag{3.3}$$

where $\boldsymbol{v}$ and V_w are the wing velocity and control volume enclosing each

isolated wing or body, respectively. As shown in figure 3.2, the results from grids I, II and III are nearly identical, and their differences in the period-averaged horizontal and vertical forces and aerodynamic power from grids I and II are less than 2%. Since grid III has Δ_{min} on a slightly wider area than grids I and II, we hereafter provide results from grid III.

The cross-section of the hind wing at each spanwise location is modelled as a rigid and flat plate with a rectangular shape having the thickness of $0.06\overline{c}_h$ assuming that the aerodynamic effect of wing corrugation is small in hovering flight (Meng *et al.* 2011). Although the hind wing thickness considered is thicker than that of a rhinoceros beetle (the maximum thickness of the vein at the wing base and the average thickness of the membrane of a rhinoceros beetle were measured to be about 715 μm ($0.05\overline{c}_h$) and 3.57 μm ($0.0002\overline{c}_h$), respectively (Jin *et al.* 2009)), a similar wing thickness has been used to investigate the aerodynamic performance of the flapping wings in many previous studies (Sun & Tang 2002; Kweon & Choi 2010; Truong *et al.* 2013*b*). We conduct two additional simulations for case 1 (flat hind wing only) with the wing thickness of $0.02\overline{c}_h$ and $0.04\overline{c}_h$, respectively. The results indicate that the effects of the wing thickness on the force and power are negligible at least for the range of the wing thickness considered.

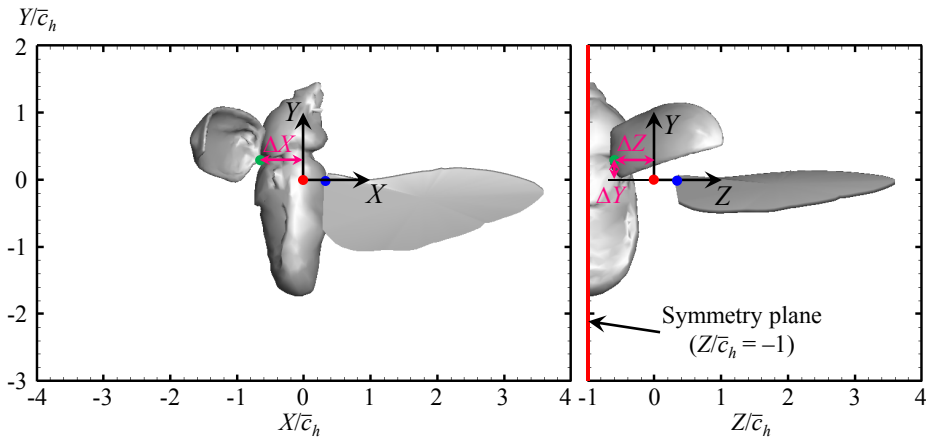

FIGURE 3.1. Body configuration: (left) side and (right) rear views of a hovering rhinoceros beetle having the body inclination of 85.9° with respect to the horizontal plane ($X - Z$ plane). The symmetry plane ($Z/\bar{c}_h = -1$) locates at the centre of the body. The distance between shoulders of hind wing and elytron (denoted as red and green solid circles, respectively) is $\Delta X = 0.65\bar{c}_h$, $\Delta Y = 0.3\bar{c}_h$, and $\Delta Z = 0.6\bar{c}_h$. Note that the shoulder and root locations of the elytron are identical, but those (red and blue solid circles, respectively) of the hind wing are separated by $0.3\bar{c}_h$ (see §4).

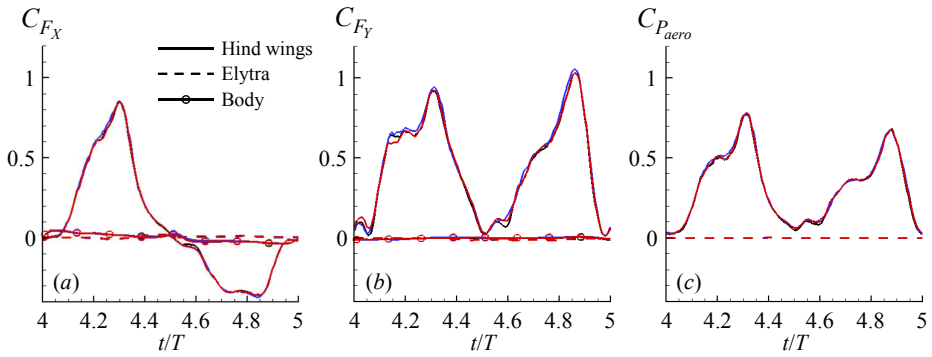

FIGURE 3.2. Results of grid dependence tests for case 3 (see §4): (a) horizontal force coefficient; (b) vertical force coefficient; (c) aerodynamic power coefficient. Blue, black, and red lines denote the results from grids I, II and III, respectively.

	Fine grid region	Grid size	Number of grids
Grid I	[-3.8, 3.8] × [-2.8, 1.6] × [-1, 3.8]	0.02	449×289×289
Grid II	[-3.8, 3.8] × [-2.8, 1.6] × [-1, 3.8]	0.01	897×577×577
Grid III	[-4, 4] × [-3, 2] × [-1, 4]	0.02	545×381×321

TABLE 3.1. Fine grid region. For each grid system, the smallest grids $\Delta_{min}(= \Delta X_{min} = \Delta Y_{min} = \Delta Z_{min})$ are uniformly located at the fine grid region and stretched grids are used elsewhere. Sizes of grid and domain are nondimensionalized by the mean chord length of the hind wing ($\overline{c}_h$).

Chapter 4

Simulation results

In this chapter, we examine the aerodynamic roles of the body, elytron and twisted hind wing using numerical simulation with the wing kinematics and wing and body geometries shown in figures 2.3 and 2.4. We simulate six different cases (see also table 4.1) for rigid flat and twisted hind wings: hind wing only (cases 1 and 4), hind wing and elytron (cases 2 and 5), and hind wing, elytron and half body (cases 3 and 6), respectively. For the twisted hind wing, the pitching angles are measured at $r_h/R_h = 0.1, 0.3, 0.6$ and 0.9, and they are connected using cubic splines for the whole wing span. For the flat hind wing, the pitching angle is constant along the spanwise direction, and its value is taken to be the same as that at r_h/R_h=0.6. For the rigid flat hind wings (cases 1 - 3), the pitching motion is less realistic, and thus a collision occurs between the body and the trailing edge near the root of the hind wing. To avoid this problem, the root of the hind wing is slightly offset by $0.3\bar{c}_h$ from the shoulder (see figure 3.1). This offset is also applied to the cases of the twisted wing (cases 4 - 6). Due to this offset, the tip velocity of the hind wing increases by

the factor of $(R_h + 0.3\bar{c}_h)/R_h$. To keep the wing tip velocity (and thus the Reynolds number) unchanged, the flapping frequency is slightly reduced such as $f' = fR_h/(R_h + 0.3\bar{c}_h)$. Since $R_h = 3.3\bar{c}_h$, the frequency is reduced by about 8.3%. To see how much the aerodynamic forces are changed due to this offset, we compare the results for case 1 with and without the offset. It turns out that the forces are changed by about 10% due to the offset. We also neglect the out-of-plane motions of the hind wing and elytron (i.e., $\theta = 0°$) because they are insignificant, as shown in figure 2.3. One may also wonder if the starting position of a flapping wing affects the aerodynamic performances. To answer this question, we perform an additional simulation starting from downstroke (as opposed to starting from upstroke) for case 3. We find that the aerodynamic performances are changed for first few cycles by a different starting position, but those changes almost disappear in the quasi-periodic state (e.g., at $t/T \geqslant 4$).

As shown in figure 3.2, it is clear that the force and power from the elytron and body are negligible and they almost come from the hind wing. Figure 4.1 shows the instantaneous vortical structures around a hovering rhinoceros beetle model with the rigid flat hind wing (case 3) during the fifth period, together with the contours of the pressure on the suction surface and around the hind wing. At $t/T = 4.125$, the hind wing accelerates backward and a leading edge vortex (LEV) is generated at the suction surface near the hind wing tip where a low pressure region exists (figure 4.1(a)). As time goes by, a wing tip vortex (WTV) is also generated along the hind wing tip path (figures 4.1(b) and (c)). At $t/T = 4.25$, the LEV grows but remains attached on the suction surface of the hind wing, and thus the low pressure region becomes wider (figures 4.1(b)). During the wing deceleration ($t/T = 4.375$), the LEV begins to be shed from

the suction surface very near the hind wing tip (figures 4.1(c)). At the end of the upstroke ($t/T = 4.5$), the LEV on the hind wing is entirely shed from the suction surface near the tip, and this region changes to a high pressure region due to the motion induced by a detached LEV (figure 4.1(d)). Also, an arc-like WTV generates a downwash motion in the wake. Similar vortical structures (LEV and WTV) and pressure fields are observed around the hind wing during the downstroke (figures 4.1(e-h)). On the other hand, the sizes and strengths of vortical structures around the elytron and body are much smaller than those around the hind wing. Accordingly, as shown in figure 4.2, the vortical structures around the hind wing and the pressure field are not significantly affected by the presence of the elytron and body. Therefore, the horizontal and vertical force and aerodynamic power coefficients obtained for cases 1 and 2 are nearly the same as those for case 3 (figure 3.2), indicating that the elytron and body generate negligible aerodynamic forces and require little aerodynamic power compared to those for the hind wing during the hovering flight.

As shown in figure 2.3, the hind wing is twisted and thus the angle of attack varies along the span during flapping. Since we consider $\theta = 0°$, $\alpha = \pi/2 + \mathrm{sgn}(\dot{\phi})\eta$, where $\dot{\phi} = \mathrm{d}\phi/\mathrm{d}t$, $\mathrm{sgn}(\bullet)$ is the signum function (1 and -1 for real positive and negative numbers, respectively, and 0 for zero) (see figures 4.3(a) and (b)). In figures 4.3(c-e), we compare the horizontal and vertical force, and aerodynamic power coefficients of the rigid twisted hind wing with those of the flat one. Here, we consider hind wings only (cases 1 and 4), because the aerodynamic roles of the elytron and the body are negligible. The force and power coefficients of the twisted hind wing are slightly increased and decreased, respectively, as compared to those of

the flat wing. Figure 4.4 shows the instantaneous vortical structures and pressure around the flat and twisted hind wings at $t/T = 4.5$. As observed in figure 4.3(a), the angle of attack of the twisted wing is large near the wing root but smaller near the tip than that of the flat wing. Therefore, the tip vortices are much stronger for the flat wing than those for the twisted wing, whereas the root vortices are stronger for the twisted wing. At this instant ($t/T = 4.5$), however, the angles of attack of the twisted wing are not very different from that of the flat one (see figure 4.3(a)), and thus the difference in the surface pressures of the flat and twisted wings is not large. We further investigate the effect of the wing twist on the time-averaged sectional lift ($\Delta\overline{L}$), drag ($\Delta\overline{D}$) and power ($\Delta\overline{P}_{aero}$). Here, the directions of lift and drag are perpendicular (y_s-direction, figure 4.3(b)) and opposite to the wing moving directions, respectively. Figure 4.5 shows the spanwise variations of the time-averaged ($4 \leqslant t/T < 5$) sectional lift, drag and aerodynamic power coefficients on the wing element ($c\Delta z$) of the flat and twisted hind wings, where $\overline{C}_l = 2\Delta\overline{L}/\rho(z\dot{\phi}_{rms})^2 c\Delta z$, $\overline{C}_d = 2\Delta\overline{D}/\rho(z\dot{\phi}_{rms})^2 c\Delta z$, $\overline{C}_{p_{aero}} = 2\Delta\overline{P}_{aero}/\rho(z\dot{\phi}_{crmc})^3 c\Delta z$, c is the local chord length, $\dot{\phi}_{rms} = (\overline{|\dot{\phi}|^2})^{1/2}$ and $\dot{\phi}_{crmc} = (\overline{|\dot{\phi}|^3})^{1/3}$, respectively. Note that the sectional aerodynamic coefficients are denoted by using lower-case subscripts such as C_l, whereas the total aerodynamic coefficients are by using upper-case subscripts such as C_L. At the wing inner part ($r/R < 0.6$), mainly due to high angles of attack, the sectional lift, drag and aerodynamic power coefficients of the twisted wing are larger (except very near the wing root for the power coefficient) than those of the flat one, whereas they are smaller at the outer part ($r/R \geqslant 0.6$) due to lower angles of attack. Nevertheless, the time-averaged total lift, drag and power are similar to each other.

The mean vertical forces ($\overline{F}_Y$) generated and aerodynamic power ($\overline{P}_{aero}$) required for cases 1 to 6 are given in table 4.1, together with the hovering efficiencies ($\eta_{aero} = \overline{C}_{F_Y}^{3/2}/(\sqrt{2\Phi_h AR_h \cos\beta_h}\,\overline{C}_{P_{aero}})$). The hovering efficiency is defined as the ratio of the ideal Rankine-Froude induced power to the actual aerodynamic power (Ellington 1984*d*; Usherwood & Lehmann 2008). For cases 3 and 6 (hind wings, elytra and body; the flat and twisted wings, respectively), the total vertical forces generated (57.1 and 56.5 mN) are quite similar to the weight of a beetle (58.2 mN), showing less than 3% differences. When we consider the hind wing only (cases 1 and 4), due to the wing twisting, the vertical force is increased by 2.8%, the aerodynamic power is decreased by 2.8%, and the hovering efficiency is increased by 7.1%, respectively, indicating a positive but small effect of the wing twist on the aerodynamic performance. A similar positive effect of the wing twist ha been reported in the previous studies (Truong *et al.* 2013*a*; Phan *et al.* 2017), although the amounts of power reduction were different from the present one owing to different wing kinematics.

The vertical forces and aerodynamic power from the hind wing are very similar to the total magnitudes for all cases. The negligible effect of the elytron on the vertical force generation can be explained by a scaling law (Lee *et al.* 2015*b*): the mean vertical force acting on a flapping wing is scaled as

$$\overline{F}_Y \sim \rho\Phi R^2 f^2 \bar{c}^2 AR \sin 2\alpha \cos\beta/(AR+2). \tag{4.1}$$

With $\Phi_h \approx 5.6\Phi_e$, $R_h \approx 1.51R_e$, $f_h = f_e$, $\bar{c}_h \approx \bar{c}_e$, $\alpha_h \approx 47°$, $\alpha_e \approx 87°$, $\cos\beta_h \approx \cos\beta_e$, and $AR_h \approx 1.56AR_e$ (see §2 and table 2.1), $\overline{F}_Y$ (elytron) $\sim 0.01\overline{F}_Y$ (hind wing) and thus it can be estimated that the motion of the elytron cannot generate a vertical force comparable to that by the

hind wing.

		Vertical force (mN)				Aerodynamic power (mW)				
Case	Wing type	Hind wings	Elytra	Body	Total	Hind wings	Elytra	Body	Total	η_{aero}
1	flat	56.8	–	–	56.8	470.4	–	–	470.4	0.207
2	flat	57.6	-0.79	–	56.9	474.6	-0.63	–	474.0	0.206
3	flat	58.3	-0.91	-0.28	57.1	477.9	-0.65	–	477.2	0.206
4	twisted	58.4	–	–	58.4	457.4	–	–	457.4	0.222
5	twisted	58.1	-0.69	–	57.4	454.9	-0.75	–	454.1	0.218
6	twisted	57.9	-0.96	-0.45	56.5	455.4	-0.71	–	454.7	0.213

TABLE 4.1. Mean vertical force and aerodynamic power averaged over the fifth cycle ($4 \leqslant t/T < 5$), hovering efficiency ($\eta_{aero} = \overline{C}_{F_Y}^{3/2} / (\sqrt{2\Phi_h AR_h \cos\beta_h}\, \overline{C}_{P_{aero}})$).

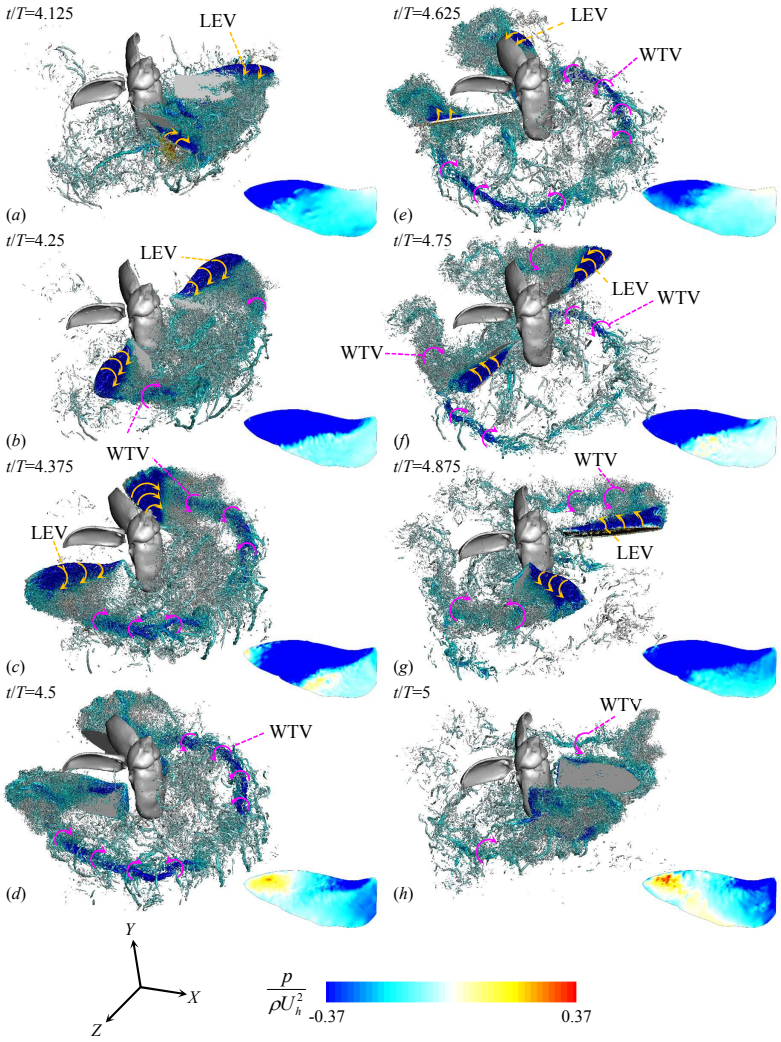

FIGURE 4.1. Development of vortical structures, identified by the iso-surface of $\lambda_2 = -12.34$ (Jeong & Hussain 1995), during the fifth period (flat hind wing; case 3), coloured by the contours of the instantaneous pressure. The instantaneous pressure on the suction surface of the hind wing are obtained by the interpolation method of Kim *et al.* (2018) and its contours are also plotted in this figure. Note that the simulations are conducted with right half of the body and wings. So, the flow fields in the left half in this figure are obtained by mirroring the results in the right half.

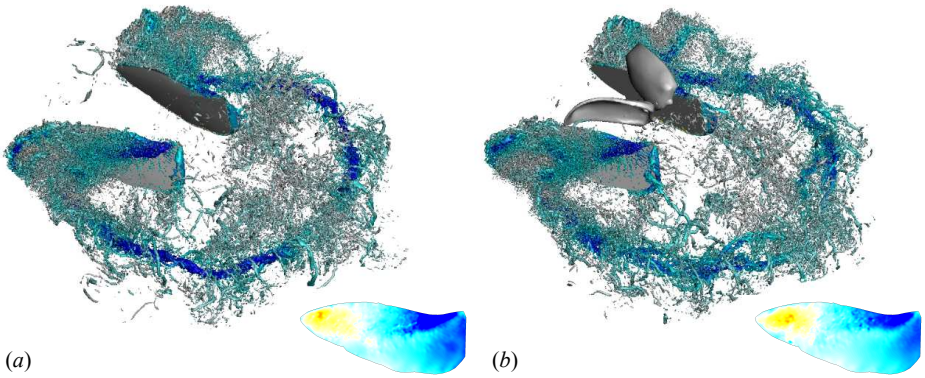

FIGURE 4.2. Effects of the presence of the elytron and body on the vortical structures and pressure around the hind wing at $t/T = 4.5$: (a) hind wing only (case 1); (b) hind wing and elytron (case 2). The contours of the instantaneous pressure on the suction surface of the hind wing are also plotted in this figure. λ_2 iso-surfaces and colour contours are the same as those in figure 4.1. Also, the vortical structures in the left half of the body and wings are from those in the right half as done in figure 4.1.

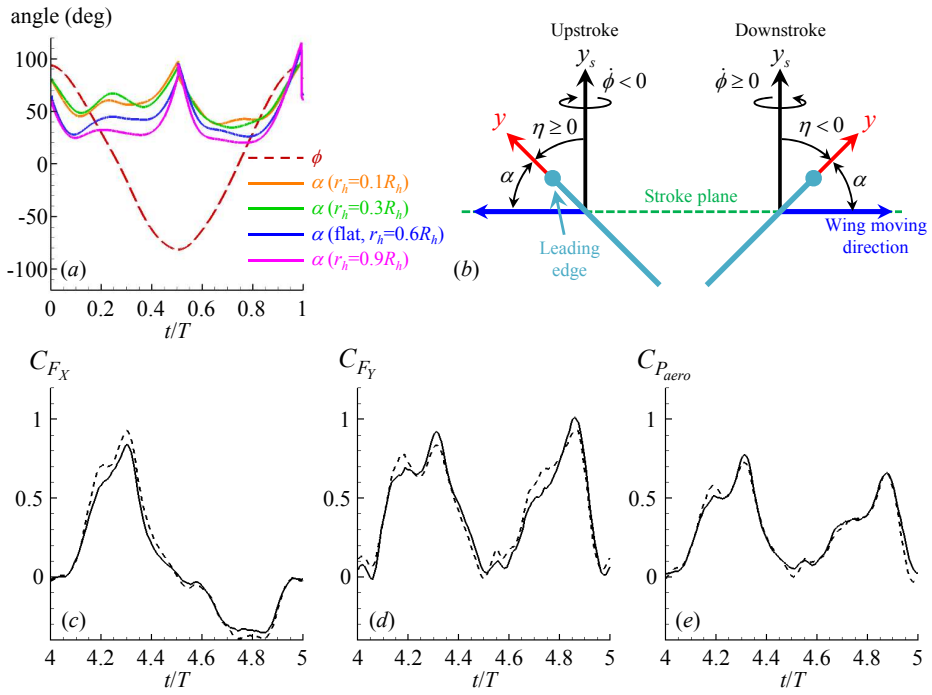

FIGURE 4.3. Angle of attack and aerodynamic force and power coefficients of the rigid flat and twisted hind wings, respectively: (a) angle of attack (α) of the hind wing; (b) definition of α in the absence of deviation motion ($\theta = 0°$); (c) horizontal force; (d) vertical force; (e) aerodynamic power. In (b), a wing cross section is shown in light blue with the leading edge marked with a solid circle. In (c)-(e), ——, flat (case 1); – – –, twisted (case 4).

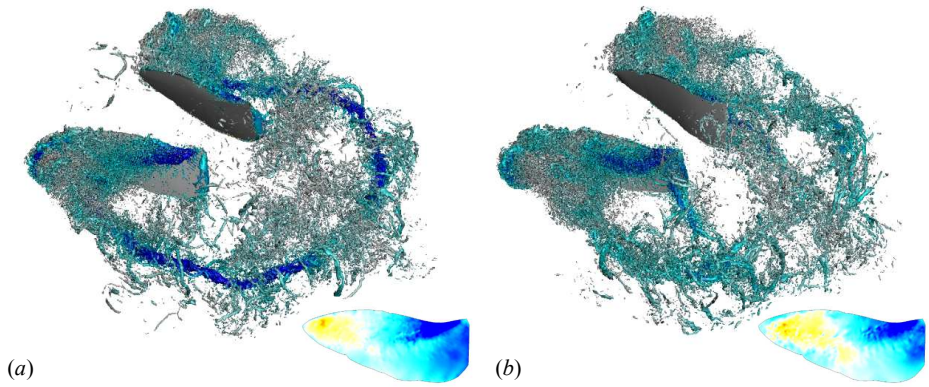

FIGURE 4.4. Instantaneous vortical structures and pressure around the hind wing at $t/T = 4.5$: (a) flat wing (case 1); (b) twisted wing (case 4). The contours of the instantaneous pressure on the suction surface of the hind wing are also plotted in this figure. λ_2 iso-surfaces and colour contours are the same as those in figure 4.1.

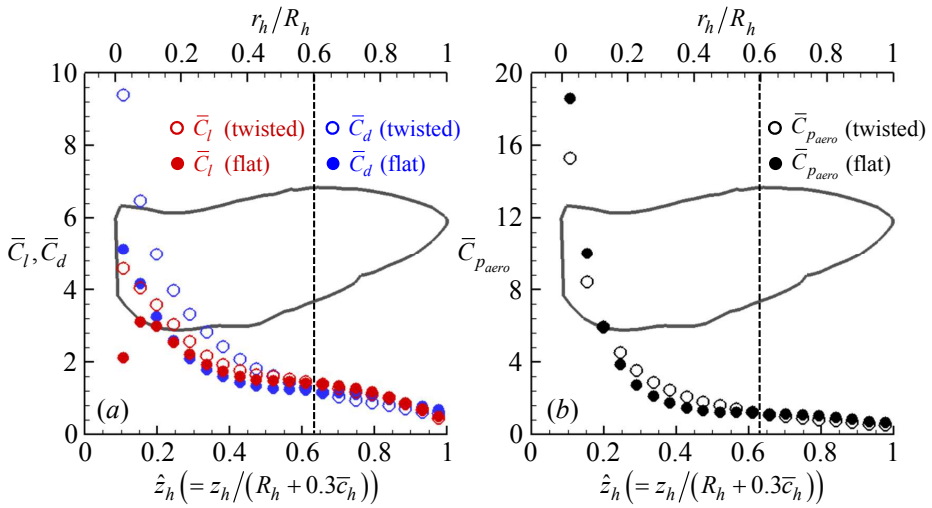

FIGURE 4.5. Spanwise variations of time-averaged ($4 \leqslant t/T < 5$) sectional lift, drag and aerodynamic power coefficients of the flat and twisted hind wings (cases 1 and 4): (a) lift and drag; (b) power. The planform shape of the hind wing is also plotted.

Chapter 5

Quasi-steady aerodynamic model of a flapping wing in hover

In this chapter, we develop an analytical model to predict the aerodynamic force and power by the flapping motion of the hind wing. As we already discussed in §4, the aerodynamic forces by the body and elytron are negligible as compared to those by the hind wing, and thus we do not consider the contributions from the body and elytron in this section. We showed in the previous section that the twisted hind wing produces the sectional aerodynamic force and power different from those of the rigid flat hind wing. Nonetheless, because of difficulties in modelling the aerodynamic force and power of the twisted wing, we consider a rigid flat wing in developing an aerodynamic model. Due to this limitation, the aerodynamic performance of the hind wing of the beetle cannot be fully considered. However, we believe that the present model would aid in capturing essential mechanisms for the force generation and power expenditure of the beetle because the total force generated and power required by the rigid flat hind wing are very similar to those by the twisted hind

wing (although the details of the sectional coefficients are different near the root for two wings). We also assume that the interaction between left and right hind wings is insignificant, and develop an aerodynamic model for single wing considering the symmetry between the left and right wings. We include the effects of the LEV and WTV, wing-wake interaction, wing acceleration and deceleration, wing pitching motion, and wing shape, and suggest a predictive quasi-steady blade element theory combined with the momentum theory. Unless otherwise required, we hereafter omit the subscript h that represents the hind wing.

5.1. Quasi-steady blade element theory

The blade element theory, originally applied to flapping flight by Osborne (1951), has been used to evaluate the force on a flapping wing by dividing it into several elements and integrating their forces over the whole wing (Sane & Dickinson 2002; Berman & Wang 2007; Whitney & Wood 2010; Nakata *et al.* 2015; Wang *et al.* 2016). Figure 5.1 shows the parameters used for the blade element theory. Here, c is the local chord length and d is the position of the leading edge from the pitching axis. The (x, y, z) coordinate is fixed to the wing shoulder, and the offset distance (distance between the wing shoulder and root) is denoted as $l(= 0.3\overline{c}_h)$.

In the absence of the out-of-plane motion ($\theta = \dot{\theta} = \ddot{\theta} = 0$), the wing angular velocity ($\boldsymbol{\omega}$) can be represented as

$$\begin{aligned} \boldsymbol{\omega} &= \dot{\phi}\boldsymbol{e}_{y_s} + \dot{\eta}\boldsymbol{e}_z \\ &= \dot{\phi}\sin\eta\boldsymbol{e}_x + \dot{\phi}\cos\eta\boldsymbol{e}_y + \dot{\eta}\boldsymbol{e}_z, \end{aligned} \tag{5.1}$$

where ϕ is the sweeping angle on the stroke plane, η is the pitching angle, and $\boldsymbol{e}_i$ is the unit vector in i direction. From (5.1), the angular acceleration

($\boldsymbol{\psi}$) is obtained as

$$\boldsymbol{\psi} = \dot{\boldsymbol{\omega}} = (\ddot{\phi}\sin\eta + \dot{\phi}\dot{\eta}\cos\eta)\boldsymbol{e}_x + (\ddot{\phi}\cos\eta - \dot{\phi}\dot{\eta}\sin\eta)\boldsymbol{e}_y + \ddot{\eta}\boldsymbol{e}_z. \tag{5.2}$$

With (5.1) and (5.2), the sectional wing sweeping velocity and acceleration of an infinitesimally thin wing (i.e., $x = 0$ on the wing) at $y = 0$ ($\boldsymbol{v}_s$ and $\boldsymbol{a}_s$, respectively), are obtained as

$$\begin{aligned} \boldsymbol{v}_s &= \boldsymbol{\omega} \times z\boldsymbol{e}_z = z(\omega_y \boldsymbol{e}_x - \omega_x \boldsymbol{e}_y), \\ \boldsymbol{a}_s &= \boldsymbol{\psi} \times z\boldsymbol{e}_z + \boldsymbol{\omega} \times \boldsymbol{v}_s \\ &= z[(\omega_z\omega_x + \psi_y)\boldsymbol{e}_x + (\omega_y\omega_z - \psi_x)\boldsymbol{e}_y - (\omega_x^2 + \omega_y^2)\boldsymbol{e}_z]. \end{aligned} \tag{5.3}$$

When $|\boldsymbol{v}_s| \neq 0$, the angle of attack ($\alpha$) can be defined as

$$\alpha = \arccos\left(\frac{\boldsymbol{v}_s \cdot \boldsymbol{e}_y}{|\boldsymbol{v}_s|}\right) \quad \text{for } 0 \leqslant \alpha \leqslant \pi. \tag{5.4}$$

The wake behind a flapping wing may be approximated by a steady and non-uniform downwash velocity ($\boldsymbol{w}$) normal to the stroke plane as

$$\boldsymbol{w} = -w(z)\boldsymbol{e}_{y_s} \quad (w \geqslant 0). \tag{5.5}$$

When a flapping wing interacts with a non-uniform downwash motion ($\boldsymbol{w}$), the effective sectional wing velocity and angle of attack are given as

$$\begin{aligned} &\boldsymbol{v}_{s,e} = \boldsymbol{v}_s - \boldsymbol{w}, \\ &\alpha_e = \arccos\left(\frac{\boldsymbol{v}_{s,e} \cdot \boldsymbol{e}_y}{|\boldsymbol{v}_{s,e}|}\right) \qquad \text{for } 0 \leqslant \alpha_e \leqslant \pi. \end{aligned} \tag{5.6}$$

With an assumption of no radial force, the required aerodynamic torque ($\mathrm{d}\boldsymbol{\tau}$) and power ($\mathrm{d}P_{aero}$) on a wing sectional element are given by

$$\begin{aligned} \mathrm{d}\boldsymbol{\tau} &= z\mathrm{d}F_y\boldsymbol{e}_x - z\mathrm{d}F_x\boldsymbol{e}_y + y_{cp}\mathrm{d}F_x\boldsymbol{e}_z, \\ \mathrm{d}P_{aero} &= \mathrm{d}\boldsymbol{\tau} \cdot \boldsymbol{\omega}, \end{aligned} \tag{5.7}$$

where $\mathrm{d}\boldsymbol{F}$ is the force on the wing sectional element, and y_{cp} is the location of centre of pressure from the pitching axis.

The sectional aerodynamic force on a flapping wing is decomposed into four different components due to the sweeping (*swp*) and pitching (*pit*) motions, their coupling (*cpl*), and added mass effect (*add*) which is further decomposed into two components owing to the sweeping (*add,1*) and pitching (*add,2*) accelerations, respectively. Then, the aerodynamic force, torque, and power of a flapping wing are given as

$$\begin{aligned}
\boldsymbol{F}(t) &= \int \Big[(\mathrm{d}F_x^{swp} + \mathrm{d}F_x^{pit} + \mathrm{d}F_x^{cpl} + \mathrm{d}F_x^{add,1} + \mathrm{d}F_x^{add,2})\boldsymbol{e}_x \\
&\quad + \mathrm{d}F_y^{swp}\boldsymbol{e}_y\Big], \\
\boldsymbol{\tau}(t) &= \int \big[z\mathrm{d}F_y^{swp}\boldsymbol{e}_x \\
&\quad - z(\mathrm{d}F_x^{swp} + \mathrm{d}F_x^{pit} + \mathrm{d}F_x^{cpl} + \mathrm{d}F_x^{add,1} + \mathrm{d}F_x^{add,2})\boldsymbol{e}_y \\
&\quad + (y_{cp}^{swp}\mathrm{d}F_x^{swp} + y_{cp}^{pit}\mathrm{d}F_x^{pit} + y_{cp}^{cpl}\mathrm{d}F_x^{cpl} \\
&\quad + y_{cp}^{add,1}\mathrm{d}F_x^{add,1} + y_{cp}^{add,2}\mathrm{d}F_x^{add,2})\boldsymbol{e}_z\Big], \\
P_{aero}(t) &= \boldsymbol{\tau}\cdot\boldsymbol{\omega}.
\end{aligned} \tag{5.8}$$

In this equation, we take $\mathrm{d}F_y^{pit} = \mathrm{d}F_y^{cpl} = \mathrm{d}F_y^{add,1} = \mathrm{d}F_y^{add,2} = 0$ from the assumptions of infinitesimally thin wing and neglected viscous forces due to the absence of viscous theory. As shown below (§6), even with these assumptions, the prediction performance is not degraded.

The lift and drag forces on the flapping wing are

$$\begin{aligned}
L &= F_x\sin\eta + F_y\cos\eta, \\
D &= -\mathrm{sgn}\ (\dot{\phi})(F_x\cos\eta - F_y\sin\eta).
\end{aligned} \tag{5.9}$$

The components of the sectional aerodynamic force and the corresponding locations of centre of pressure are given as follows (Andersen *et al.* 2005; Whitney & Wood 2010; Wang *et al.* 2016):

$$\begin{gathered}
\mathrm{d}F_x^{swp} = -\frac{1}{2}\mathrm{sgn}(\boldsymbol{v}_{s,e}\cdot\boldsymbol{e}_x)\rho c|\boldsymbol{v}_{s,e}|^2(C_l\cos\alpha_e + C_d\sin\alpha_e)\mathrm{d}z, \\
\mathrm{d}F_y^{swp} = \frac{1}{2}\rho c|\boldsymbol{v}_{s,e}|^2(C_l\sin\alpha_e - C_d\cos\alpha_e)\mathrm{d}z, \\
y_{cp}^{swp} = d - \frac{c}{\pi}|\alpha_e|,
\end{gathered} \tag{5.10}$$

$$\mathrm{d}F_x^{pit} = \frac{1}{6}\rho\omega_z|\omega_z|C_{pit}[d^3 + (d-c)^3]\mathrm{d}z, \quad y_{cp}^{pit} = \frac{3}{4}\frac{d^4 + (d-c)^4}{d^3 + (d-c)^3}, \tag{5.11}$$

$$\mathrm{d}F_x^{cpl} = \begin{cases} -\pi\rho\left(\dfrac{3}{4}c - d\right)c(\boldsymbol{v}_{s,e}\cdot\boldsymbol{e}_y)\omega_z\mathrm{d}z & \text{for } \boldsymbol{v}_{s,e}\cdot\boldsymbol{e}_y \geqslant 0, \\ -\pi\rho\left(d - \dfrac{1}{4}c\right)c(\boldsymbol{v}_{s,e}\cdot\boldsymbol{e}_y)\omega_z\mathrm{d}z & \text{for } \boldsymbol{v}_{s,e}\cdot\boldsymbol{e}_y < 0, \end{cases} \tag{5.12}$$

$$y_{cp}^{cpl} = \begin{cases} d - \dfrac{1}{4}c & \text{for } \boldsymbol{v}_{s,e}\cdot\boldsymbol{e}_y \geqslant 0, \\ d - \dfrac{3}{4}c & \text{for } \boldsymbol{v}_{s,e}\cdot\boldsymbol{e}_y < 0, \end{cases}$$

$$\begin{aligned}
\mathrm{d}F_x^{add,1} &= -\frac{1}{4}\pi\rho c^2(\boldsymbol{a}_s\cdot\boldsymbol{e}_x)\mathrm{d}z, \quad y_{cp}^{add,1} = d - \frac{1}{2}c, \\
\mathrm{d}F_x^{add,2} &= -\frac{1}{4}\pi\rho c^2(\frac{1}{2}c - d)\psi_z\mathrm{d}z, \quad y_{cp}^{add,2} = d - \frac{(9c-16d)c}{16c-32d},
\end{aligned} \tag{5.13}$$

where C_l and C_d are the sectional lift and drag coefficients of a revolving wing, respectively, C_{pit} is the force coefficient due to the pitching motion, d is the position of the leading edge from the pitching axis, and ψ_z is the pitching acceleration (5.2). Note that (5.10)-(5.13) are the same as those of Wang *et al.* (2016) when $\boldsymbol{v}_{s,e} = \boldsymbol{v}_s$ and $\alpha_e = \alpha$ in (5.10) and (5.12). However, we use different formulae for C_l, C_d, and C_{pit} (see below) and do not include the Coriolis effect in $\mathrm{d}F_x^{cpl}$ because the translational velocity of a flapping wing is typically a few times the rotational velocity (Wang *et al.* 2016).

The conventional definitions of the lift (L) and drag (D) coefficients for a flat wing revolving at a constant angular velocity Ω are

$$C_L = \frac{2L}{\rho \hat{z}_2^2 (R+l)^2 \Omega^2 R \overline{c}}, \quad C_D = \frac{2D}{\rho \hat{z}_2^2 (R+l)^2 \Omega^2 R \overline{c}}, \tag{5.14}$$

where $\hat{z}_k (= \sqrt[k]{\int_{1-\lambda}^{1} \hat{c} \hat{z}^k \mathrm{d}\hat{z}/\lambda})$ is a non-dimensional radius of the kth moment of wing area, $\hat{c} = c/\overline{c}$, $\hat{z} = z/(R+l)$, and $\lambda = R/(R+l)$. Wang *et al.* (2004) suggested

$$\begin{aligned} C_L &= A \sin 2\alpha, \\ C_D &= B - C \cos 2\alpha, \end{aligned} \tag{5.15}$$

where A, B, and C are model constants determined from experimental or numerical data, and depend on the Reynolds number and wing geometry. Taha *et al.* (2014) provided a theoretical value for A in (5.15) based on the extended lifting line theory (Schlichting & Truckenbrodt 1979), and suggested

$$C_L = \pi \frac{AR}{\sqrt{AR^2 + 4} + 2} \sin 2\alpha. \tag{5.16}$$

They showed that (5.16) is an excellent predictive model for $0 \leqslant \alpha \leqslant \pi/2$. Note that this formula includes the effect of WTV as well as LEV (Wang *et al.* 2004; Berman & Wang 2007; Taha *et al.* 2014; Wang *et al.* 2016).

The sectional lift and drag coefficients of a revolving wing are defined by

$$C_l = \frac{2\mathrm{d}L}{\rho z^2 \Omega^2 c \mathrm{d}z}, \quad C_d = \frac{2\mathrm{d}D}{\rho z^2 \Omega^2 c \mathrm{d}z}, \tag{5.17}$$

where $\mathrm{d}L$ and $\mathrm{d}D$ are the sectional lift and drag forces acting on $c\mathrm{d}z$. When we assume $C_l = K\hat{z}^n$ (K is a proportional constant), $L = \int_l^{l+R} \frac{1}{2} K \rho z^2 \Omega^2 c \hat{z}^n \mathrm{d}z = \frac{1}{2} K \rho (l+R)^2 \Omega^2 R \overline{c} \int_{1-\lambda}^{1} \hat{c} \hat{z}^{n+2} \mathrm{d}\hat{z}/\lambda = \frac{1}{2} K \rho (l+R)^2 \Omega^2 R \overline{c} \hat{z}_{n+2}^{n+2}$, from which the proportional constant K is obtained as $K = \hat{z}_2^2 C_L / \hat{z}_{n+2}^{n+2}$.

Therefore, the sectional lift coefficient of a revolving wing can be estimated by non-dimensional radii of the second and $(n+2)$th moments of wing area and C_L if $C_l \sim \hat{z}^n$:

$$C_l = \frac{\hat{z}_2^2}{\hat{z}_{n+2}^{n+2}} \hat{z}^n C_L. \tag{5.18}$$

Wang *et al.* (2016) assumed that C_l is constant along the radial direction, i.e., $n = 0$. Then, $C_l = C_L$. Some other studies showed that $n \approx -1$ for a low-aspect-ratio revolving wing at low Reynolds number and high angles of attack (Poelma *et al.* 2006; Kim *et al.* 2015). We use $n = -1$ to estimate C_l, because $n = 0$ may be valid for a high-aspect-ratio revolving wing operating at high Reynolds number and low angles of attack.

Wang *et al.* (2016) provided a model for the drag coefficient from (5.16) assuming that the total force on the wing is normal to the wing surface:

$$C_D = C_L \tan\alpha = \frac{2\pi AR}{\sqrt{AR^2+4}+2} \sin^2\alpha. \tag{5.19}$$

They also assumed $C_d = C_D$, as done for the sectional lift coefficient. Recently, Oh & Choi (2018) suggested an improved model for the drag coefficient as follows (see appendix A):

$$C_D = \frac{1}{\lambda \hat{z}_2^2} \left(\frac{2.656}{Re^{1/2}} \kappa_1 + \frac{5.32}{Re^{7/8}} \kappa_2 \right) \cos 2\alpha + \frac{2\pi AR}{\sqrt{AR^2+4}+2} \sin^2\alpha, \tag{5.20}$$

where $Re = (l+R)\Omega\bar{c}/\nu$, $\kappa_1 = \int_{1-\lambda}^{1} \hat{c}^{1/2} \hat{z}^{3/2} \mathrm{d}\hat{z}$ and $\kappa_2 = \int_{1-\lambda}^{1} \hat{c}^{1/8} \hat{z}^{9/8} \mathrm{d}\hat{z}$. The first term in (5.20) is the contribution of viscous drag for a low-Reynolds-number revolving wing ($Re \sim O(10^2)$), and the second term is the same as (5.19). (5.16) and (5.20) provided excellent agreements with measured C_L and C_D of revolving fruit fly, hawkmoth and bumblebee wings for the ranges of $2.83 \leqslant AR \leqslant 3.74$ and $136 \leqslant Re \leqslant 8071$. In the present study, we assume that C_d is also in the form of $C_d = B^* - C^* \cos 2\alpha$

as in (5.15). To determine B^* and C^*, we consider the sectional drag coefficients at α=0 and $\pi/4$, as done in Oh & Choi (2018): $C_d(0) = 2.656/Re_c^{1/2} + 5.32/Re_c^{7/8}$ ($Re_c = z\Omega c/\nu$) from the triple deck theory (Stewartson 1968; Messiter 1970), and $C_d(\pi/4) = C_l(\pi/4)$ because the resultant force on the wing element at $\alpha = \pi/4$ (a post-stall angle) is nearly perpendicular to the wing chord. Then, our model for the sectional lift and drag coefficients of a revolving wing becomes

$$\begin{aligned} C_l &= \frac{\hat{z}_2^2}{\hat{z}_1}\frac{\pi AR}{\sqrt{AR^2+4}+2}\frac{\sin 2\alpha}{\hat{z}}, \\ C_d &= \left(\frac{2.656}{Re_c^{1/2}} + \frac{5.32}{Re_c^{7/8}}\right)\cos 2\alpha + \frac{\hat{z}_2^2}{\hat{z}_1}\frac{2\pi AR}{\sqrt{AR^2+4}+2}\frac{\sin^2\alpha}{\hat{z}}. \end{aligned} \tag{5.21}$$

In the present study, we use (5.21) for C_l and C_d in (5.10), together with $Re_c = |\boldsymbol{v}_{s,e}|c/\nu$ and α replaced by α_e.

C_{pit} has been commonly modelled as the drag coefficient of a wing at $\alpha = \pi/2$ (Andersen *et al.* 2005; Whitney & Wood 2010; Nakata *et al.* 2015; Wang *et al.* 2016). Note that Whitney & Wood (2010), Nakata *et al.* (2015) and Wang *et al.* (2016) took C_{pit} as the drag coefficient of a wing at $\alpha = \pi/2$ revolving about y_s-axis rather than about z-axis: e.g., $C_{pit} = 2\pi AR/(\sqrt{AR^2+4}+2)$ from (5.19) at $\alpha = \pi/2$ in Wang *et al.* (2016). According to Ellington (1991), the drag coefficient of a two-dimensional flat plate at $\alpha = \pi/2$ is empirically given as $C_d = 1.95+50/Re$. Therefore, we use

$$C_{pit} = 2.0 \tag{5.22}$$

as done in Andersen *et al.* (2005), although the flapping wing under consideration is not two-dimensional.

5.2. Estimation of induced downwash motion

To obtain the non-uniform downwash motion $\boldsymbol{w}$ defined in (5.5), we combine the present blade element theory with an inviscid momentum theory (Ellington 1984*c*; Johnson 1994). From the momentum theory, the ideal (without tip loss effect) period-averaged sectional lift ($\mathrm{d}\overline{L}$) of a flapping wing is

$$\mathrm{d}\overline{L} = 2\rho\Phi w^2 z \mathrm{d}z, \tag{5.23}$$

where Φ is the sweeping amplitude of the flapping wing and $w(z)$ is a local downwash velocity. $\mathrm{d}\overline{L}$ can be also obtained by the quasi-steady blade element theory: from (5.10)-(5.13) and the relationship in (5.9),

$$\begin{aligned}\mathrm{d}\overline{L} &= \frac{1}{T}\int_{t_0}^{t_0+T} \left(\mathrm{d}F_x \sin\eta + \mathrm{d}F_y \cos\eta\right) \mathrm{d}t \\ &= \frac{1}{T}\int_{t_0}^{t_0+T} \Big[\left(\mathrm{d}F_x^{swp} + \mathrm{d}F_x^{pit} + \mathrm{d}F_x^{cpl} + \mathrm{d}F_x^{add,1} + \mathrm{d}F_x^{add,2}\right)\sin\eta \\ &+ \mathrm{d}F_y^{swp}\cos\eta\Big] \mathrm{d}t.\end{aligned} \tag{5.24}$$

The downwash motion can be obtained by matching (5.23) with (5.24). However, w is nonlinearly coupled through $\mathrm{d}\boldsymbol{F}^{swp}$ and $\mathrm{d}\boldsymbol{F}^{cpl}$ as in (5.10) and (5.12). Thus, (5.23) and (5.24) should be solved by an iterative way or by a linearization of (5.24). We obtain w by both approaches and find that their differences are negligible (see below). The assumptions for the linearization are the following:

(i) The resultant force on the wing is nearly perpendicular to the wing surface because flapping wings typically operate at high angles of attack and thus the viscous friction force is much smaller than the force due to pressure difference. Then, the first term of C_d in (5.21) is neglected, which results in $\mathrm{d}F_y^{swp} = 0$ in (5.10).

(ii) $|\tan\eta|$ is of the order of 1 or less, and $\dot{\phi}\eta \leqslant 0$. These are valid for typical flapping flight of insects during most of the flapping period. For example, see figure 2.3(a). During advanced or delayed rotation, this assumption yields mispredictions of $\mathrm{d}\boldsymbol{F}^{swp}$ and $\mathrm{d}\boldsymbol{F}^{cpl}$, but does not cause a crucial error for estimation of $\mathrm{d}\overline{L}$ in (5.24) if the duration of such rotation is short as compared to the whole cycle.

(iii) Sectional sweeping speed is much faster than the speed of local downwash motion, i.e $|\boldsymbol{v}_s|(=|z\dot{\phi}|) \gg w$. Strictly, this is not valid near the wing root ($z \approx 0$) and during stroke reversal ($\dot{\phi} \approx 0$). In these cases, however, the sectional aerodynamic forces due to the sweeping velocity ($\mathrm{d}\boldsymbol{F}^{swp}$ and $\mathrm{d}\boldsymbol{F}^{cpl}$) are small. Therefore, albeit causing some discrepancies in sectional forces near the wing root, this assumption does not lead a significant error in estimating the aerodynamic forces acting on the entire wing. For a similar reason, this assumption has been commonly used to estimate downwash distribution of rotary wings (Johnson 1994; Usherwood & Ellington 2002*a*; Leishman 2006).

It should be emphasized that the above assumptions are used only for linearization of (5.24) and derivation of an explicit form of w.

The following relationships hold (figure 5.1(b)):

$$\left.\begin{aligned} \boldsymbol{w}\cdot\boldsymbol{e}_x &= -w\sin\eta, \quad \boldsymbol{w}\cdot\boldsymbol{e}_y = -w\cos\eta, \\ \boldsymbol{v}_s\cdot\boldsymbol{e}_x &= z\dot{\phi}\cos\eta, \quad \boldsymbol{v}_s\cdot\boldsymbol{e}_y = -z\dot{\phi}\sin\eta, \\ \sqrt{|\boldsymbol{v}_s|^2+w^2}\sin\alpha_e &= |\boldsymbol{v}_s|\sin\alpha - w\cos\alpha. \end{aligned}\right\} \tag{5.25}$$

With (5.10), (5.21) and assumption (i), $\mathrm{d}F_x^{swp}\sin\eta$ in (5.24) becomes

$$\begin{aligned}&\mathrm{d}F_x^{swp}\sin\eta\\&\approx -\mathrm{sgn}(\boldsymbol{v}_{s,e}\cdot\boldsymbol{e}_x)\pi\rho c(|\boldsymbol{v}_s|^2+w^2)\sin\alpha_e\sin\eta\frac{AR}{\sqrt{AR^2+4}+2}\frac{\hat{z}_2^2}{\hat{z}_1\hat{z}}\mathrm{d}z.\end{aligned}\tag{5.26}$$

Assumptions (ii) and (iii), and (5.25) provide the following approximations:

$$\left.\begin{aligned}&\mathrm{sgn}(\boldsymbol{v}_{s,e}\cdot\boldsymbol{e}_x)=\mathrm{sgn}(\boldsymbol{v}_s\cdot\boldsymbol{e}_x)\mathrm{sgn}\left(1-\frac{\boldsymbol{w}\cdot\boldsymbol{e}_x}{\boldsymbol{v}_s\cdot\boldsymbol{e}_x}\right)\approx\mathrm{sgn}(\boldsymbol{v}_s\cdot\boldsymbol{e}_x),\\&(|\boldsymbol{v}_s|^2+w^2)\sin\alpha_e\simeq|\boldsymbol{v}_s|^2\sin\alpha-w|\boldsymbol{v}_s|\cos\alpha.\end{aligned}\right\}\tag{5.27}$$

Then, (5.26) can be further simplified by

$$\begin{aligned}&\mathrm{d}F_x^{swp}\sin\eta\\&\approx-\mathrm{sgn}(\boldsymbol{v}_s\cdot\boldsymbol{e}_x)\pi\rho c(|\boldsymbol{v}_s|^2\sin\alpha-w|\boldsymbol{v}_s|\cos\alpha)\sin\eta\\&\times\frac{AR}{\sqrt{AR^2+4}+2}\frac{\hat{z}_2^2}{\hat{z}_1\hat{z}}\mathrm{d}z\\&\approx\mathrm{d}F_x^{swp}|_{w=0}\sin\eta\\&+w\underbrace{\left[\mathrm{sgn}(\boldsymbol{v}_s\cdot\boldsymbol{e}_x)\pi\rho c|\boldsymbol{v}_s|\cos\alpha\sin\eta\frac{AR}{\sqrt{AR^2+4}+2}\frac{\hat{z}_2^2}{\hat{z}_1\hat{z}}\right]}_{\equiv I}\mathrm{d}z.\end{aligned}\tag{5.28}$$

Here, it is noteworthy that I is always negative because $|\boldsymbol{v}_s|\cos\alpha=\boldsymbol{v}_s\cdot\boldsymbol{e}_y$ from (5.4), and thus $\mathrm{sgn}(\boldsymbol{v}_s\cdot\boldsymbol{e}_x)|\boldsymbol{v}_s|\cos\alpha=\mathrm{sgn}(z\dot{\phi}\cos\eta)(-z\dot{\phi}\sin\eta)=-|z\dot{\phi}|\sin\eta$ from (5.25). Therefore, the interactive effect of downwash and wing sweeping motions on the sectional lift ($wI\mathrm{d}z$) is always negative. Assumption (ii) and (5.25) yield

$$\mathrm{sgn}(\boldsymbol{v}_{s,e}\cdot\boldsymbol{e}_y)=\mathrm{sgn}(\boldsymbol{v}_s\cdot\boldsymbol{e}_y)\mathrm{sgn}\left(1-\frac{\boldsymbol{w}\cdot\boldsymbol{e}_y}{\boldsymbol{v}_s\cdot\boldsymbol{e}_y}\right)\approx\mathrm{sgn}(\boldsymbol{v}_s\cdot\boldsymbol{e}_y)=1.\tag{5.29}$$

With (5.12) and (5.29), $\mathrm{d}F_x^{cpl}\sin\eta$ in (5.24) reduces to

$$\begin{aligned}\mathrm{d}F_x^{cpl}\sin\eta &\approx -\pi\rho\left(\frac{3}{4}c-d\right)c(\boldsymbol{v}_s\cdot\boldsymbol{e}_y-\boldsymbol{w}\cdot\boldsymbol{e}_y)\omega_z\sin\eta\mathrm{d}z\\ &\approx \mathrm{d}F_x^{cpl}|_{w=0}\sin\eta-w\left[\pi\rho\left(\frac{3}{4}c-d\right)c\dot{\eta}\sin\eta\cos\eta\right]\mathrm{d}z.\end{aligned}\tag{5.30}$$

Substituting (5.28) and (5.30) into (5.24) provides an approximated period-averaged sectional lift from the blade element theory:

$$\begin{aligned}&\mathrm{d}\overline{L}\approx w\overline{I}\mathrm{d}z\\ &+\frac{1}{T}\int_{t_0}^{t_0+T}\sin\eta\left(\mathrm{d}F_x^{swp}|_{w=0}+\mathrm{d}F_x^{pit}+\mathrm{d}F_x^{cpl}|_{w=0}+\mathrm{d}F_x^{add,1}\right.\\ &\left.+\mathrm{d}F_x^{add,2}\right)\mathrm{d}t\\ &\approx w\overline{I}\mathrm{d}z+\mathrm{d}\overline{L}|_{w=0}.\end{aligned}\tag{5.31}$$

Note that the second term in (5.30) disappears after the integration due to the periodicity of wing kinematics, i.e $\overline{\dot{\eta}\sin\eta\cos\eta}$=0. Also, from the assumption (i), $\mathrm{d}F_y^{swp}|_{w=0}\approx 0$ and thus the integral in (5.31) becomes approximately the period-averaged sectional lift in the absence of downwash motion ($\mathrm{d}\overline{L}|_{w=0}$).

Equating (5.31) with (5.23) provides a quadratic equation for w:

$$2\rho\Phi z w^2=\overline{I}w+\frac{\mathrm{d}\overline{L}|_{w=0}}{\mathrm{d}z}.\tag{5.32}$$

The coefficients in (5.32) can be evaluated once wing geometry and kinematics are specified. Since $I<0$, $\overline{I}<0$. Thus, unless the last term is negative (it is in general positive for insect flight), w can be uniquely determined as

$$w=\frac{1}{4\rho\Phi z}\left[\overline{I}+\left(\overline{I}^2+8\rho\Phi z\frac{\mathrm{d}\overline{L}|_{w=0}}{\mathrm{d}z}\right)^{1/2}\right]\geqslant 0\quad\text{for } z\neq 0.\tag{5.33}$$

For the present wing geometry and kinematics, the maximum difference between (5.33) and iteratively obtained w is only 2.3%, and the time-averaged total lift, drag and power predicted with the latter are different from those with (5.33) by less than 1%.

Table 5.1 summarizes the differences among the present model, a predictive model by Wang *et al.* (2016) and a semi-empirical model by Nakata *et al.* (2015). The model of Nakata *et al.* (2015) contained model constants that were obtained by fitting them to predict their numerical results for a flapping hawkmoth wing during a quasi-periodic state. Thus, the effects of the fluid viscosity and wing-wake interaction were inherently included therein. However, their model constants depend on the wing geometry and should be determined whenever a wing geometry changes. Thus, their model is not entirely predictive. On the contrary, the predictive model suggested by Wang *et al.* (2016) did not contain any model constants, but did not include the effects of friction force and wing-wake interaction. In the present study, we include the effect of wing-wake interaction, and consider the variations of C_l and C_d along the wing span.

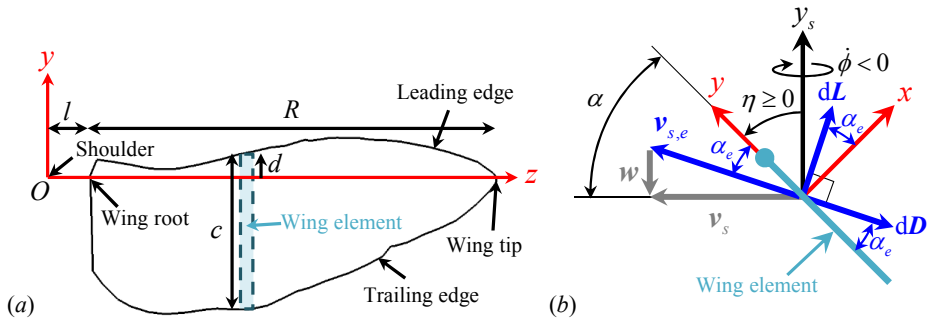

FIGURE 5.1. Wing parameters used for the blade element theory (hind wing): (a) wing shape; (b) angles and sectional forces. In (b), a wing cross section is shown in light blue with the leading edge denoted as a solid circle, and w is the downwash motion.

	Present	Wang *et al.* (2016)	Nakata *et al.* (2015)
Model constants	No	No	Yes
Effect of sweeping motion	Yes	Yes	Yes
Variations of C_l and C_d along wing span	Yes	No	No
Effect of pitching motion	Yes	Yes	Yes
Coupling effect	Yes	Yes	Yes
Added mass effect	Yes	Yes	Yes
Viscous effect	Yes	No	Yes
Effect of wing-wake interaction	Yes	No	Yes

TABLE 5.1. Comparison of the present quasi-steady model with the models by Wang *et al.* (2016) and Nakata *et al.* (2015).

Chapter 6

Model validation and discussions

In this chapter, we compare the forces and power ((5.8) and (5.9)) predicted by the present model ((5.10)-(5.13), (5.21) and (5.22)) together with w (5.33) for case 1 with those from the present numerical simulation and from the previous model by Wang *et al.* (2016). Figure 6.1 shows the temporal variations of the lift, drag and aerodynamic power coefficients predicted by the present model with $w = 0$ during the first stroke period ($0 \leqslant t/T < 1$), together with those from the present numerical simulation and predicted by the model of Wang *et al.* (2016). For the first half stroke ($0 \leqslant t/T < 0.5$), both models show excellent prediction performance, although they slightly overestimate the force and power peaks. On the contrary, the predictions are poor (especially for C_L) during the second half stroke ($0.5 \leqslant t/T < 1$) because of neglected induced downwash motion.

As shown in figure 6.2, the sweeping motion is the most dominant contributor to the force generation and power expenditure. The C_L due to the sweeping motion predicted by the present model is the same as

that by the model of Wang *et al.* (2016), although different C_l's in (5.21) and (5.16) are used for the present model and the model of Wang *et al.* (2016), respectively. The present C_D due to the sweeping motion is almost same as that of Wang *et al.* (2016), because the Reynolds number ($Re \approx 12000$) is high enough to neglect the viscous drag (the first term of C_d in (5.21)). On the other hand, predictions of the aerodynamic power due to the sweeping motion by two models are slightly different, because the sectional force coefficients due to the sweeping motion vary along the spanwise direction in the present model. The magnitudes of the forces and power due to the pitching motion are very small except during the stroke reversal. During the stroke reversal, the predictions are different because $C_{pit} = 2\pi AR/(\sqrt{AR^2+4}+2) \simeq 3.53$ for the hind wing ($AR = 3.30$) in Wang *et al.* (2016), but $C_{pit} = 2.0$ in the present model. The coupling effect is also an important component for the force generation and power requirement, and the model by Wang *et al.* (2016) predicts slightly larger peak values of the force and power from the coupling than the present model because they include the Coriolis effect. The added mass effect is quite large at the start and end of the half stroke and both models are identical.

Figure 6.3 shows the spanwise variations of the time-averaged sectional lift, drag and aerodynamic power coefficients predicted by the present model with $w = 0$ during the first half stroke, where $\overline{C}_l = 2\mathrm{d}\overline{L}/\rho(z\dot{\phi}_{rms})^2 c\mathrm{d}z$, $\overline{C}_d = 2\mathrm{d}\overline{D}/\rho(z\dot{\phi}_{rms})^2 c\mathrm{d}z$, $\overline{C}_{p_{aero}} = 2\mathrm{d}\overline{P}_{aero}/\rho(z\dot{\phi}_{crmc})^3 c\mathrm{d}z$, as used in figure 4.5. Here, $\mathrm{d}\overline{L}/\mathrm{d}z$, $\mathrm{d}\overline{D}/\mathrm{d}z$ and $\mathrm{d}\overline{P}_{aero}/\mathrm{d}z$ can be obtained by the present model together with (5.7) and (5.9). The results from the present numerical simulation and predicted by the model of Wang *et al.* (2016) are also plotted in this figure. The present model

quite accurately predicts the sectional force and power coefficients. Since the time-averaged sectional force coefficients due to the wing pitching motion and coupling effects are very small for both models and two models are the same for the added mass effect, the differences in the predicted time-averaged sectional force coefficients mainly come from the sweeping motion. Therefore, the present model for the sectional force coefficients due to the sweeping motion (5.21) seems to be more appropriate. High power coefficients near the wing root are predicted mainly by the sweeping motion in the present model, but they are predicted by the coupling effect and pitching motion in the model of Wang *et al.* (2016).

Figure 6.4 shows the temporal variations of the lift, drag and aerodynamic power coefficients predicted by the present model with $w(\neq 0)$ (5.33), together with those from the present numerical simulation ($4 \leqslant t/T < 5$) and predicted by the model of Wang *et al.* (2016). At this time period, the wake behind the hind wing reaches a quasi-periodic state. As shown in this figure, the present model including the effect of the induced downwash motion in the wake accurately predicts the force and power coefficients. The differences between the time-averaged lifts, drags and power consumptions predicted by the present model and from the numerical simulation are 0.5 %, 4.1 % and 10.8 %, respectively, and they may come from the assumptions of steady induced downwash motion ($w = w(z)$) and no swirl in the wake. The present result clearly indicates that the inclusion of the downwash motion in the wake ($w \neq 0$) is very important in developing an aerodynamic model.

Figure 6.5 shows the components of force and power coefficients predicted by the present model with $w(\neq 0)$ (5.33). As for the case of the first half stroke, the sweeping motion is most dominant in generating force

and power consumption that are positive during most of the flapping period. The effects of coupling and added mass are also quite large at the start and end of each half stroke. Due to the coupling effect (5.12), the lift, drag and power become negative at the start of half stroke (wing pitching down), but positive at the end of half stroke (wing pitching up). On the contrary, the lift, drag and power due to the added mass effect are positive and negative at the start and end of half stroke, respectively, because of the wing acceleration and deceleration. The pitching motion hardly produces the force and requires little power except during the stroke reversal. The lift and drag due to the pitching motion are positive before the stroke reversal but negative after that. However, the power due to the pitching motion is positive during the stroke reversal.

Figure 6.6 shows the spanwise variations of the time-averaged sectional lift, drag and power coefficients predicted by the present model with $w \neq 0$ and by the model of Wang *et al.* (2016), together with those from the present numerical simulation ($4 \leqslant t/T < 5$). The sectional lift, drag and power coefficients along the spanwise direction predicted by the present model with $w \neq 0$ are in good agreements with those from the present numerical simulation. Again, the wing sweeping motion is dominant in generating forces and power consumption away from the wing root ($\hat{z} > 0.2$), and the added mass and coupling effects are important near the wing root. However, the pitching motion requires non-negligible power near the wing root as much as the coupling term does. Note also that the aerodynamic power consumption due to the added mass is slightly negative. This is from relatively large negative aerodynamic power during the wing deceleration, and thus the hind wing can save a small amount of the aerodynamic power due to the added mass effect.

To investigate the applicability of the present model to other insect wings, we consider a fruit fly (*D. virilis*) wing that has the Reynolds number ($Re = 253$), aspect ratio ($AR = 2.4$), sweeping amplitude ($\Phi = 150^\circ$), non-dimensional radii of the first ($\hat{z}_1 = 0.54$) and second ($\hat{z}_2 = 0.58$) moments of wing area, and wing planform geometry and kinematics (see figures 6.7(a, b) and Sun & Tang (2002) for the detail), very different from those of the present rhinoceros beetle wing. Figure 6.7 shows the wing planform of a fruit fly (*D. virilis*) wing and the force and power coefficients predicted by the present model with (5.33), together with the results from the numerical simulation of Sun & Tang (2002). The predicted lift, drag and aerodynamic power coefficients are in excellent agreements with those from the numerical simulation by Sun & Tang (2002). Therefore, the present model may be applied to various wing shapes for their force and power prediction.

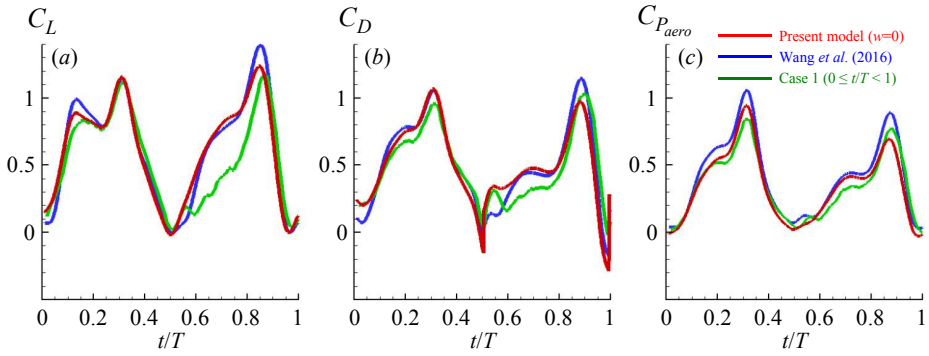

FIGURE 6.1. Predicted force and power coefficients using the present model with $w = 0$ and the model of Wang *et al.* (2016), and those from the present numerical simulation during the first stroke period (case 1): (a) lift; (b) drag; (c) aerodynamic power.

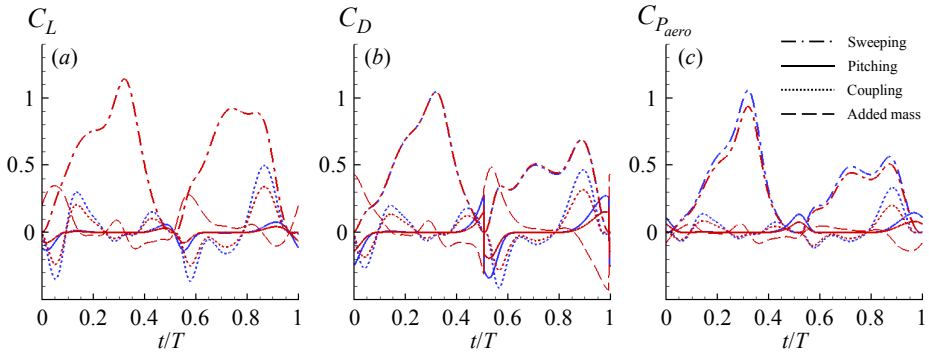

FIGURE 6.2. Predicted components of the force and power coefficients using the present model with $w = 0$ and the model of Wang *et al.* (2016): (a) lift; (b) drag; (c) aerodynamic power. Red and blue lines denote the results predicted by the present model ($w = 0$) and model of Wang *et al.* (2016), respectively.

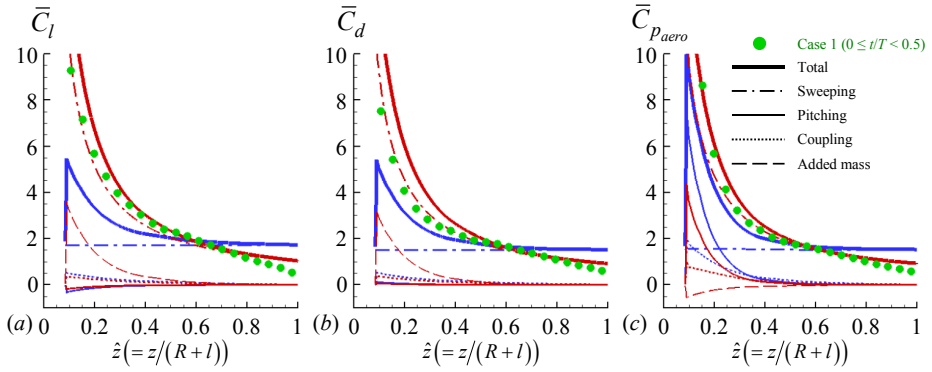

FIGURE 6.3. Predicted time-averaged sectional aerodynamic coefficients ($0 \leqslant t/T < 0.5$; case 1): (a) lift; (b) drag; (c) aerodynamic power. Red and blue lines denote the results predicted by the present model with $w = 0$ and model of Wang *et al.* (2016), respectively, and green solid circles are those from present numerical simulation.

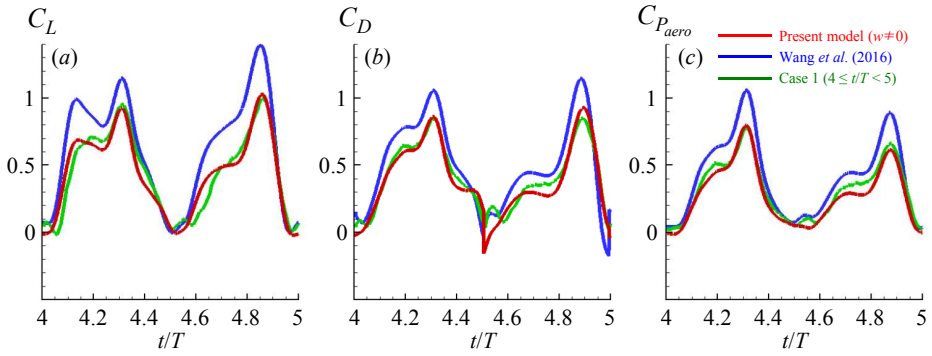

FIGURE 6.4. Predicted force and power coefficients using the present model with $w \neq 0$ and the model of Wang *et al.* (2016), and those from the present numerical simulation during the fifth stroke period (case 1): (a) lift; (b) drag; (c) aerodynamic power.

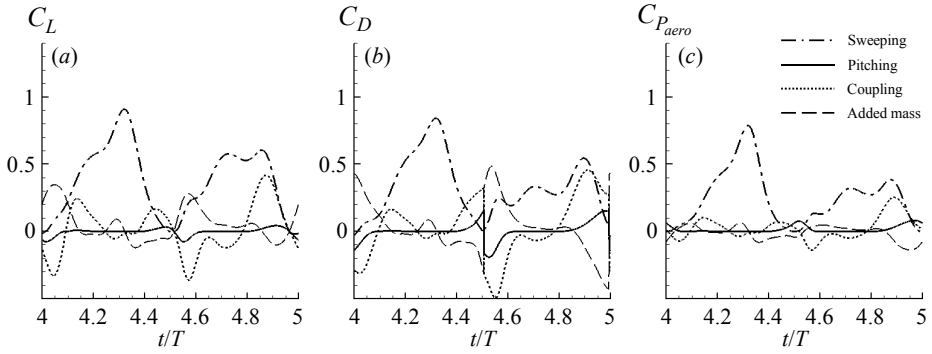

FIGURE 6.5. Predicted components of the force and power coefficients using the present model with $w \neq 0$: (a) lift; (b) drag; (c) aerodynamic power.

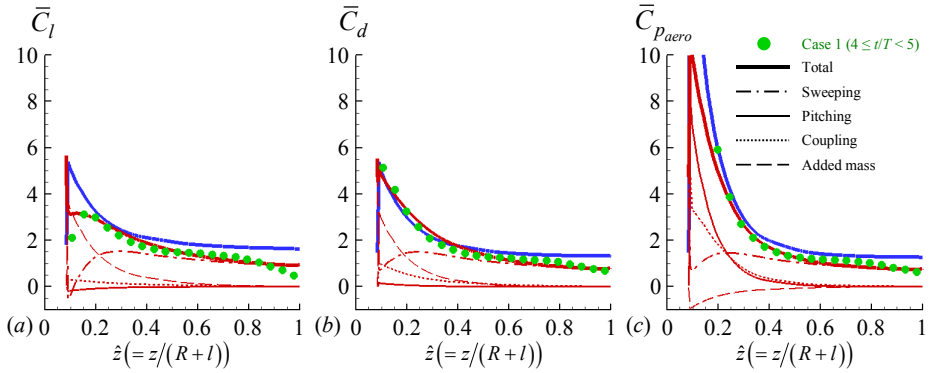

FIGURE 6.6. Predicted time-averaged sectional aerodynamic coefficients using the present model with $w \neq 0$ and the model of Wang *et al.* (2016), and those from the present numerical simulation ($4 \leqslant t/T \leqslant 5$; case 1): (a) lift; (b) drag; (c) power. Red and blue lines denote the results predicted by the present model ($w \neq 0$) and model of Wang *et al.* (2016), respectively, and green solid circles are those from present numerical simulation.

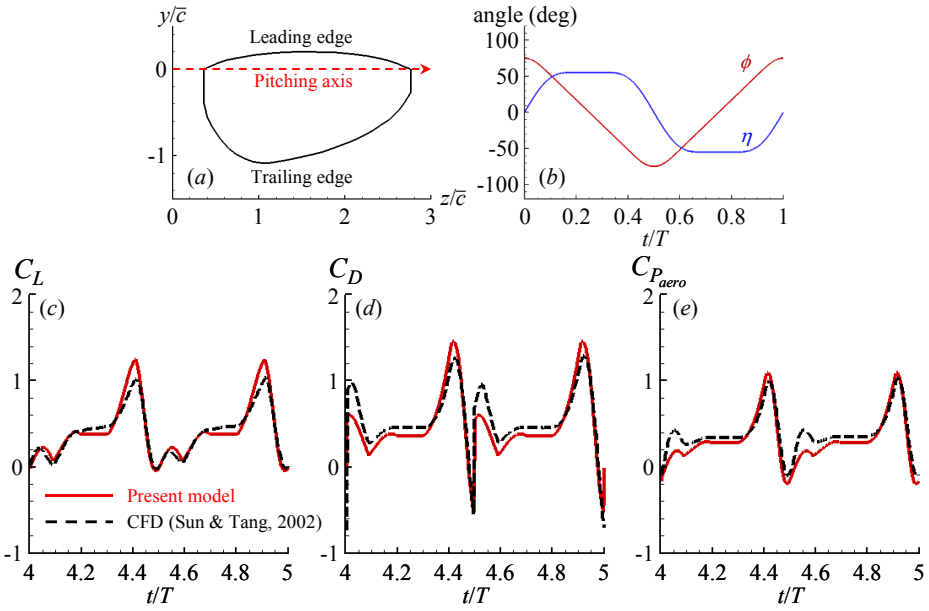

FIGURE 6.7. Fruit fly (*D. virilis*) wing and its force and power coefficients: (a) wing planform geometry; (b) wing kinematics; (c) lift coefficient; (d) drag coefficient; (e) aerodynamic power coefficient. The results from numerical simulation are from Sun & Tang (2002).

Chapter 7

Further consideration on the induced downwash motion

So far, we modeled the induced downwash velocity as steady and non-uniform in the spanwise direction, i.e., $w(z)$. However, the flow fields behind the wing indicate that the induced downwash motion should be unsteady. Therefore, we consider an unsteady non-uniform downwash motion $w(t, z)$ in this section. Figure 7.1 shows the comparison of the downwash velocities from the present model and numerical simulation for case 1. The area A_w for the spatial average of the downwash velocity shown in figure 7.1(a) is similar to those used for computing the effective angle of attack in the previous studies (Birch & Dickinson 2003; Kim *et al.* 2015; Han *et al.* 2019). As shown in figure 7.1(b), the downwash velocity $\overline{w}^{A_w}(t, \hat{z})$ ($w(t, \hat{z})$ averaged over A_w; $\hat{z} = z/(R + l)$) almost linearly decreases in time except very near the wing tip ($\hat{z} \leqslant 0.8$): i.e., it is maximum at the beginning of each half stroke and minimum at the end of half stroke, because vortical structures generated in the previous stroke are convected downward. Upward velocity is also observed very near the

wing tip due to the tip vortex and just before the stroke reversal because of the leading edge vortex. Figure 7.1(c) shows the spanwise distribution of the downwash velocity averaged over A_w and t from numerical simulation and the present model w (5.33). Except near the wing tip, the predicted downwash velocity w is in a good agreement with that from numerical simulation. The discrepancy near the tip comes from the upward induced velocity existing in this region. The effective angles of attack predicted by the present model are compared at two different spanwise locations (near the mid-span and tip, respectively) with those obtained from numerical simulation in figures 7.1(d) and (e), together with the prescribed angle of attack α. Near the mid-span ($\hat{z} = 0.425$), $w < \overline{w}^{A_w}$ at early stage of half stroke and $w > \overline{w}^{A_w}$ at late stage because $w \approx \overline{w}^{A_w,t}$ (see figures 7.1(b) and (c)), and thus α_e from the present model is larger and smaller than those from numerical simulation at early and late stages, respectively (figure 7.1(d)). On the other hand, near the wing tip ($\hat{z} = 0.925$), the wing velocity is much larger than the induced velocity, so that the effective angles of attack from the present model and numerical simulation are not very different from the prescribed angle of attack (figure 7.1(e)).

As shown in figure 7.1(b), the temporal variation of the downwash velocity may be approximated with a sawtooth profile in time, i.e, $w(t, z)(\geqslant 0)$, which can be formulated as

$$w(t, z) = (1 + k)\overline{w}(z) + k\overline{w}(z)f(t), \tag{7.1}$$

where

$$f(t) = \begin{cases} -\dfrac{2}{T_u}(t - t_u) & \text{for } t_u \leqslant t \leqslant\ t_u + T_u, \\ -\dfrac{2}{T - T_u}(t - t_u - T_u) & \text{for } t_u + T_u \leqslant t \leqslant t_u + T_u + T_d, \end{cases} \tag{7.2}$$

$\overline{w}(z)$ is the downwash velocity averaged over a flapping period, $0 \leqslant k \leqslant 1$, t_u is the time corresponding to the upstroke start, T_u and T_d are the upstroke and downstroke periods (they not necessarily half of one flapping period $(T_u + T_d)$), respectively. At $k = 0$, w is a steady downwash motion, but w becomes a steeper sawtooth wave at a higher k (see figure 7.2(a)).

From the momentum theory under the consideration of a periodic downwash motion (Siekmann 1963; Ellington 1984*c*), the period-averaged sectional lift of a flapping wing becomes

$$\mathrm{d}\overline{L} = 2\rho\Phi\overline{w^2}z\mathrm{d}z. \tag{7.3}$$

For the sawtooth profile of w in time (7.1), $\overline{w^2} = \overline{w}^2(1 + k^2/3)$. Therefore, (7.3) becomes

$$\mathrm{d}\overline{L} = 2\rho\Phi\overline{w}^2\left(1 + \frac{k^2}{3}\right)z\mathrm{d}z. \tag{7.4}$$

Substituting (7.1) into (5.28) yields

$$\mathrm{d}F_x^{swp}\sin\eta \approx \mathrm{d}F_x^{swp}|_{w=0}\sin\eta + (1+k)\overline{w}I\mathrm{d}z + k\overline{w}f(t)I\mathrm{d}z. \tag{7.5}$$

With (7.1), (5.30) becomes

$$\mathrm{d}F_x^{cpl}\sin\eta \approx \mathrm{d}F_x^{cpl}|_{w=0}\sin\eta + (1+k)\overline{w}I'\mathrm{d}z + k\overline{w}f(t)I'\mathrm{d}z, \tag{7.6}$$

where $I' = -\pi\rho\left(\frac{3}{4}c - d\right)c\dot{\eta}\sin\eta\cos\eta$. Substituting (7.5) and (7.6) to (5.24) with $\overline{I'} = 0$ gives

$$\mathrm{d}\overline{L} \approx \overline{w}\left[(1+k)\overline{I} + k\overline{fI} + k\overline{fI'}\right]\mathrm{d}z + \mathrm{d}\overline{L}|_{w=0}. \tag{7.7}$$

Equating (7.4) with (7.7) provides a quadratic equation for $\overline{w}$:

$$2\rho\Phi\overline{w}^2\left(1 + \frac{k^2}{3}\right)z = \overline{w}\underbrace{\left[(1+k)\overline{I} + k\overline{fI} + k\overline{fI'}\right]}_{\equiv\,\overline{I}^*} + \frac{\mathrm{d}\overline{L}|_{w=0}}{\mathrm{d}z}. \tag{7.8}$$

If $\overline{I}^*$ is negative and the last term in (7.8) is positive, $\overline{w}$ is obtained by

$$\overline{w} = \frac{1}{4\rho\Phi z(1+k^2/3)} \times \left\{ \overline{I}^* + \left[\overline{I}^{*2} + 8\rho\Phi z \left(1+\frac{k^2}{3}\right) \frac{\mathrm{d}\overline{L}|_{w=0}}{\mathrm{d}z} \right]^{1/2} \right\} \geqslant 0 \quad \text{for } z \neq 0. \tag{7.9}$$

Here, $\overline{I}^* = \overline{I}$ when $k = 0$, and thus (7.9) is reduced to (5.33).

To examine the effect of the unsteadiness of the downwash motion in the present model, we obtain the aerodynamic force and power coefficients predicted by the present model ((5.10)-(5.13), (5.21) and (5.22)) together with (7.1), (7.2) and (7.9) for $k = 0$ and 1, respectively, and compared the results with those from the present numerical simulation (case 1) and also from the present model with $w = 0$ in figures 7.2(b-d). As shown, the predicted results from the present model with non-zero w (with $k = 0$ and 1) agree very well with those of the numerical simulation, indicating that the unsteadiness of w in the model is not very important in predicting the aerodynamic performance at least for the present wing kinematics and geometry considered. Note also that the model with $w = 0$ (i.e., no induced downwash motion) does not accurately predict the aerodynamic forces.

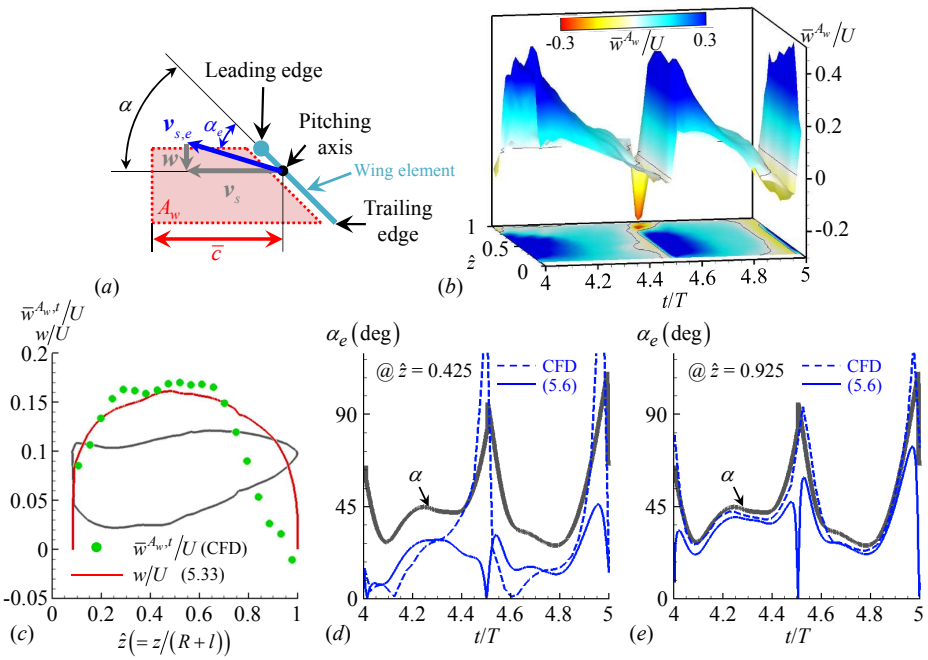

FIGURE 7.1. Downwash velocity and effective angle of attack (case 1): (a) schematic diagram of the area (A_w) for the spatial average of the downwash velocity; (b) temporal and spanwise distribution of the downwash velocity averaged over A_w, $\overline{w}^{A_w}(t, \hat{z})$, from numerical simulation; (c) spanwise distribution of the downwash velocity averaged over A_w and t, $\overline{w}^{A_w,t}(\hat{z})$, from numerical simulation (CFD) and the present model w (5.33); (d) and (e) effective angles of attack at $\hat{z} = 0.425$ and 0.925, respectively, from numerical simulation and present model.

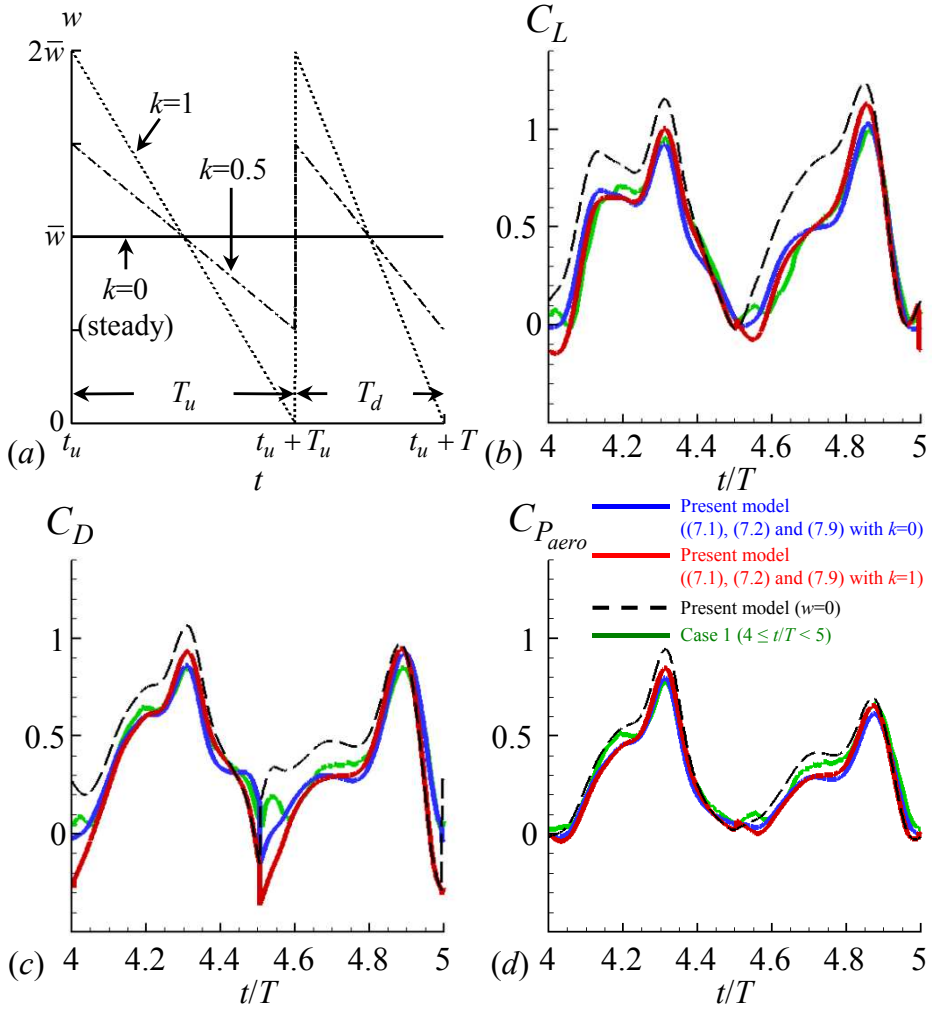

FIGURE 7.2. A model of the induced downwash velocity and its predictions of the force and power coefficients for different k's (case 1): (a) $w(t,z)$ (7.1) for $k = 0$, 0.5 and 1; (b) lift; (c) drag; (d) aerodynamic power. In (b) - (d), the values of $t_u/T = 3.995$, $T_u/T = 0.511$ and $T_d/T = 0.489$ ($k = 0$ and 1) are used for (7.1) and (7.2). The results from the present numerical simulation and also from the present model with $w = 0$ are compared in these figures.

Chapter 8

Conclusions

In the present study, the aerodynamic force generated and power required by hovering motion of a rhinoceros beetle (*Trypoxylus dichotomus*) were investigated using numerical simulations, and a quasi-steady blade element theory combined with a momentum theory was suggested to predict the force and power on the wing. The wing kinematics of a hovering beetle were measured using three high-speed cameras, and the geometries of body and elytron were three-dimensionally scanned for the use of numerical simulation. We showed from numerical simulation that the twist of hind wing along the wing span direction has a positive but marginal effect on the total force and power on the wing, and the aerodynamic role of the elytron is negligible in producing the lift and drag forces. Thus, the hind wing alone can generate the vertical force enough to support the weight. The elytron may play a role when it moves forward or turns during flight (see, for exmaple, Le *et al.* (2013)). However, its detailed mechanism may be further investigated to fully understand its aerodynamic function.

We developed a predictive quasi-steady blade element theory for the

force produced and power required by hovering motion, in which the effects of the wing-wake interaction as well as the wing sweeping, pitching, their coupling and added mass were included. For the wing-wake interaction, the wake generated by a flapping wing was modelled as a steady or unsteady non-uniform induced downwash motion, and this downwash motion was derived by combining the blade element theory with the inviscid momentum theory. Both models with steady and unsteady induced downwash motions provided excellent agreements with the numerical results, indicating that the steady downwash motion alone should be enough to provide accurate force generation and power consumption. With the aerodynamic model developed, we showed that the wing sweeping motion mainly contributes to aerodynamic force generation and power consumption. The added mass and coupling of sweeping and pitching motions were also important contributors to the force production and power consumption. The pitching motion hardly generated the aerodynamic forces but required the aerodynamic power near the wing root. The present aerodynamic model with the steady non-uniform induced downwash motion is a predictive model since it does not include any model constants, and thus may be used for various wing geometries. Therefore, the present model may be used for the optimizations of the flapping-wing geometry and kinematics to enhance the performance of the flapping wing in hover. Finally, we would like to mention the limitations of the present model. First, as mentioned by Wang *et al.* (2016), the present model assumed a quasi-steady state at each instant of the wing motion and thus neglected the Wagner effect (Wagner 1925). However, as indicated by Wang *et al.* (2016), the Wagner effect may be small at high angles of attack and low Reynolds numbers. Second, the present model was based on the model

equations for the drag and lift coefficients ((5.16) and (5.20)) that were tested for the ranges of $2.83 \leqslant AR \leqslant 3.74$ and $136 \leqslant Re \leqslant 8071$ (see Oh & Choi (2018)). Thus, the present model may provide poor predictions for a much wider range of these parameters. However, since many insect wings operate at these parameter ranges (Lentink & Dickinson 2009), the present model may be predictive for most hovering insect wings. Third, we developed our model for a wing without camber. Therefore, a further study is required to develop a model for a flapping wing with camber in the future.

Part II.

Optimal wing geometry and kinematics of a hovering rhinoceros beetle for minimum power consumption

Chapter 1

Introduction

The idea of bio-inspired design has initially proposed from the belief that biological organisms have evolved to better adapt to their environment through the natural selection. From this point of view, the flapping flight of insects has received a great attention in designing bio-inspired flapping-wing micro air vehicles (FWMAVs), with a high flight performance (Shyy *et al.* 2008, 2013). However, since biological organisms are typically multi-functional (Berman & Wang 2007; Zheng *et al.* 2013), it is questionable that flapping wings of various insects are optimal for a specific flight performance which may vary upon design purpose. Therefore, optimization of wing motion and shape of flying insects for various objective functions may be important to understand the variety of their wing motions and shapes and to improve the flight performance of FWMAVs. For these reasons, there has been several attempts to optimize wing motion or shape of flying insects for a specific flight performance (e.g. lift-to-drag ratio, energy consumption, power loading) based on experiment (Park & Choi 2012), computational fluid dynamics (CFD) (Zheng *et al.* 2013)

and an aerodynamic model (Berman & Wang 2007; Ansari *et al.* 2008*a*,*b*; Nabawy & Crowther 2014; Nakata *et al.* 2015; Ke *et al.* 2017; Wang *et al.* 2017).

Berman & Wang (2007) optimized the wing motions of hovering fruit fly, bumblebee and hawkmoth for minimium mechanical power consumption, assuming that an insect wing is a rigid plate with a half-ellipse wing planform shape. Fixing the stroke amplitudes to the empirically measured values, they found that the optimal wing-beat frequencies match well with the observed ones. Zheng *et al.* (2013) also considered a rigid and flat hawkmoth wing and found the optimal wing motion maximizing aerodynamic power loading (the ratio of mean lift to the mean aerodynamic power expenditure). Unlike the measured wing motion (inclined stroke plane), the optimal wing motion of the hawkmoth resembles the normal hovering flight and has a 33% higher power loading than that from the measured wing motion. Therefore, they showed that the measured wing motion of the hawkmoth is not optimal in terms of aerodynamic power loading.

For wing shape optimization, Ansari *et al.* (2008*b*) suggested that a wing planform shape with a straight leading edge and more wing area outboard generally produces better lift and lift-to-torque characteristics. Also, they proposed that the best position of the pitching axis for lift is the mid-chord point. Nabawy & Crowther (2014) suggested a wing planform shape of which radius of the first moment of area is 40% wing length for minimum induced power factor, assuming that non-dimensional chord length along the wing span follows the beta distribution. Wang *et al.* (2017) showed that the optimal pitching axis for minimum power consumption is located between the leading edge and the mid-chord point,

which results in a wing shape similar to the hawkmoth wing. Also, their results indicated that the wing with the optimal pitching axis can save up to 33% of power as compared to a wing having the pitching axis as a straight leading edge.

In the present study, we focus on a hovering rhinoceros beetle because it is one of the heaviest insects and has the highest wing loading among the biological flyers that satisfy the weight and size requirements of FW-MAVs (Oh *et al.* 2020) (see also figure 1.1 in part I). To have a high wing loading, it in general requires a high weight-specific power. Also, it typically takes more power to hover than almost any other flight modes because of no ambient wind to help lift force generation (Berman & Wang 2007). Thus, it is reasonable to expect that the flapping wing motion and shape of a hovering rhinoceros beetle may be close to the optimal ones minimizing power consumption. So far, previous studies for a hovering rhinoceros beetle have mainly focused on the optimization of the wing twist along the wing span (Truong *et al.* 2013*a*; Phan *et al.* 2017), but the optimal wing shape of the beetle was not fully investigated. Therefore, the objective of our study is to investigate the optimal wing shape as well as flapping wing motion of a hovering rhinoceros beetle for minimum power consumption. To that end, we first parametrize the flapping wing motion and shape. Then, we use a predictive quasi-aerodynamic model combined with a momentum theory to more accurately predict the aerodynamic performance of a flapping wing in hover (Oh *et al.* 2020). Based on the aerodynamic model, we separately optimize wing motion and shape for minimum power consumption. The present results will provide a useful strategy to design the optimal flapping wing motion and shape of a beetle-like FWMAV.

Chapter 2

Models for a hovering flight of a rhinoceros beetle

Rhinoceros beetles have two pairs of hard fore wings (elytra) and flexible hind wings. For the simplicity, we consider the hind wings only and assume that hind wing is a rigid and flat plate from the previous results in part I (Oh *et al.* 2020):

(i) Aerodynamic effects of the elytra and body on the force generation and aerodynamic power consumption are negligible because of their low velocity and short length scales as compared to those of hind wings.

(ii) When the pitching angle of a rigid and flat hind wing is taken to be that at 60% wing length, the enhancement of the total vertical force and the reduction of the total aerodynamic power expenditure due to the twist of hind wings along the wing span are less than 3%, respectively, as compared to its flat counterpart.

2.1. Wing motion and shape

Figure 2.1(a) shows the definitions of the coordinates and wing kinematic parameters. To describe the flapping wing motion, we introduce three coordinates (see also §2.2 in part I). The (X, Y, Z) coordinate is an inertial reference frame where the XZ plane is the horizontal plane, X and Z are the frontal and right lateral directions, respectively, and Y-axis points in the anti-gravity direction. The stroke plane is an imaginary plane where the wing roughly moves, which inclined at an angle β with respect to the horizontal plane. We define the (x_s, y_s, z_s) coordinate such that y_s is perpendicular to the stroke plane, $z_s = Z$, and x_s is in compliance with the right hand rule and fix its origin at the wing root. Finally, the (x, y, z) coordinate is a non-inertial reference frame co-rotating with the wing and is defined such that x, y and z indicate wing thicknesswise, chordwise, and spanwise directions, respectively.

Within the stroke plane, the flapping motion of insects can be typically decomposed into the translational and pitching motions, where the translational motion can be further decomposed into the sweeping and (out-of-plane) deviation motions, respectively. We consider the sweeping and pitching motions only because the out-of-plane deviation motion is in general insignificant (Ellington 1984*b*) (see also figure 2.3(a) in part I). Here, the sweeping (ϕ) and pitching (η) angles are defined as the angles of rotation about y_s axis (azimuth) and the spanwise axis (z-axis) of the wing, respectively. Therefore, wing angular velocity ($\boldsymbol{\omega}$) and acceleration ($\boldsymbol{\psi}$) are

$$\begin{aligned} \boldsymbol{\omega} &= \dot{\phi}\boldsymbol{e}_{y_s} + \dot{\eta}\boldsymbol{e}_z = \dot{\phi}\sin\eta\boldsymbol{e}_x + \dot{\phi}\cos\eta\boldsymbol{e}_y + \dot{\eta}\boldsymbol{e}_z, \\ \boldsymbol{\psi} &= \dot{\boldsymbol{\omega}} = (\ddot{\phi}\sin\eta + \dot{\phi}\dot{\eta}\cos\eta)\boldsymbol{e}_x + (\ddot{\phi}\cos\eta - \dot{\phi}\dot{\eta}\sin\eta)\boldsymbol{e}_y + \ddot{\eta}\boldsymbol{e}_z, \end{aligned} \tag{2.1}$$

where $\boldsymbol{e}_i$ means the unit vector in i direction. For the purpose of optimization, we adopt a kinematic model proposed by Berman & Wang (2007) to parametrize the sweeping and pitching angles:

$$\begin{aligned}\phi(t) &= \phi_0 + \frac{\phi_m}{\sin^{-1} K}\sin^{-1}[K\cos(2\pi f t)],\\ \eta(t) &= \eta_0 + \frac{\eta_m}{\tanh C_\eta}\tanh[C_\eta\cos(2\pi f t + \Phi_\eta)].\end{aligned} \tag{2.2}$$

Here, $f(=1/T)$ is the flapping frequency and Φ_η is the phase shift of the pitching motion with respect to the sweeping motion. The subscripts 0 and m denote offsets and amplitudes, respectively, and K and C_η are the shape factors for each of motions (Berman & Wang 2007) (see figures 2.2(a, b)). Also, the stroke plane angle (β) is introduced to uniquely determine the wing motion with respect to the (X, Y, Z) coordinate. Therefore, nine kinematic parameters are considered to specify the flapping wing motion:

$$\Xi_k = (f, \phi_m, \phi_0, K, \eta_m, \eta_0, C_\eta, \Phi_\eta, \beta). \tag{2.3}$$

For the wing geometry, we consider the wing planform shape only, i.e. the wing thickness is zero ($x = 0$). Figure 2.1(b) shows the definitions of parameters for the wing planform shape: R is the wing length; d is the location of leading edge with respect to the pitching axis; c and $\bar{c}$ are the local and mean chord lengths, respectively. Note that we do not consider an offset of the wing root in the spanwise direction. Ellington (1984a) suggested that non-dimensional chord length ($\hat{c} = c/\bar{c}$) of a typical insect wing along its wing span follows the beta distribution, and it can be

determined by $\hat{z}_1$ only:

$$\begin{aligned}
\hat{c}(\hat{z}; p_\beta, q_\beta) &= \frac{\hat{z}^{p_\beta - 1}(1 - \hat{z}^{q_\beta - 1})}{\displaystyle\int_0^1 \hat{z}^{p_\beta - 1}(1 - \hat{z}^{q_\beta - 1})\mathrm{d}\hat{z}}, \\
p_\beta &= \hat{z}_1 \frac{\hat{z}_1^2 - \hat{z}_2^2}{\hat{z}_2^2 - \hat{z}_1^2}, \quad q_\beta = (1 - \hat{z}_1)\frac{\hat{z}_1^2 - \hat{z}_2^2}{\hat{z}_2^2 - \hat{z}_1^2}, \\
\hat{z}_2 &= 0.929\hat{z}_1^{0.732},
\end{aligned} \tag{2.4}$$

where p_β and q_β are shape parameters of the beta distribution, $\hat{z}_k (= \sqrt[k]{\int_0^1 \hat{c}\hat{z}^k \mathrm{d}\hat{z}})$ is the non-dimensional radius of the kth moment of wing area, and $\hat{z} = z/R$. To determine the leading-edge profile and thus fully specify wing planform shape, we adopt a model for the non-dimensional position of leading edge ($\hat{d} = d/c$) suggested by Wang *et al.* (2017):

$$\hat{d} = \hat{z}(\hat{d}_t - \hat{d}_r) + \hat{d}_r, \tag{2.5}$$

where $\hat{d}_r$ and $\hat{d}_t$ are $\hat{d}$ at the wing root and tip, respectively, and the dependence of the wing planform shape on $\hat{z}_1$, $\hat{d}_r$ and $\hat{d}_t$ is shown in figure 2.2(c). Note that $\hat{d}$ has a value between $\hat{d}_r$ and $\hat{d}_t$ since we assume that $\hat{d}$ changes linearly along the wing span and can be also interpreted as a measure of how far the pitching axis is from the leading edge. Therefore, we consider five parameters to determine $c(z)$ and $d(z)$:

$$\Xi_g = (R, AR, \hat{z}_1, \hat{d}_r, \hat{d}_t), \tag{2.6}$$

where $AR (= R/\bar{c})$ is the single wing aspect ratio. Here, R and AR can be interpreted as scaling factors for the wing planform shape (Ellington 1984*a*). The Reynolds number ($Re = U\bar{c}/\nu$) is about 12000 based on the mean wing tip velocity ($U = 2\Phi f R$) and chord length ($\bar{c}$), where ν is the kinematic viscosity of air and $\Phi (= 2\phi_m)$ is the total sweeping amplitude, respectively.

2.2. Aerodynamic force and power expenditure

Aerodynamic force ($\boldsymbol{F}$) and torque ($\boldsymbol{\tau}_{aero}$) on the wing are obtained by integrating the sectional aerodynamic force ($\mathrm{d}\boldsymbol{F}$) and torque ($\mathrm{d}\boldsymbol{\tau}_{aero}$) along the wing span:

$$\boldsymbol{F} = \int_0^R \mathrm{d}\boldsymbol{F}, \qquad \boldsymbol{\tau}_{aero} = \int_0^R \mathrm{d}\boldsymbol{\tau}_{aero}. \tag{2.7}$$

Here, $\mathrm{d}\boldsymbol{F}$ and $\mathrm{d}\boldsymbol{\tau}_{aero}$ in (2.7) are modelled as the superposition of contributions due to wing sweeping (*swp*) and pitching (*pit*) motions, their coupling (*cpl*), and added mass effects (*add*). Formulae for each of terms are given in §5 in part I (see also Oh *et al.* (2020) for the detail). Then, the vertical force (F_Y) generation can be obtained from the following coordinate transform:

$$F_Y = (F_x \sin\eta + F_y \cos\eta)\cos\beta - (F_x \cos\eta - F_y \sin\eta)\sin\beta\cos\phi. \tag{2.8}$$

We estimate torque due to wing inertia ($\boldsymbol{\tau}_{iner}$) by using the Euler equation for a rigid body with a rotational motion. According to the Euler equation, the required torque to move a rigid and flat wing in a vacuum is

$$\boldsymbol{\tau}_{iner} = \boldsymbol{I_w}\dot{\boldsymbol{\omega}} + \boldsymbol{\omega} \times (\boldsymbol{I_w}\boldsymbol{\omega}), \tag{2.9}$$

where $\boldsymbol{I_w}$ is the inertia tensor of the wing. Due to the insufficient information on the exact mass distribution ($\mathrm{d}m$) of the wing, however, we assume that the wing has a uniform density. With the assumption of an

infinitesimally thin wing ($x = 0$), $\boldsymbol{I_w}$ can be approximated by

$$\begin{aligned}\boldsymbol{I_w} &= I_{w,ij} = \int_V (r_k r_k \delta_{ij} - r_i r_j)\mathrm{d}m \\ &\approx \frac{m_w}{S}\begin{bmatrix} \int_S (y^2+z^2)\mathrm{d}S & 0 & 0 \\ 0 & \int_S z^2\mathrm{d}S & -\int_S yz\mathrm{d}S \\ 0 & -\int_S yz\mathrm{d}S & \int_S y^2\mathrm{d}S \end{bmatrix},\end{aligned} \tag{2.10}$$

where r_k is the position in k direction, δ_{ij} is the Kronecker delta, m_w and $S(= R\overline{c})$ are wing mass and planform area, respectively. Here, m_w is taken to be 60 mg (Oh *et al.* 2020) (see also table 2.1 in part I).

Mechanical power (P_{mech}), the required power to drive a wing in the presence of fluid, may be represented by the summation of aerodynamic power (P_{aero}) and inertial power (P_{iner}). Here, P_{aero} and P_{iner} are evaluated by the inner products of corresponding torque and wing angular velocity, and thus mechanical power is obtained by

$$P_{mech} = P_{aero} + P_{iner} = \boldsymbol{\tau}_{aero}^T \boldsymbol{\omega} + (\boldsymbol{I_w}\boldsymbol{\psi})^T \boldsymbol{\omega}. \tag{2.11}$$

Wing deceleration causes the reduction in the wing kinetic energy, which results in a negative inertial power. As long as the law of energy conservation holds, this amount of kinetic energy reduction must be transferred to the surroundings. If there is an energy storage system such as a torsional spring (Whitney & Wood 2010) and it can perfectly transform the kinetic energy into an elastic energy, this elastic energy can be used to accelerate the wing during the next half stroke (Ellington 1984*d*). In this case, the period-averaged inertial power is exactly zero and thus the period-averaged mechanical power reduces to the period-averaged aerodynamic power:

$$\overline{P}_{mech} = \overline{P}_{aero}. \tag{2.12}$$

In the absence of such an energy storage system, on the contrary, the amount of kinetic energy reduction (negative inertial power) can be dissipated as heat and sound energy or used to compensate aerodynamic power consumption. If the reduced kinetic energy is used for aerodynamic power consumption and then the excess energy is transformed to heat and sound energy, the total power required by the wing can be modelled as (Ke *et al.* 2017; Wang *et al.* 2017):

$$\overline{P}^{+}_{mech} = \overline{R(P_{mech})} = \frac{1}{T}\int_{t_0}^{t_0+T} R(P_{aero} + P_{iner})\mathrm{d}t, \tag{2.13}$$

where $R(x)$ is a ramp function defined by

$$R(x) = \begin{cases} x & \text{if } x \geqslant 0, \\ \\ 0 & \text{if } x < 0. \end{cases} \tag{2.14}$$

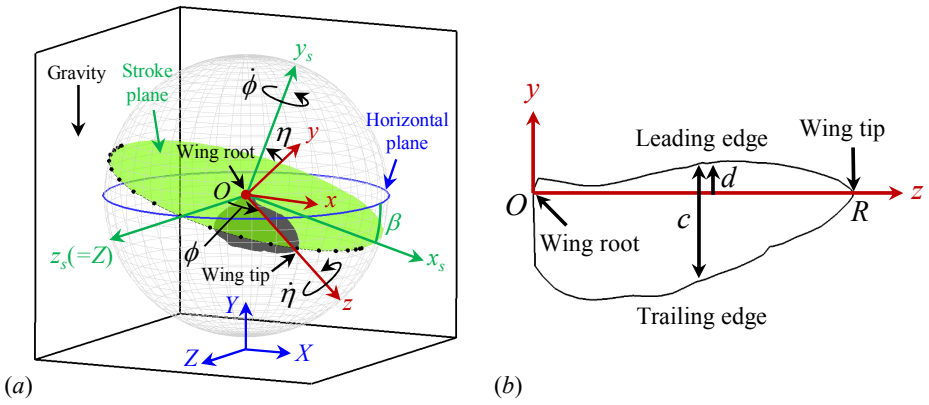

FIGURE 2.1. Definitions of the coordinates and parameters of (a) flapping wing motion and (b) planform shape. Note that we do not consider an offset of the wing root in the spanwise direction.

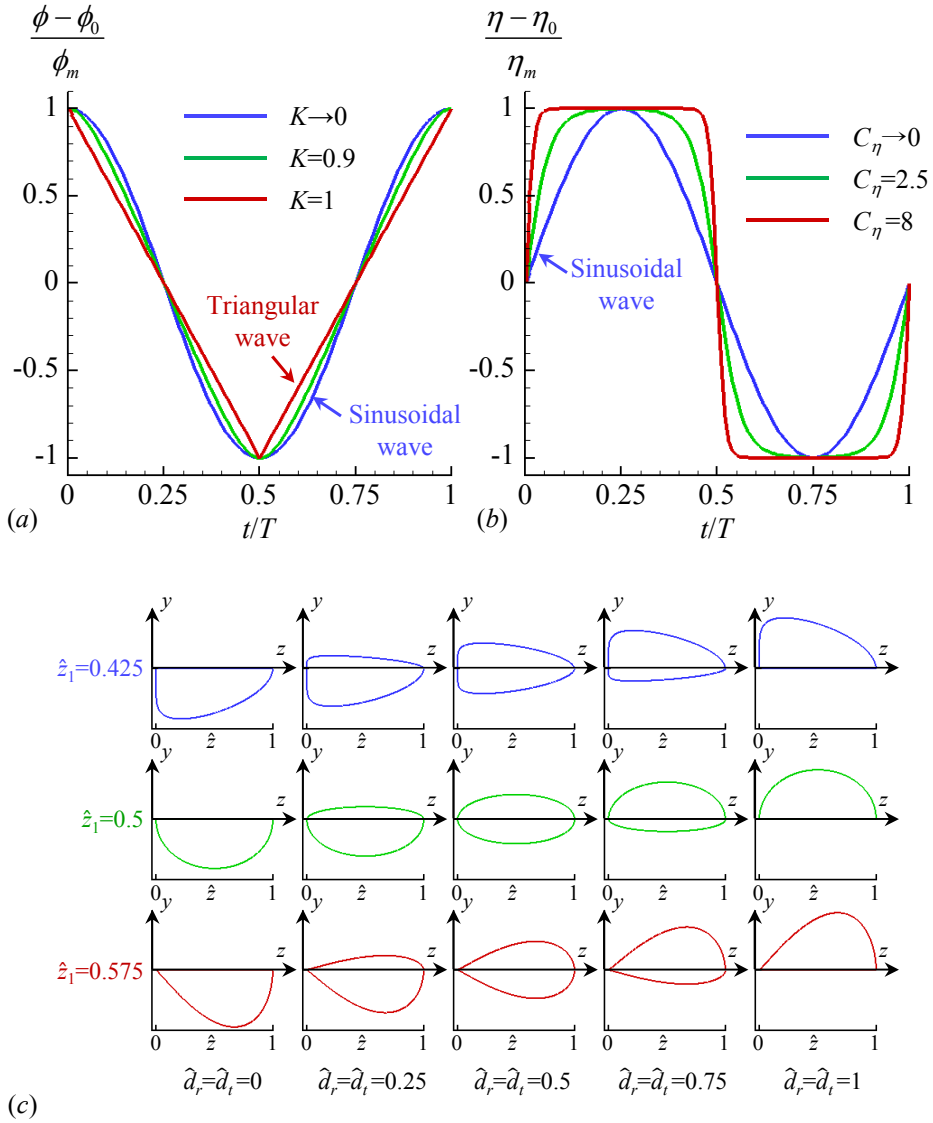

FIGURE 2.2. Effects of parameters on the wing motion and planform shape: (a) sweeping angles (ϕ) with different K; (b) pitching angles (η) with different C_η; (c) wing planform shapes with different $\hat{z}_1$, $\hat{d}_r$ and $\hat{d}_t$. In (b), lines are drawn with $\Phi_\eta = -\pi/2$.

Chapter 3

Optimization

In the present study, we separately explore the optimal wing motions for the measured wing shape (figure 2.1(b)) and the optimal wing shapes for the measured wing motion (figure 4.1), respectively.

First, we find two optimal wing motions which minimize the period-averaged aerodynamic (2.12) and positive mechanical (2.13) power consumptions, respectively. For convenience, these kinds of the optimal results will be referred to as the aerodynamically optimal (for the former) and mechanically optimal (for the latter), respectively. We fix ϕ_m to the measured value because the optimal ϕ_m for minimum power may be found at its upper boundary (Berman & Wang 2007; Nakata *et al.* 2015). The flapping frequency f is also fixed to the measured one in order to keep $U(= 4\phi_m f R)$ and the Reynolds number ($Re = U\bar{c}/\nu$) unchanged. Thus, seven kinematic parameters (ϕ_0, K, η_m, η_0, C_η, Φ_η, β) are considered in the optimizations of the wing motion.

Similarly, for the measured wing motion, we optimize wing shapes for minimum aerodynamic power and positive mechanical power, respec-

tively. The measured sweeping and pitching angles are connected by periodic quintic splines (Schurer 1968) to obtain smooth change of angular accelerations in time, as done by Oh *et al.* (2020). In the wing shape optimizations, we fix R and AR to the measured values to make the wing area (S) and the mean tip velocity (U) as well as the Reynolds number (Re) constant. Therefore, three geometric parameters ($\hat{r}_1$, $\hat{d}_r$, $\hat{d}_t$) are optimized for minimum power consumptions.

The optimal parameters are found under the following constraints:

(i) $\tilde{L} \geqslant 1$, where $\tilde{L} = 2\overline{F}_Y/W$, W(=58.21 mN) is the weight of the beetle (Oh *et al.* 2020) (see also table 2.1 in part I) and $\overline{F}_Y$ is the mean vertical force generated by a single wing. Thus, $2\overline{F}_Y$ is the total vertical force generated by a pair of wings under an assumption of no interactions between left and right wings. This inequality constraint was introduced by Berman & Wang (2007) for enough vertical force generation to support the weight of insect. Thanks to this constraint, the optimal wing motions and shapes have a high wing loading at least greater than that of the beetle because the wing area is fixed to the measured one.

(ii) The mean sectional lift in the absence of downwash motion ($w = 0$) is greater than or equal to zero, i.e. $\min(\overline{\mathrm{d}\boldsymbol{F}|_{w=0} \cdot \boldsymbol{e}_{y_s}}) \geqslant 0$. This constraint is introduced to explicitly obtain the spanwise distribution of the steady induced downwash motion ((5.33) in part I) which interacts with the wing in the hovering flight.

Also, we define the lower and upper boundaries of each parameter to consider the physical constraints. Boundary of ϕ_0 is limited so that the sweeping angle does not exceed $\pm\pi/2$. Note that the maximum sweeping

angle of the beetle (1.62, see table 4.1) is slightly larger than $\pi/2$. However, the deviation is not large, and thus the range of ϕ_0 is acceptable. The ranges of η_0 and η_m are chosen such that the leading edge is always above the stroke plane, i.e., $-\pi/2 \leqslant \eta \leqslant \pi/2$. Within the range of K, the waveform of sweeping angle varies from sinusoidal ($K \to 0$) to triangular ($K \to 1$). The waveform of pitching angle changes from sinusoidal ($C_\eta \to 0$) to square ($C_\eta \to \infty$) with the increase of C_η. To avoid excessive added mass force due to the pitching acceleration, we set the upper boundary of C_η to 8.6 which makes the duration of the wing pitch greater than about $0.1T$. The wing kinematic pattern changes from horizontal to vertical with the increase in β. The range of $\hat{z}_1$ is set from 0.4 to 0.6 because $\hat{z}_1$'s of typical insect wings are in this range (Ellington 1984*a*). Finally, the pitching axis is located at the leading edge, mid-chord and trailing edge when $\hat{d}_r = \hat{d}_r = 0$, 0.5 and 1 (Wang *et al.* 2017), respectively.

The used method for the optimizations is similar to that by Berman & Wang (2007). To efficiently find the global optimum, we use a clustering genetic algorithm (Milano & Koumoutsakos 2002) together with the method-of-moving-asymptotes algorithm (Svanberg 2002) in NLopt open-source library (Johnson 2018). For the initial population of the genetic algorithm, we use 500 parameter sets randomly chosen within the boundaries (table 4.1). The genetic algorithm makes the parameter sets converge to an area where the global optimum is likely to be found. Then, one of the parameter sets is chosen as the initial point for the gradient-based optimization.

	Lower boundary	Upper boundary
ϕ_0 [rad]	$\phi_m - \pi/2$	$\pi/2 - \phi_m$
K [1]	0	1
η_m [rad]	0	$\pi/2$
η_0 [rad]	$\eta_m - \pi/2$	$\pi/2 - \eta_m$
C_η [1]	0	8.6
Φ_η [rad]	$-\pi$	π
β [rad]	0	$\pi/2$
$\hat{z}_1$ [1]	0.4	0.6
$\hat{d}_r$ [1]	0	1
$\hat{d}_t$ [1]	0	1

TABLE 3.1. Lower and upper boundaries of wing parameters for optimization

Chapter 4

Results and discussion

4.1. Optimal wing motions for the measured wing shape

Table 4.1 shows the kinematic parameters for minimum $\overline{P}_{aero}$ and $\overline{P}^{+}_{mech}$ and those of best fit to the measured motion, and the resultant sweeping and pitching angles are plotted in figure 4.1. As shown in figure 4.1, there are qualitative agreements between the optimized wing motions and the measured one. The optimal stroke plane angles indicate a nearly normal hovering flight ($\beta \approx 0$), which are similar to the measured stroke plane angle ($\beta = 2.25°$). For the sweeping motion, the both optimal ϕ_0's are found at the lower boundary, i.e., $\phi_m - \pi/2 = -0.04$. It is observed that the aerodynamically optimal sweeping motion ($K = 0.05$) is more closer to the simple harmonic motion ($K \to 0$) than the mechanically optimal one ($K = 0.51$). For the pitching motion, the optimal pitching amplitudes (η_m) and offsets (η_0) are very close to the measured ones. The pitching offsets (η_0) are nearly zero and the amplitude of aerodynamically optimal pitching motion is slightly larger than that of mechanically optimal one. Large pitching amplitude of the aerodynamically optimal motion may be

due to the fact that an increase in the pitching amplitude results in low angles of attack and thus reduces aerodynamic power consumption. On the other hand, a larger pitching amplitude may require more inertial power. Therefore, a relatively small pitching amplitude ($\eta_m = 0.89$) is better to reduce mechanical power consumption. For C_η, a measure of how rapid the wing pitch reversal is, the mechanically optimal C_η is very close to the measured one whereas the aerodynamically optimal C_η is larger than the measured one. Finally, since the optimal phase shifts of the pitching motion are greater than $-\pi/2$, a rapid wing pitching motion occurs before each of stroke reversals ($\dot{\phi} = 0$), i.e., an advanced rotation (Dickinson *et al.* 1999) is preferred for minimum power consumption. Similar results were also reported by Ansari *et al.* (2008*a*) and Wang *et al.* (2017).

Figure 4.2 shows the vertical force ($C_{F_Y} = 2F_Y/\rho U^2 S$) and power ($C_{P_i} = 2P_i/\rho U^3 S$) coefficients of the wings with the optimal motions. As can be expected, it turns out that the both wing motions produce the total mean vertical forces ($2\overline{F}_Y$) as same as the weight of the beetle (58.21 mN) (Berman & Wang 2007; Nakata *et al.* 2015). Also, we find that $2\overline{P}_{aero}$ and $2\overline{P}^{+}_{mech}$ are 468.2 mW and 689.4 mW for the aerodynamically optimal wing motion and 488.3 mW and 630.7 mW for the mechanically optimal wing motion (see table 4.3), respectively. As shown in figures 4.2(a, b), the time-varying vertical force coefficients are similar to each other except for the ends of each half stroke. This difference is mainly due to different C_η of both motions. As mentioned above, since the optimal C_η for $\overline{P}_{aero}$ is larger than that for $\overline{P}^{+}_{mech}$, the pitching velocity of the aerodynamically optimal wing motion is faster than that of mechanically optimal one. This causes second peaks at the ends of half stroke in the

power coefficients (figure 4.2(c)) as well as the vertical force coefficient (figure 4.2(a)) which are not noticeable in the case of the mechanically optimal wing motion (figures 4.2(b) and 4.2(d)).

Although the optimal wing motions are qualitatively similar to the measured one, there are still discrepancies between the optimal angles and measured ones as shown in figure 4.1. For the sweeping angle, it seems that the differences mainly come from different sweeping offsets ($\phi_0 = -0.04$ for the optimal motions; $\phi_0 = 0.09$ for the measured motion). This is due to the limitation that the present model cannot capture the effect of ϕ_0 if $\beta = 0$. Note that there is no effect of ϕ_0 on F_x, F_y and power consumption (see §5 in part I) and ϕ_0 hardly affect on the vertical force since the optimal β's are nearly zero and thus the second term in (2.8) is also nearly zero. For the pitching motion, discrepancies may be due to the limitations of used kinematic model (2.2), e.g. unlike the measured motion, (2.2) cannot provide a wing pitching motion having local humps or different durations of upstroke and downstroke.

4.2. Optimal wing shapes for the measured wing motion

Figure 4.3 shows the wing shapes for minimum $\overline{P}_{aero}$ and $\overline{P}^{+}_{mech}$ and that of best fit together with the measured one. Unlike the cases of the optimal wing motions, two optimal wing shapes are quite different each other and the mechanically optimal shape is closer to the measured shape than the aerodynamically optimal one. In other words, the measured wing shape is not optimal in terms of aerodynamic power consumption. Table 4.2 shows the optimal geometric parameters and those of best fit to the measured wing shape. Both optimal $\hat{z}_1$'s are slightly larger than that of the measured one, and the aerodynamically optimal $\hat{z}_1$ is larger than the

mechanically optimal one. As a result, the wing area distributions of the optimal wing shapes are concentrated farther away from the wing root than that of the measured one.

It is noteworthy that there are differences in the locations of pitching axis of two optimal wing shapes. For minimum aerodynamic power, the pitching axis ($\hat{d}$) locates at between the 1/4-chord and the mid-chord points ($0.25 \leqslant \hat{d} \leqslant 0.5$). Together with $\hat{z}_1 = 0.50$, the wing shape becomes similar to an ellipse as shown in figure 4.3. On the other hand, the pitching axis of the mechanically optimal wing shape locates at between the leading edge and the 1/4-chord point ($0 \leqslant \hat{d} \leqslant 0.25$). With a relatively small $\hat{z}_1 (= 0.47)$, the wing shape is qualitatively similar to the measured one. Figure 4.4 shows the vertical force (C_{F_Y}) and power (C_{P_i}) coefficients from the optimal wing shapes with the measured wing motion. As for the cases of the optimal wing motions, the both optimal wing shapes can generate the mean vertical forces as same as the weight of the beetle. $2\overline{P}_{aero}$ and $2\overline{P}^{+}_{mech}$ are 418.9 mW and 695.7 mW for the aerodynamically optimal wing shape and 459.9 mW and 647.7 mW for the mechanically optimal wing shape (see table 4.3), respectively.

To visualize the structures of the vertical force generation and power expenditure and gain more insight into why the obtained wing shapes are indeed optimal, we calculate $\tilde{L}$, $\overline{C}_{P_{aero}}$ and $\overline{C}_{P^{+}_{mech}}$ for all ($\hat{r}_1$, $\hat{d}_r$, $\hat{d}_t$) within their boundaries (table 3.1). Figures 4.5(a-c) shows the structures of $\tilde{L}$, $\overline{C}_{P_{aero}}$ and $\overline{C}_{P^{+}_{mech}}$ over the entire domain, indicating that mean vertical force and power expenditures increase as $\hat{z}_1$ increases and $\hat{d}_r$ and $\hat{d}_t$ decrease. Since the wing area experiencing a fast speed is increased by the increase of $\hat{z}_1$, a larger $\hat{z}_1$ typically results in larger $\tilde{L}$, $\overline{C}_{P_{aero}}$ and $\overline{C}_{P^{+}_{mech}}$. Also, when the leading edge approaches to the pitching axis ($\hat{d}_r = \hat{d}_t = 0$),

the effect of the pitching motion on the force and power increases. Unlike the case of $\tilde{L}$, it is observed that the both power coefficients increase when ($\hat{r}_1$, $\hat{d}_r$, $\hat{d}_t$) approaches to (0.6, 1, 1), i.e. the trailing edge locates at the pitching axis, which is undesirable for increasing lift force generation as can be seen in figure 4.5(a).

Figures 4.6(a) and 4.6(b) show the contours of $\overline{P}_{aero}$ and $\overline{P}^{+}_{mech}$ on the iso-surface of $\tilde{L} = 1$. As clearly shown in figures, the present optimization method indeed found the global optima. It is noteworthy that geometric parameters for a lower power consumption are diagonally distributed over the surface. As shown in figure 4.6(a), the aerodynamically efficient geometric parameters are found roughly between $\hat{d}_t = -\hat{d}_r + 0.5$ and $\hat{d}_t = -\hat{d}_r + 1$. At this region, $\hat{z}_1$ is nearly constant with a value of 0.5. Also, if we define $\overline{d}(= 0.5(\hat{d}_r + \hat{d}_t))$ as a measure of how far the leading edge locates from the pitching axis on average, $0.25 \leqslant \overline{d} \leqslant 0.5$. This means that a wing with $\hat{z}_1 = 0.5$ having its pitching axis located between the 1/4-chord and the mid-chord points is favorable for a low aerodynamic power consumption. On the other hand, mechanically efficient geometric parameters are around at $0 \leqslant \overline{d} \leqslant 0.25$ with a $\hat{z}_1$ lower than 0.5 (figure 4.6(b)), i.e., it is better for the pitching axis to be located between the leading edge and the 1/4-chord point to reduce the positive mechanical power consumption.

4.3. Numerical simulation on the optimal wing motions and shapes

We also perform numerical simulations to validate the optimal results. Numerical details are described in §3 of part I. Figure 4.7 shows the vertical force and power coefficients of the optimal results from the

numerical simulation, together with those predicted by the aerodynamic model. Here, the inertial power coefficients $C_{P_{iner}}(= (\boldsymbol{I_w}\boldsymbol{\psi})^T\boldsymbol{\omega})$ are identical for both numerical simulation and aerodynamic model (see 2.11). As clearly shown in this figure, the vertical force and aerodynamic and positive mechanical power coefficients predicted by the aerodynamic model are in excellent agreements with those from the numerical simulation.

Table 4.3 summarizes the total vertical force generation, power expenditures and hovering efficiencies of the optimal wing motions and shapes as well as those from the measured wing motion and shape. Here, two types of hovering efficiencies ($\eta_i = \overline{C}_{F_Y}^{3/2}/(\sqrt{2\Phi AR\cos\beta}\,\overline{C}_{P_i})$), η_{aero} and η_{mech}, are considered, which are defined based on $\overline{C}_{P_{aero}}$ and $\overline{C}_{P^+_{mech}}$, respectively. As shown in this table, all vertical forces are comparable to the weight of the beetle. η_{aero} of the aerodynamically optimal wing shape and η_{mech} of the mechanically optimal wing motion are increased by 3.3% and 7.4%, respectively, as compared to those from the measured wing shape and motion. On the other hand, the hovering efficiencies decrease for the other cases. This is due to the limitations that the kinematic and geometric models used cannot provide the same wing shape and motion as the measured ones.

Ξ_k	minimizing $\overline{P}_{aero}$	minimizing $\overline{P}^{+}_{mech}$	best fit
f [Hz]		37.04	
ϕ_m [rad]		1.53	
ϕ_0 [rad]	-0.04	-0.04	0.09
K [1]	0.05	0.51	0.71
η_m [rad]	0.93	0.89	0.98
η_0 [rad]	0.01	0.01	0.04
C_η [1]	2.69	2.09	2.09
Φ_η [rad]	-1.30	-1.33	-1.46
β [rad]	0.02	0.02	0.04

TABLE 4.1. Kinematic parameters minimizing $\overline{P}_{aero}$ and $\overline{P}^{+}_{mech}$ and those of best fit to the measured wing motion.

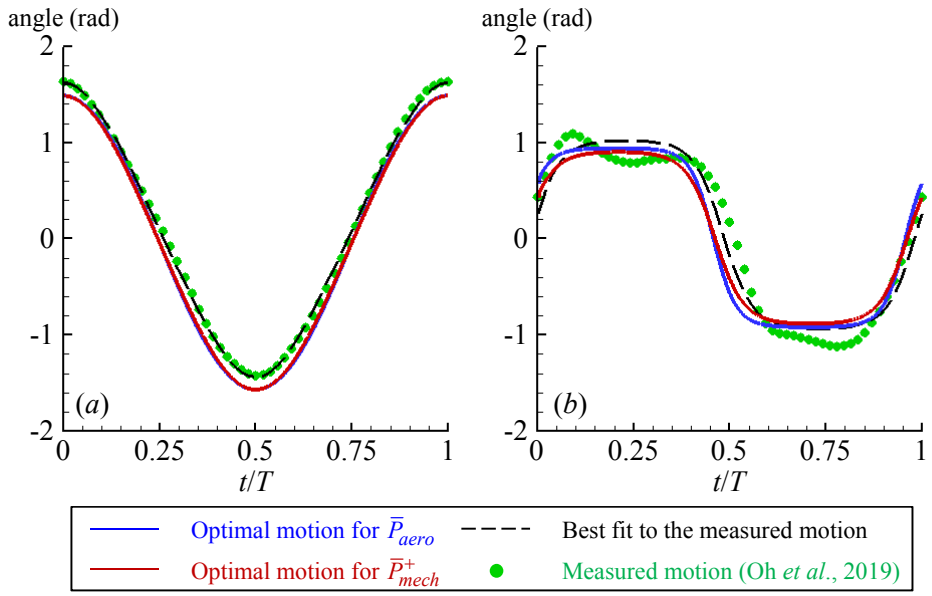

FIGURE 4.1. Comparison of the optimal wing motions with the measured motion at 60% wing length (Oh *et al.* 2020): (a) sweeping angle; (b) pitching angle. The sweeping and pitching angles of best fit to the measured ones are also provided.

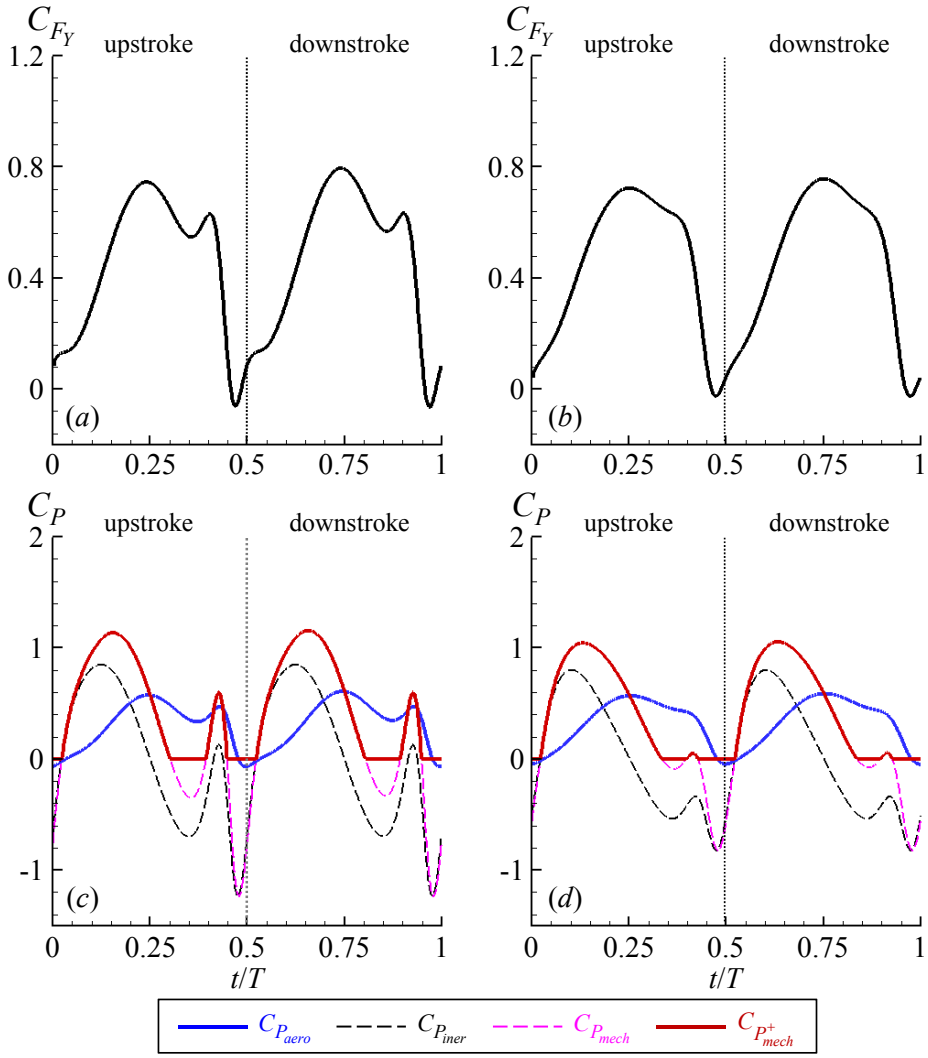

FIGURE 4.2. Vertical force and power coefficients of the wings with the optimal motions and the measured wing shape: (a, b) vertical force; (c, d) powers. Left, optimal for $\overline{P}_{aero}$; right, optimal for $\overline{P}^+_{mech}$.

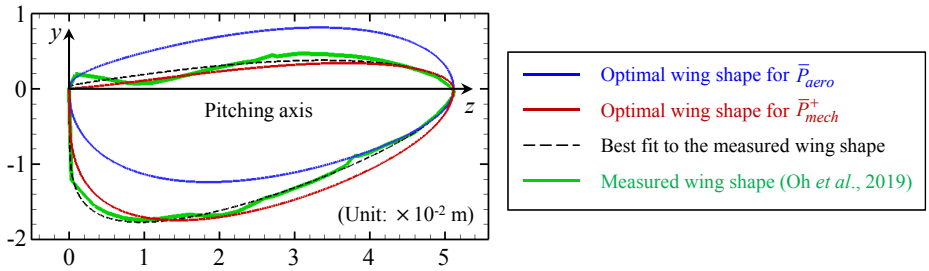

FIGURE 4.3. Comparison of the optimal wing shapes with the measured shape (Oh *et al.* 2020). The wing shape of best fit to the measured one is also plotted.

Ξ_g	minimizing $\overline{P}_{aero}$	minimizing $\overline{P}^{+}_{mech}$	best fit
R [mm]		51.2	
AR [1]		3.30	
$\hat{z}_1$ [1]	0.50	0.47	0.44
$\hat{d}_r$ [1]	0.27	0	0.03
$\hat{d}_t$ [1]	0.49	0.20	0.36

TABLE 4.2. Geometric parameters minimizing $\overline{P}_{aero}$ and $\overline{P}^{+}_{mech}$ and those of best fit to the measured wing shape.

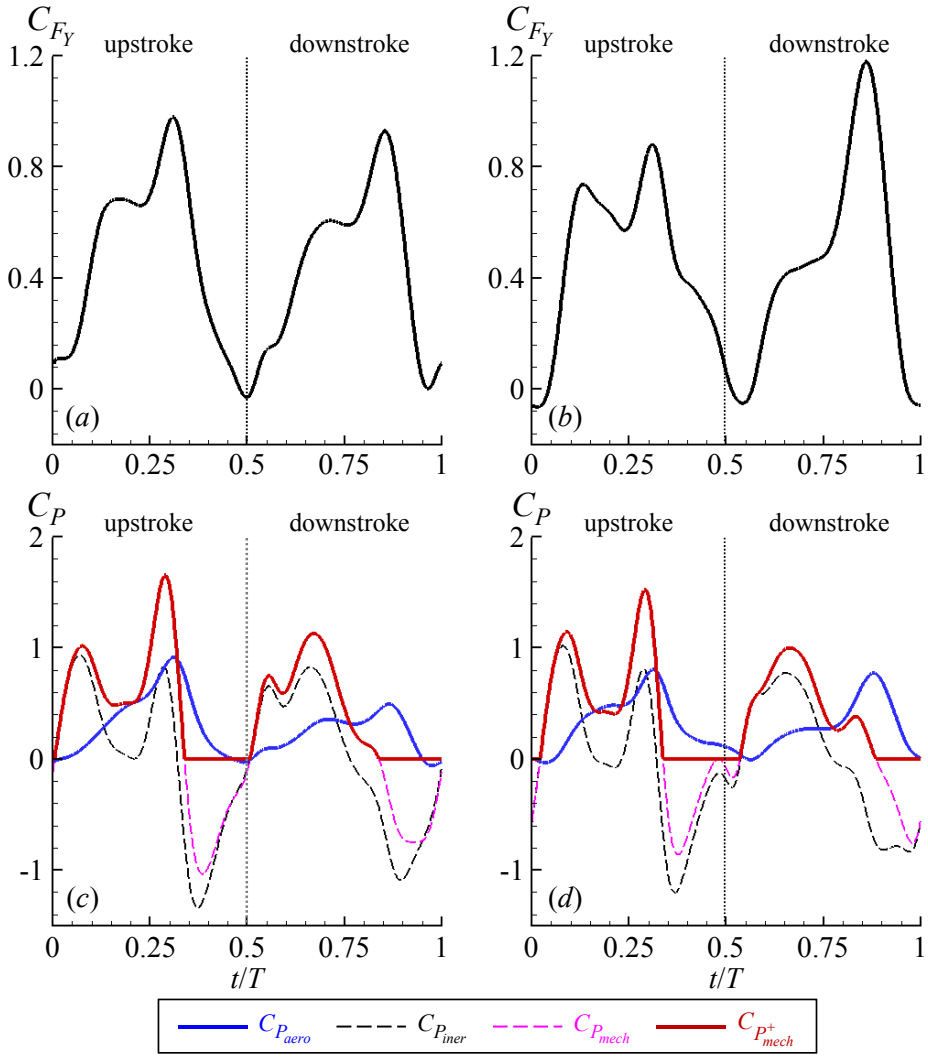

FIGURE 4.4. Vertical force and power coefficients from the optimal wing shapes and the measured wing motion: (a, b) vertical force; (c, d) power coefficients. Left, optimal for $\overline{P}_{aero}$; right, optimal for $\overline{P}^{+}_{mech}$.

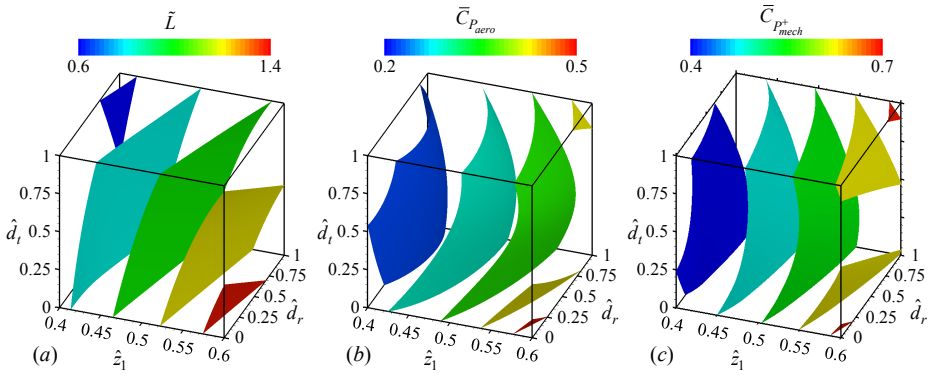

FIGURE 4.5. Iso-surfaces of (a) non-dimensional vertical force ($\tilde{L}$), (b) mean aerodynamic power coefficient ($\overline{C}_{P_{aero}}$) and (c) mean positive mechanical power coefficient ($\overline{C}_{P^+_{mech}}$).

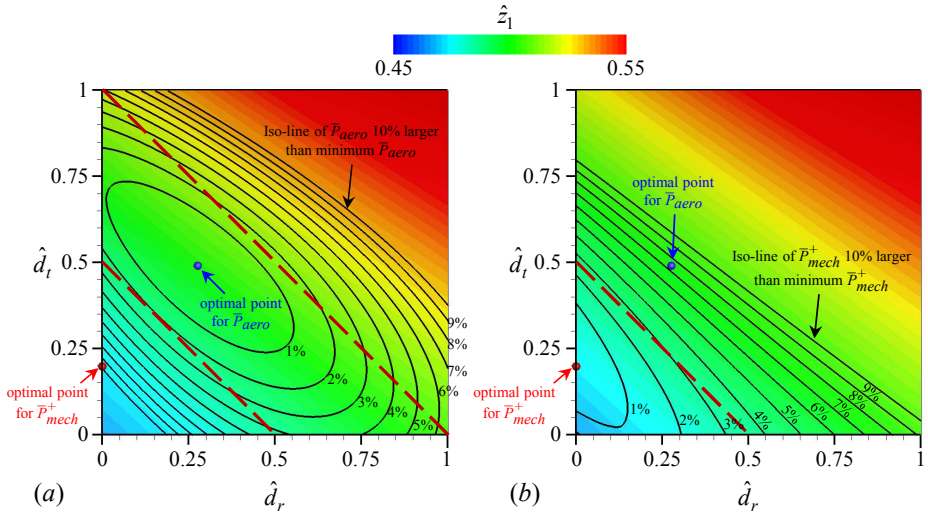

FIGURE 4.6. Power contours on the iso-surface of $\tilde{L} = 1$ coloured with $\hat{z}_1$: (a) $\overline{P}_{aero}$; (b) $\overline{P}^{+}_{mech}$. The optimal geometric parameters are shown as solid circles. Two dashed lines are $\hat{d}_t = -\hat{d}_r + 0.5$ and $\hat{d}_t = -\hat{d}_r + 1$, respectively.

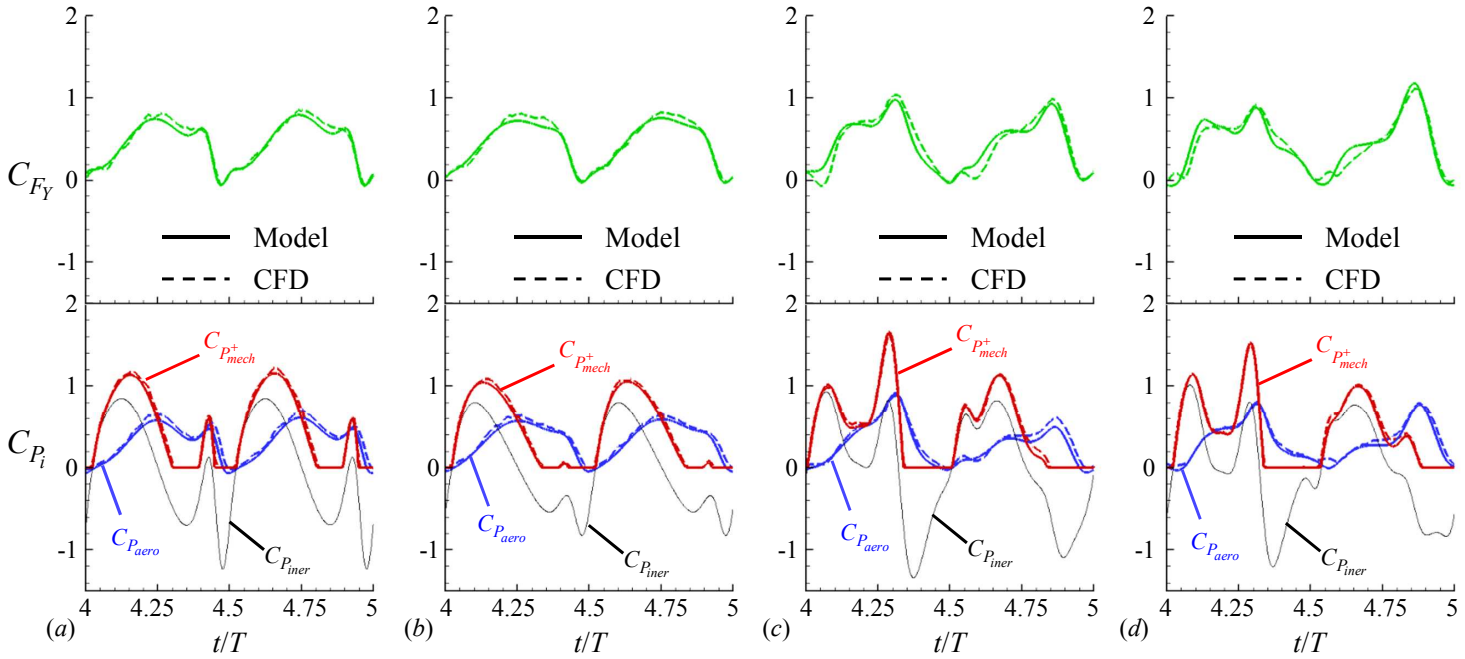

FIGURE 4.7. Vertical force and power coefficients of the optimal wing motions and shapes predicted by the aerodynamic model and those from numerical simulation (CFD): (a) aerodynamically optimal wing motion; (b) mechanically optimal wing motion; (c) aerodynamically optimal wing shape; (d) mechanically optimal wing shape. Top, vertical force coefficient; bottom, power coefficients. ——, model; – – –, CFD.

Motion	Shape	$2\overline{F}_Y$ [mN]	$2\overline{P}_{aero}$ [mW]	$2\overline{P}^{+}_{mech}$ [mW]	η_{aero}	η_{mech}
Aerodynamically optimal	Measured	60.5 (58.21)	547.3 (468.2)	737.6 (689.4)	0.196	0.145
Mechanically optimal	Measured	61.7 (58.21)	553.0 (488.3)	672.6 (630.7)	0.199	0.164
Measured	Aerodynamically optimal	58.6 (58.21)	477.1 (418.9)	718.9 (695.7)	0.214	0.142
Measured	Mechanically optimal	58.2 (58.21)	508.3 (459.9)	676.2 (647.7)	0.199	0.149
Measured		56.8	470.3	638.2	0.207	0.153

TABLE 4.3. Mean vertical force, power and figure of merit obtained from numerical simulation. Values in parentheses indicate those predicted by the aerodynamic model. Note that the weight of the beetle is 58.21 mN.

Chapter 5

Conclusion

In the present study, the optimal wing shapes and motions of a hovering rhinoceros beetle for minimum power consumption were investigated using a quasi-steady aerodynamic model together with a hybrid of a clustering genetic algorithm and a gradient-based optimizer. With the measured wing shape, we first found the optimal wing motions minimizing aerodynamic power and positive mechanical power, respectively. We showed that both optimal wing motions are close to the measured wing motion. Also, with the measured wing motion, we optimized wing shapes for minimum power consumptions, as done for the optimal wing motions. Optimization results indicated that the pitching axis of the aerodynamically optimal wing shape locates at between the 1/4-chord and the mid-chord points, which results in a wing shape similar to an ellipse with $\hat{z}_1 = 0.50$. On the contrary, the pitching axis of the mechanically optimal wing shape located at between the leading edge and the 1/4-chord point, and thus it resembled the measured wing shape with a relatively small $\hat{z}_1$. Combined with the results of the optimal wing motions, we showed that the wing

shape and motion of a hovering rhinoceros beetle are quite similar to the mechanically optimal ones.

Further investigation on the effects of wing geometric parameters indicated that the mean vertical force and both power expenditures increase as $\hat{z}_1$ increases and the leading edge approaches to the pitching axis. Also, we found that aerodynamically efficient wing shapes have $\hat{z}_1 \approx 0.5$ and the pitching axis is between the 1/4-chord and the mid-chord points. On the other hand, mechanically efficient wing shapes have a lower $\hat{z}_1$ than that of the aerodynamically efficient ones and the pitching axis is between the leading edge and the 1/4-chord point.

It should be emphasized that the optimal wing shapes and motions are for a hovering flight of a rhinoceros beetle. As pointed out by Ansari *et al.* (2008*b*), these may not be optimal for other flight modes. Therefore, some weighting may be required for the best overall flight performance. The present optimization method can be also used for finding the optimal parameters for other flight performances (e.g. lift-to-drag ratio, power loading). Therefore, the present approach can provide a guideline for the design of a FWMAV in hover with a high performance and also be a useful tool to understand the diversity of flapping wing motion and shape of flying insects.

References

Andersen, A., Pesavento, U. & Wang, Z. J. 2005 Unsteady aerodynamics of fluttering and tumbling plates. *J. Fluid Mech.* **541**, 65–90.

Ansari, S. A., Knowles, K. & Zbikowski, R. 2008*a* Insectlike flapping wings in the hover: part 1. effect of wing kinematics. *J. Aircr.* **45**, 1945–1954.

Ansari, S. A., Knowles, K. & Zbikowski, R. 2008*b* Insectlike flapping wings in the hover: part 2. effect of wing geometry. *J. Aircr.* **45**, 1976–1990.

Ansari, S. A., Zbikowski, R. & Knowles, K. 2006*a* Aerodynamic modelling of insect-like flapping flight for micro air vehicles. *Prog. Aerosp. Sci.* **42**, 129–172.

Ansari, S. A., Zbikowski, R. & Knowles, K. 2006*b* Non-linear unsteady aerodynamic model for insect-like flapping wings in the hover. part 1: methodology and analysis. *Proceedings of the Institution of Mechanical Engineers, Part G: Journal of Aerospace Engineering* **220**, 61–83.

Aono, H., Liang, F. & Liu, H. 2008 Near- and far-field aerodynamics in insect hovering flight: an integrated computational study. *J. Exp. Biol.* **211**, 239–257.

Berman, G. J. & Wang, Z. J. 2007 Energy-minimizing kinematics in hovering insect flight. *J. Fluid Mech.* **582**, 153–168.

Birch, J. M. & Dickinson, M. H. 2003 The influence of wing–wake interactions on the production of aerodynamic forces in flapping flight. *J. Exp. Biol.* **206**, 2257–2272.

Bomphrey, R. J., Nakata, T., Phillips, N. & Walker, S. M. 2017 Smart wing rotation and trailing-edge vortices enable high frequency mosquito. *Nature* **544**, 92–95.

Dickinson, M. H., Lehmann, F.-O. & Sane, S.P. 1999 Wing rotation and the aerodynamic basis of insect flight. *Science* **284**, 1954–1960.

Dickson, W. B. & Dickinson, M. H. 2004 The effect of advance ratio on the aerodynamics of revolving wings. *J. Exp. Biol.* **207**, 4269–4281.

Dudley, R. & Ellington, C. P. 1990 Mechanics of forward flight in bumblebee ii. quasi-steady lift and power requirements. *J. Exp. Biol.* **148**, 53–88.

Ellington, C. P. 1984*a* The aerodynamics of hovering insect flight: ii. morphological parameters. *Phil. Trans. R. Soc. Lond. B* **305**, 17–40.

Ellington, C. P. 1984*b* The aerodynamics of hovering insect flight: iii. kinematics. *Phil. Trans. R. Soc. Lond. B* **305**, 41–78.

Ellington, C. P. 1984*c* The aerodynamics of hovering insect flight: v. a vortex theory. *Phil. Trans. R. Soc. Lond. B* **305**, 115–144.

Ellington, C. P. 1984*d* The aerodynamics of hovering insect flight: vi. lift and power requirements. *Phil. Trans. R. Soc. Lond. B* **305**, 145–181.

Ellington, C. P. 1991 Aerodynamics and the origin of insect flight. *Advances in Insect Physiology* **23**, 171–210.

Ellington, C. P., van den Berg, C., Willmott, A. P. & Thomas, A. L. R. 1996 Leading-edge vortices in insect flight. *Nature* **384**, 626–630.

Fry, S. N., Sayaman, R. & Dickinson, M. H. 2005 The aerodynamics of hovering flight in drosophila. *J. Exp. Biol.* **208**, 2303–2318.

Garmann, D. J. & Visbal, M. R. 2014 Dynamics of revolving wings for various aspect ratios. *J. Fluid Mech.* **748**, 932–956.

Han, J.-S., Nguyen, A. T. & Han, J.-H. 2019 Aerodynamic characteristics of flapping wings under steady lateral inflow. *J. Fluid Mech.* **870**, 735–759.

Hatze, H. 1988 High-precision three-dimensional photogrammetric calibration

and object space reconstruction using a modified dlt-approach. *J. Biomechanics* **21**, 533–538.

Hedrick, T. L. 2008 Software techniques for two- and three-dimensional kinematic measurements of biological and biomimetic systems. *Bioinspir. Biomim.* **3**, 034001.

Ho, S., Nassef, H., Pornsinsirirak, N., Tai, Y. C. & Ho, C. M. 2003 Unsteady aerodynamics and flow control for flapping wing flyers. *Prog. Aerosp. Sci.* **39**, 635–681.

Jensen, M. 1956 Biology and physics of locust flight. iii. the aerodynamics of locust flight. *Phil. Trans. R. Soc. Lond. B* **239**, 511–5522.

Jeong, J. & Hussain, F. 1995 On the identification of a vortex. *J. Fluid Mech.* **285**, 69–94.

Jin, T., Goo, N. S., Woo, S.-C. & Park, H. C. 2009 Use of a digital image correlation technique for measuring the material properties of beetle wing. *J. Bio. Eng.* **6**, 224–231.

Johnson, S. G. 2018 The nlopt nonlinear-optimization package.

Johnson, W. 1994 *Helicopter theory*. Dover.

Ke, X., Zhang, W., Cai, X. & Chen, W. 2017 Wing geometry and kinematic parameters optimization of flapping wing hovering flight for minimum energy. *Aerosp. Sci. Technol.* **64**, 192–203.

Kim, J., Kim, D. & Choi, H. 2001 An immersed-boundary finite-volume method for simulations of flow in complex geometries. *J. Comp. Phys.* **171**, 132–150.

Kim, J., Kweon, J. & Choi, H. 2015 Sectional lift coefficient of a rotating wing at low reynolds number. *J. Mech. Sci. and Technol.* **29**, 4775–4781.

Kim, W., Lee, I. & Choi, H. 2018 A weak-coupling immersed boundary method for fluid–structure interaction with low density ratio of solid to fluid. *J. Comp. Phys.* **359**, 296–311.

Kweon, J. & Choi, H. 2010 Sectional lift coefficient of flapping wing in hovering motion. *Phys. Fluids* **22**, 071703.

Le, T. Q., Truong, T. V., Park, S. H., Truong, T. Q., Ko, J. H., Park, H. C. & Byun, D. 2013 Improvement of the aerodynamic performance by wing flexibility and elytra-hind wing interaction of a beetle during forward flight. *J. R. Soc. Interface* **10**, 20130312.

Lee, B., Park, H. & Kim, S.-T. 2015*a* Three-dimensional wing behaviors of a rhinoceros beetle during takeoff flights. *J. Mech. Sci. and Technol.* **29**, 5281–5288.

Lee, J., Choi, H. & Kim, H.-Y. 2015*b* A scaling law for the lift of hovering insects. *J. Fluid Mech.* **782**, 479–490.

Lee, J., Kim, J., Choi, H. & Yang, K.-S. 2011 Sources of spurious force oscillations from an immersed boundary method for moving-body problems. *J. Comp. Phys.* **230**, 2677–2695.

Leishman, J. G. 2006 *Principles of helicopter aerodynamics*. Cambridge University Press.

Lentink, D. & Dickinson, M. H. 2009 Rotational accelerations stabilize leading edge vortices on revolving fly wings. *J. Exp. Biol.* **212**, 2705–2719.

Lissaman, P. B. S. 1983 Low-reynolds-number airfoils. *Ann. Rev. Fluid Mech.* **15**, 223–239.

Liu, G., Dong, H. & Li, C. 2016 Vortex dynamics and new lift enhancement mechanism of wing-body interaction in insect forward flight. *J. Fluid Mech.* **795**, 634–651.

Luo, G. & Sun, M. 2005 The effects of corrugation and wing planform on the aerodynamic force production of sweeping model insect wings. *Acta Mech. Sin.* **21**, 531–541.

Meng, X. G., Xu, L. & Sun, M. 2011 Aerodynamic effects of corrugation in flapping insect wings in hovering flight. *J. Exp. Biol.* **214**, 432–444.

Messiter, A. F. 1970 Boundary-layer flow near the trailing edge of a flat plate. *SIAM J. Appl. Math.* **18**, 241–257.

Milano, M. & Koumoutsakos, P. 2002 A clustering genetic algorithm for cylinder drag optimization. *J. Comp. Phys.* **175**, 79–107.

Mueller, T. J. & DeLaurier, J. D. 2001 An overview of micro air vehicle aerodynamics fixed and flapping wing aerodynamics for micro air vehicle applications. *Progress in Astronautics and Aeronautics* **195**, 1–10.

Nabawy, M. R. A. & Crowther, W. J. 2014 On the quasi-steady aerodynamics of normal hovering flihgt part i: induced power factor. *J. R. Soc. Interface* **11**, 20131196.

Nakata, T., Liu, H. & Bomphrey, R. J. 2015 A cfd-informed quasi-steady model of flapping-wing aerodynamics. *J. Fluid Mech.* **783**, 323–343.

Oh, S. & Choi, H. 2018 A predictive model of the drag coefficient for a revolving wing at low reynolds number. *Bioinspir. Biomim.* **13**, 054001.

Oh, S., Lee, B., Park, H., Choi, H. & Kim, S. T. 2020 A numerical and theoretical study of the aerodynamic performance of a hovering rhinoceros beetle (*Trypoxylus dichotomus*). *J. Fluid Mech.* **885**, A18.

Osborne, M. F. M. 1951 Aerodynamics of flapping flight with application to insects. *J. Exp. Biol.* **28**, 221–245.

Park, H. & Choi, H. 2012 Kinematic control of aerodynamic forces on an inclined flapping wing with asymmetric strokes. *Bioinspir. Biomim.* **7**, 016008.

Pennycuick, C. J. 2008 *Modelling the flying bird*. Academic Press.

Phan, H. V., Truong, Q. T. & Park, H. C. 2017 An experimental comparative study of the efficiency of twisted and flat flapping wings during hovering flight. *Bioinspir. Biomim.* **12**, 036009.

Poelma, C., Dickson, W. B. & Dickinson, M. H. 2006 Time-resolved reconstruction of the full velocity field around a dynamically-scaled flapping wing. *Exp. Fluids* **41**, 213–225.

Polhamus, E. C. 1971 Predictions of vortex-lift characteristics by a leading-edge suction analogy. *J. Aircr.* **8**, 193–199.

Rayner, J. M. V. 1979 A vortex theory of animal flight: part 1. the vortex wake of a hovering animal. *J. Fluid Mech.* **91**, 697–730.

Sane, S. P. & Dickinson, M. H. 2002 The aerodynamic effects of wing ro-

tation and a revised quasi-steady model of flapping flight. *J. Exp. Biol.* **205**, 1087–1096.

Schlichting, H. & Truckenbrodt, E. A. 1979 *Aerodynamics of the airplane*. McGraw-Hill.

Schurer, F. 1968 A note on interpolating periodic quintic splines with equally spaced nodes. *J. Approx. Theory* **1**, 493–500.

Shyy, W., Aono, H., Kang, C.-K. & Liu, H. 2013 *An introduction to flapping wing aerodynamics*. Cambridge University Press.

Shyy, W., Lian, Y., Tang, J., Viieru, D. & Liu, H. 2008 *Aerodynamics of low Reynolds number flyers*. Cambridge University Press.

Siekmann, J. 1963 On a pulsating jet from the end of a tube, with application to the propulsion of certain aquatic animals. *J. Fluid Mech.* **15**, 399–418.

Spedding, G. R. & Lissaman, P. B. S. 1998 Technical aspects of microscale flight systems. *J. Avian Biology* **29**, 458–468.

Stewartson, K. 1968 On the flow near the trailing edge of a flat plate. *Proc. R. Soc. A* **306**, 275–290.

Sun, M. & Du, G. 2003 Lift and power requirements of hovering insect flight. *Acta Mechanica Sinica* **19**, 458–469.

Sun, M. & Tang, J. 2002 Lift and power requirements of hovering flight in drosophila virilis. *J. Exp. Biol.* **205**, 2413–2427.

Svanberg, K. 2002 A class of globally convergent optimization methods based on conservative convex separable approximations. *SIAM J. Optim.* **12**, 555–573.

Taha, H. E., Hajj, M. R. & Beran, P. S. 2014 State-space representation of the unsteady aerodynamics of flapping flight. *Aerosp. Sci. Technol.* **34**, 1–11.

Taha, H. E. & Rezaei, A. S. 2018 *Unsteady Viscous Lift Frequency Response Using The Triple Deck Theory*, pp. 2018–2038. AIAA.

Tennekes, H. 1996 *The simple science of flight: from insects to jumbo jets*. MIT Press.

Truong, Q. T., Nguyen, Q. V., Truong, V. T., Park, H. C., Byun, D. Y. & Goo, N. S. 2011 A modified blade element theory for estimation of forces generated by a beetle-mimicking flapping wing system. *Bioinspir. Biomim.* **6**, 036008.

Truong, T. Q., Phan, V. H., Park, H. C. & Ko, J. H. 2013*a* Effect of wing twisting on aerodynamic performance of flapping wing system. *AIAA Journal* **51**, 1612–1620.

Truong, T. V., Kim, J., Kim, M. J., Park, H. C., Yoon, K. J. & Byun, D. 2013*b* Flow structurs around a flapping wing considering ground effect. *Exp. Fluids* **54**, 1575.

Truong, T. V., Le, T. Q., Park, H. C. & Byun, D. 2017 Experimental and numerical studies of beetle-inspired flapping wing in hovering flight. *Bioinspir. Biomim.* **12**, 036012.

Usherwood, J. R. & Ellington, C. P. 2002*a* The aerodynamics of revolving wings i. model hawkmoth. *J. Exp. Biol.* **205**, 1547–1564.

Usherwood, J. R. & Ellington, C. P. 2002*b* The aerodynamics of revolving wings ii. propeller force coefficeints from mayfly to quail. *J. Exp. Biol.* **205**, 1565–1576.

Usherwood, J. R. & Lehmann, F.-O. 2008 Phasing of dragonfly wings can improve aerodynamic efficiency by removing swirl. *J. R. Soc. Interface* **5**, 1303–1307.

Vogel, S. 1967 Flight in drosophila. ii. variations in stroke parameters and wing contours. *J. Exp. Biol.* **46**, 383–392.

Wagner, H. 1925 Über die entstehung des dynamischen auftriebes von tragflügeln. *Z. Angew. Math. Mech.* **5**, 17–35.

Wan, H., Dong, H. & Gai, K. 2015 Computational investigation of cicada aerodynamics in forward flight. *J. R. Soc. Interface* **12**, 20141116.

Wang, Q., Goosen, J. F. L. & van Keulen, F. 2016 A predictive quasi-steady model of aerodynamic loads of flapping wings. *J. Fluid Mech.* **800**, 688–719.

Wang, Q., Goosen, J. F. L. & van Keulen, F. 2017 Optimal pitching axis location of flapping wings for efficient hovering flight. *Bioinspir. Biomim.* **12**, 056001.

Wang, Z. J., Birch, J. M. & Dickinson, M. H. 2004 Unsteady forces and flows in low reynolds number hovering flight: two-dimensional computations versus robotic wing experiments. *J. Exp. Biol.* **207**, 449–460.

White, F. M. 2006 *Viscous Fluid Flow*. McGraw-Hill.

Whitney, J. P. & Wood, R. J. 2010 Aeromechanics of passive rotation in flapping flight. *J. Fluid Mech.* **660**, 197–220.

Willmott, A. P. & Ellington, C. P. 1997 The mechanics of flight in the hawkmoth manduca sexta i. kinematics of hovering and forward flight. *J. Exp. Biol.* **200**, 2705–2722.

Willmott, A. P., Ellington, C. P. & Thomas, A. L. R. 1997 Flow visualization and unsteady aerodynamics in the flight of the hawkmoth manduca sexta. *Phil. Trans. R. Soc. B* **352**, 303–316.

Xia, X. & Mohseni, K. 2013 Lift evaluation of a two-dimensional pitching flat plate. *Phys. Fluids* **25**, 091901.

Zheng, L., Hedrick, T. L. & Mittal, R. 2013 A multi-fidelity modelling approach for evaluation and optimization of wing stroke aerodynamics in flapping flight. *J. Fluid Mech.* **721**, 118–154.

Appendix A

A predictive model of the drag coefficient for a revolving wing at low Reynolds number

A.1. Introduction

Recently, many military and civilian organizations have developed micro aerial vehicles (MAVs) for operations in hazardous conditions. They have small length and low velocity scales, and thus operate at low Reynolds numbers (Mueller & DeLaurier 2001; Ho *et al.* 2003). Insects have a great potential for the design of flapping MAVs because their dimensions, weights and flight conditions are similar to those of flapping MAVs. The flight of insects commonly involves a flapping motion of their wings, where the flapping motion is typically decomposed into translational and rotational motions. Therefore, the flapping flights of various species of insects, such as the fruit fly, mosquito, bumblebee and hawkmoth, have

This appendix is based on "**Oh, S.** & Choi, H. 2018 A predictive model of the drag coefficient for a revolving wing at low Reynolds number. *Bioinspir. Biomim.* **13**, 054001".

been investigated by numerous researchers (see, for example, Dudley & Ellington (1990), Willmott *et al.* (1997), Dickinson *et al.* (1999), Wang *et al.* (2004) and Bomphrey *et al.* (2017)). As a result, vortical structures, such as the attached leading edge vortex (LEV), and the trailing edge and wing tip vortices, have been found to be responsible for the generation of forces on flapping wings. Among them, LEV attached to the wing upper surface has been shown to be a predominant flow structure responsible for the lift generation during insect flights (Ellington *et al.* 1996; Dickinson *et al.* 1999). Ellington *et al.* (1996) suggested that lift augmentation due to the LEV attached on flapping wings is analogous to the vortex lift on delta wings because the structure of LEV on flapping wings is similar to that observed on highly swept delta wings. This vortex lift on highly swept delta wings was successfully modelled by Polhamus (1971) using an analogy with the leading edge suction associated with the potential flow.

Dynamically scaled wings revolving at a constant angular speed, albeit their motions are less realistic, have been commonly used to estimate the quasi-steady translational forces of flapping wings (Sane & Dickinson 2002; Berman & Wang 2007; Whitney & Wood 2010; Wang *et al.* 2016), in which the force due to the attached LEV was taken into account but those from rapid acceleration and pitching motions were not considered because the attached LEV is a robust characteristics for both revolving and flapping wings (Dickinson *et al.* 1999; Usherwood & Ellington 2002*a*,*b*; Dickson & Dickinson 2004; Lentink & Dickinson 2009). Wang *et al.* (2004) suggested a semi-empirical model for force coefficients of a revolving wing with an elliptic cross-section at a fixed angle of attack, taking into account the effect of attached LEV. However, their model re-

quired additional experiment or numerical simulation to determine the model constants therein. Recently, predictive models without requiring additional experimental or simulation data have been developed by a few research groups. Taha *et al.* (2014) derived a general formula for the maximum lift coefficient of a revolving wing based on extended lifting line theory and suggested a predictive model of the lift coefficient for a wide range of angles of attack. Furthermore, Wang *et al.* (2016) provided an aerodynamic model for the drag coefficient using the result of Taha *et al.* (2014), assuming that the resultant force is perpendicular to the wing chord line for all angles of attack. However, as pointed out by Wang *et al.* (2016), their model could not accurately predict the drag coefficient especially at low Reynolds number and low angles of attack, because the viscous drag was neglected. Hence, there is no accurate predictive aerodynamic model for a revolving wing operating at low angles of attack and low Reynolds numbers.

The objective of present study is to develop an improved aerodynamic model of the drag coefficient for a revolving wing at these operating conditions. First, we include the viscous drag in the present model using laminar boundary layer theory, called triple deck theory, to predict the viscous drag more accurately at low angles of attack and low Reynolds numbers. Second, using the lift model of Taha *et al.* (2014), we estimate the drag coefficient at an angle of attack where the resultant force on the wing is most perpendicular to the wing chord line. With these two modifications, we suggest an improved predictive model of the drag coefficient for a revolving wing from the semi-empirical model of Wang *et al.* (2004). To validate the present model, the drag coefficients predicted by the present model together with the lift model of Taha *et al.* (2014) are

compared with the experimental data of four different revolving wings, two *Drosophila melanogaster* (Dickinson *et al.* 1999; Dickson & Dickinson 2004), hawkmoth (Usherwood & Ellington 2002*a*), and bumblebee (Usherwood & Ellington 2002*b*) wings, having different aspect ratios and Reynolds numbers.

A.2. An improved model of the drag coefficient

The conventional definitions of the lift (C_L) and drag (C_D) coefficients on a wing revolving at a constant angular speed Ω are

$$C_L = \frac{2L}{\rho(R\Omega)^2 S\hat{r}_2^2}, \quad C_D = \frac{2D}{\rho(R\Omega)^2 S\hat{r}_2^2}, \tag{A.1}$$

where L and D are the lift and drag forces, ρ is the fluid density, R is the wing-tip radius from the rotating axis, and S is the wing planform area. $\hat{r}_2$ is a non-dimensional radius of the second moment of wing area defined by

$$\hat{r}_2 = \sqrt{\frac{1}{R^2 S}\int_{R-R_w}^{R} cr^2 \mathrm{d}r} = \sqrt{\frac{1}{\lambda}\int_{1-\lambda}^{1} \hat{c}\hat{r}^2 \mathrm{d}\hat{r}}, \tag{A.2}$$

where $\lambda = R_w/R$, $\hat{c} = c/\overline{c}$, $\hat{r} = r/R$, $S = \overline{c}R_w$, R_w is the wing root-to-tip length, c and r are the local chord length and radial distance from the rotating axis, and $\overline{c}$ is the mean chord length. The Reynolds number is defined as

$$Re = \frac{R\Omega\overline{c}}{\nu}, \tag{A.3}$$

where ν is the kinematic viscosity. The sectional drag coefficient is defined as

$$C_d = \frac{2\mathrm{d}D}{\rho(r\Omega)^2 c\mathrm{d}r}. \tag{A.4}$$

Several aerodynamic models have been suggested to predict the force coefficients of a revolving wing by including the effect of the attached

LEV, as mentioned previously. Dickinson *et al.* (1999) presented an empirical model for the lift and drag coefficients of a revolving fruit fly wing, *D. melanogaster*, as a harmonic function of the angle of attack

$$C_L = 0.225 + 1.58\sin(2.13\alpha - 7.20^\circ), \tag{A.5}$$

$$C_D = 1.92 - 1.55\cos(2.04\alpha - 9.82^\circ), \tag{A.6}$$

where α is the angle of attack (in degree). Wang *et al.* (2004) pointed out that the lift and drag coefficients of a wing with elliptic cross-section depend explicitly on 2α because 2α dependence is consistent with the symmetry of cross-section about its geometric centre. Thus, they suggested a semi-empirical model for the lift and drag coefficients of a revolving wing as follows:

$$C_L = A\sin 2\alpha, \tag{A.7}$$

$$C_D = B - C\cos 2\alpha, \tag{A.8}$$

$$\text{or} \quad C_D = C_D(0)\cos^2\alpha + C_D\left(\frac{\pi}{2}\right)\sin^2\alpha, \tag{A.9}$$

where A, B, C, $C_D(0)$ and $C_D(\pi/2)$ are model constants depending on the Reynolds number and wing geometry, and determined using experimental data. Berman & Wang (2007) determined the values of A, B, C, $C_D(0)$ and $C_D(\pi/2)$ from the data of *D. melanogaster* (Dickinson *et al.* 1999) and hawkmoth (Usherwood & Ellington 2002*a*) wings, respectively. However, (A.7)–(A.9) require additional experiments or simulations to determine A, B, C, $C_D(0)$ and $C_D(\pi/2)$ whenever the wing geometry or Reynolds number changes. In other words, the models (A.7)–(A.9) are not entirely predictive. Taha *et al.* (2014) presented a general formula for A in (A.7) based on the extended lifting line theory (Schlichting & Truckenbrodt

1979), and suggested the lift coefficient as

$$C_L = \pi \frac{AR}{\sqrt{AR^2 + 4} + 2} \sin 2\alpha, \tag{A.10}$$

where $AR(= R_w/\overline{c})$ is the wing aspect ratio. The lift coefficients obtained from (A.10) were in good agreements with experimental data for a range of angles of attack ($0^\circ \leqslant \alpha \leqslant 90^\circ$), showing that (A.10) is an excellent predictive model for the lift coefficient. Then, Wang *et al.* (2016) suggested a predictive model for the drag coefficient with the assumption that the resultant force on the wing is perpendicular to the wing chord line. Accordingly, the drag coefficient is given by

$$C_D = C_L \tan \alpha = 2\pi \frac{AR}{\sqrt{AR^2 + 4} + 2} \sin^2 \alpha. \tag{A.11}$$

They showed that (A.11) is in good agreements with the experimental results for a dynamically scaled hawkmoth wing ($AR = 2.83$, $Re = 8071$) (Usherwood & Ellington 2002*a*), but does not agree with the experimental ones for a dynamically scaled *D. melanogaster wing* ($AR = 3.74$, $Re = 136$) (Dickinson *et al.* 1999) because of the neglected viscous drag on the wing surface at low Reynolds number. Additionally, Wang *et al.* (2016) also pointed out that (A.11) overestimates the drag coefficient at $\alpha = \pi/2$.

Hence, we present an improved model by including the viscous drag. In Berman & Wang (2007), the model constants in the drag coefficient model (A.8) were determined by providing the magnitudes of the drag coefficient at $\alpha = 0$ and $\pi/2$ (A.9). In the present study, however, we provide the magnitudes of the drag coefficient at $\alpha = 0$ and $\pi/4$ (see below), which results in

$$C_D = C_D(0) \cos 2\alpha + 2C_D \left(\frac{\pi}{4}\right) \sin^2 \alpha. \tag{A.12}$$

To evaluate $C_D(0)$, we consider laminar viscous drag on a 2D flat plate having a finite chord length at zero angle of attack

$$C_d(0) = \frac{1.328}{\sqrt{Re_c}} + \frac{2.66}{Re_c^{7/8}}, \tag{A.13}$$

where $Re_c = r\Omega c/\nu$. The first term on the right hand side of (A.13) is the Blasius solution which is accurate for $Re_c \geqslant 1000$ but underestimates the drag coefficient for $1 < Re_c < 1000$ because of the effects from both leading and trailing edges at low Reynolds number (White 2006). To correct the underestimation at low Reynolds number, the second term was introduced from triple deck theory developed by Stewartson (1968) and Messiter (1970) (see also Taha & Rezaei (2018)). Considering the upper and lower surfaces of wing, the viscous drag coefficient becomes

$$C_d(0) = \frac{2.656}{\sqrt{Re_c}} + \frac{5.32}{Re_c^{7/8}}, \tag{A.14}$$

Then, the viscous drag acting on the entire wing is obtained as:

$$\begin{aligned} D(0) &= \int_{R-R_w}^{R} \frac{1}{2}\rho(r\Omega)^2 c C_d \mathrm{d}r \\ &= \frac{1}{2}\rho\Omega^2 \int_{R-R_w}^{R} cr^2 \left[2.656\sqrt{\frac{\nu}{r\Omega c}} + 5.32\left(\frac{\nu}{r\Omega c}\right)^{\frac{7}{8}}\right] \mathrm{d}r. \end{aligned} \tag{A.15}$$

With (A.15), the drag coefficient at $\alpha = 0$ becomes

$$C_D(0) = \frac{2D(0)}{\rho(R\Omega)^2 S\hat{r}_2^2} = \frac{1}{\lambda\hat{r}_2^2}\left(\frac{2.656}{\sqrt{Re}}\kappa_1 + \frac{5.32}{Re^{7/8}}\kappa_2\right), \tag{A.16}$$

where $\kappa_1 (= \int_{1-\lambda}^{1} \hat{c}^{1/2}\hat{r}^{3/2}\mathrm{d}\hat{r})$ and $\kappa_2 (= \int_{1-\lambda}^{1} \hat{c}^{1/8}\hat{r}^{9/8}\mathrm{d}\hat{r})$ are evaluated from the wing geometry.

If the resultant force on the wing is assumed to be perpendicular to the wing chord line, $C_D(\alpha) = C_L(\alpha)\tan\alpha$. To see if this assumption is valid, we consider four different revolving wings: two *D. melanogaster*

wings (AR = 3.74, Re = 136 (Dickinson *et al.* 1999); AR = 3.32, Re = 140 (Dickson & Dickinson 2004)), a hawkmoth wing (AR = 2.83, Re = 8071 (Usherwood & Ellington 2002*a*)), and a bumblebee wing (AR = 3.16, Re = 5496 (Usherwood & Ellington 2002*b*)). Figure A.1 shows the drag coefficients predicted by $C_D(\alpha) = C_L(\alpha)\tan\alpha$ and those by previous experiments for various angles of attack. For the *D. melanogaster* wings (figures A.1(a) and (b)), the agreements between the measured C_D (○) and $C_D = C_L\tan\alpha$ (▲) are very good around $\alpha = \pi/4$ but become poorer as α approaches 0 or $\pi/2$. The poor agreements are due to the neglect of viscous drag at $\alpha = 0$ for this low Reynolds number, and due to $\tan(\alpha = \pi/2) \to \infty$, respectively. On the other hand, for the hawkmoth (figure A.1(c)) and bumblebee (figure A.1(d)) wings, the agreements are very good at $\alpha = 0$ because the drag coefficient is very small for this relatively high Reynolds number flow, but become poorer with increasing α. As is clear in figure A.1, for both low and relatively high Reynolds number flows, the prediction by $C_D(\alpha) = C_L(\alpha)\tan\alpha$ is much better at $\alpha = \pi/4$ than at $\alpha = \pi/2$. Therefore, we theoretically obtain the force coefficient at $\alpha = \pi/4$ rather than that at $\alpha = \pi/2$: i.e. from (A.10) and $C_D(\alpha) = C_L(\alpha)\tan\alpha$, we obtain

$$C_D\left(\frac{\pi}{4}\right) = \pi\frac{AR}{\sqrt{AR^2+4}+2}. \tag{A.17}$$

Then, our model of the drag coefficient for a revolving wing consists of (A.12) together with (A.16) and (A.17):

$$C_D = \frac{1}{\lambda\hat{r}_2^2}\left(\frac{2.656}{\sqrt{Re}}\kappa_1 + \frac{5.32}{Re^{7/8}}\kappa_2\right)\cos 2\alpha + \frac{2\pi AR}{\sqrt{AR^2+4}+2}\sin^2\alpha. \tag{A.18}$$

A.3. Results and discussion

Table A.1 shows the values of λ, κ_1, κ_2, $\hat{r}_2^2$, Re, AR, $t/\overline{c}$ (ratio of wing thickness to mean chord), and $C_D(0)$ for all wings considered here. The values of λ, κ_1, and κ_2 are obtained by digitizing the pictures in Dickinson *et al.* (1999), Dickson & Dickinson (2004) and Usherwood & Ellington (2002*a*,*b*), respectively. For the *D. melanogaster* wings, the errors between predicted and measured $C_D(0)$'s are very small. For the hawkmoth and bumblebee wings, the predicted drag coefficients are almost zero like the measured ones because of relatively high Reynolds number. Hence, (A.16) is quite accurate in predicting the drag coefficient at zero angle of attack.

The drag coefficients, predicted by the present model (A.18), for various angles of attack are compared with the experimental ones in figure A.1, together with those by the predictive model (A.11) of Wang *et al.* (2016). The prediction performance of (A.18) at low Reynolds numbers is much better than that of (A.11) because of the inclusion of friction term in (A.18) (see figures A.1(a) and (b)). At high Reynolds numbers, the drag coefficients predicted by (A.11) and (A.18) are nearly the same, and agree with the experimental one for the hawkmoth wing (figure A.1(c)) but show some deviation at high angles of attack from the experimental one for the bumblebee wing (figure A.1(d)). The reason for this disagreement for the bumblebee wing is not clear. One of the possible reasons may be the way of obtaining the drag coefficient in Usherwood & Ellington (2002*b*): in this experiment, the drag coefficient was taken to be the same as the torque coefficient assuming that the sectional drag coefficient was constant along the wing span. However, it has been shown that the sectional lift coefficient is not constant along the span for revolving wings (Luo & Sun 2005; Garmann & Visbal 2014; Kim *et al.* 2015). If the resul-

tant force on the wing is assumed to be nearly perpendicular to the wing chord line, the sectional drag coefficient may also vary along the wing span.

Polar plots of the predicted and measured force coefficients of the two *D. melanogaster*, hawkmoth, and bumblebee wings, C_D versus C_L, are given in figure A.2. As shown, the present model (A.18) together with (A.10) accurately predicts the force coefficients of *D. melanogaster* and hawkmoth wings, but shows some deviation at high angles of attack for the bumblebee wing possibly due to the reason mentioned above.

A.4. Conclusion

In this study, we suggested an improved predictive model of the drag coefficient for a revolving wing operating at low Reynolds number, by considering the viscous drag on the wing and theoretical drag coefficient at the attack angle of $\pi/4$. We showed that the drag coefficients predicted by the present model for the two *D. melanogaster* ($AR = 3.74$, $Re = 136$; $AR = 3.32$, $Re = 140$), hawkmoth ($AR = 2.83$, $Re = 8071$), and bumblebee ($AR = 3.16$, $Re = 5496$) wings were in good agreements with those of previous experiments. Especially, the prediction of the drag coefficient at low Reynolds number was superior to those of previous models. The ranges of AR and Re investigated in the present study were $2.83 \leqslant AR \leqslant 3.74$ and $136 \leqslant Re \leqslant 8071$. According to Lentink & Dickinson (2009), typical AR's for insect wings cluster near 3. Therefore, the present predictive model (A.18) together with (A.10) by Taha *et al.* (2014) works for typical insect wings, at least for the range of Re considered here. The present model does not require additional measurement or numerical simulation to determine model constants once the wing geometry and angular speed

are specified. Therefore, the present model can be used to optimize the motion and geometry of revolving wings for enhancing their aerodynamic performances.

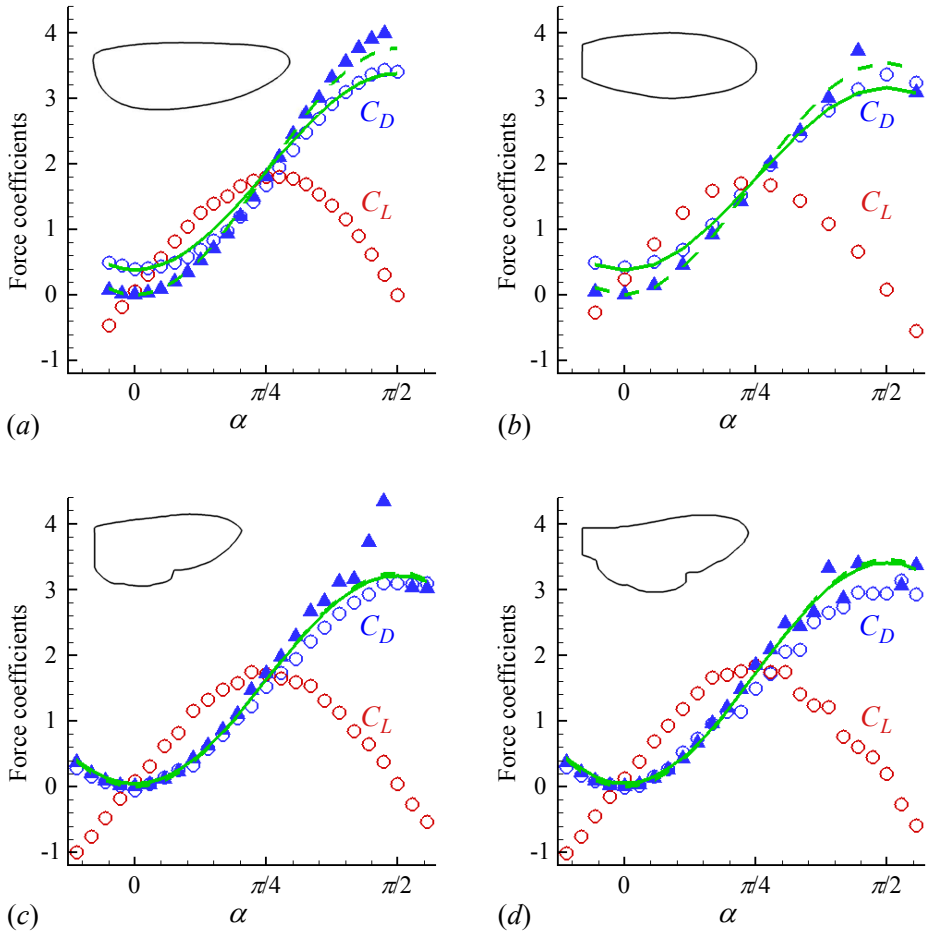

FIGURE A.1. Measured and predicted drag coefficients together with measured lift coefficients: (a) *D. melanogaster* wing ($AR = 3.74$, $Re = 136$) (Dickinson *et al.* 1999); (b) *D. melanogaster* wing ($AR = 3.32$, $Re = 140$) (Dickson & Dickinson 2004); (c) hawkmoth wing ($AR = 2.83$, $Re = 8071$) (Usherwood & Ellington 2002*a*); (d) bumblebee wing ($AR = 3.16$, $Re = 5496$) (Usherwood & Ellington 2002*b*). ○, measured C_L; ○, measured C_D; ▲, $C_D = C_L \tan\alpha$; – – –, (A.11) (Wang *et al.* 2016); ——, (A.18) (present model). Wing planform shapes are also plotted in this figure.

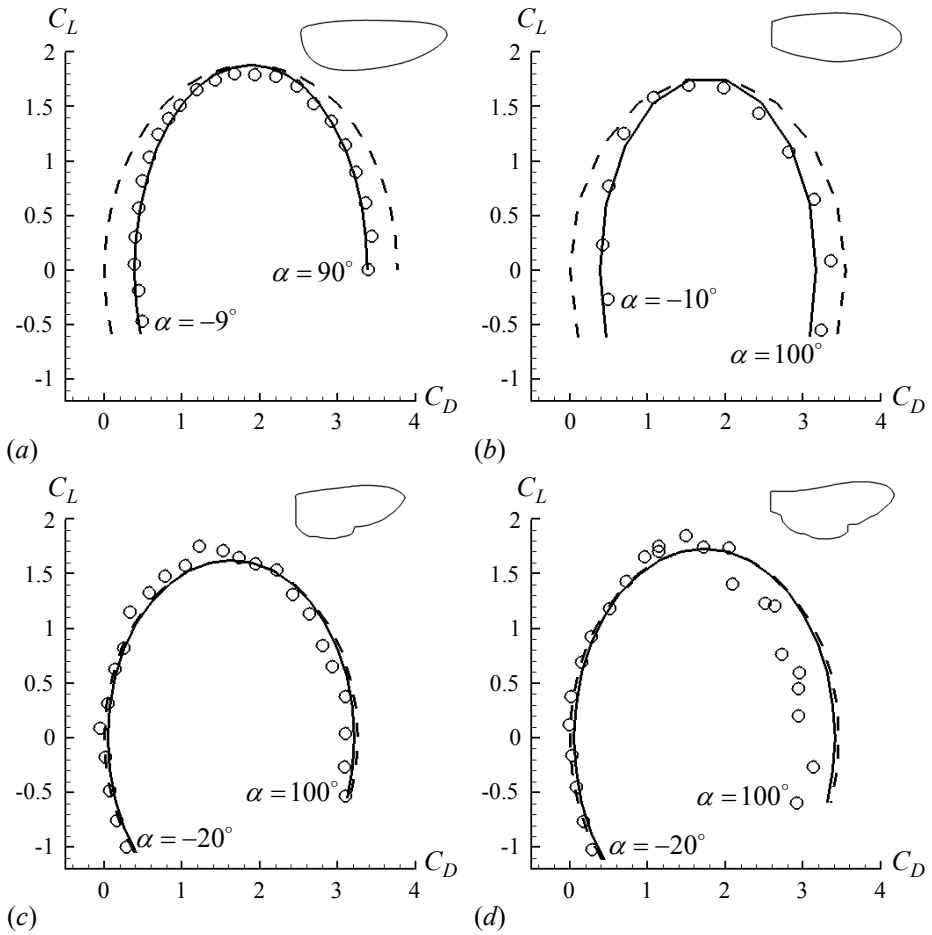

FIGURE A.2. Polar plots of the force coefficients: (a) and (b) *D. melanogaster* wings; (c) hawkmoth wing; (d) bumblebee wing. ——, (A.10) (Taha *et al.* 2014) and (A.18) (present model); – – –, (A.10) (Taha *et al.* 2014) and (A.11) (Wang *et al.* 2016); ○, measured by Dickinson *et al.* (1999) in (a), Dickson & Dickinson (2004) in (b), Usherwood & Ellington (2002*a*) in (c), and Usherwood & Ellington (2002*b*) in (d). Wing planform shapes are also plotted in this figure.

Wing	λ	κ_1	κ_2	$\hat{r}_2$	Re	AR	$t/\overline{c}\,(\%)$	$C_D(0)$ Predicted by (A.16)	$C_D(0)$ Measured
D. melanogaster (Dickinson *et al.* 1999)	0.75	0.37	0.44	0.63	136	3.74	4.79	0.3868	0.3909
D. melanogaster (Dickson & Dickinson 2004)	0.89	0.38	0.46	0.59	Approx. 140	3.32	3.42	0.3830	0.4245
Hawkmoth (Usherwood & Ellington 2002*a*)	0.90	0.36	0.45	0.55	8071	2.83	1.56	0.0428	-0.0503
Bumblebee (Usherwood & Ellington 2002*b*)	0.90	0.38	0.46	0.58	5496	3.16	1.74	0.0495	-0.0087

TABLE A.1. Wing characteristics, and predicted and measured drag coefficients at $\alpha = 0$ for four different wings.

정지 비행하는 장수풍뎅이 주변의 유동 특성: 모델링 및 최적화

서울대학교 대학원
기계항공공학부
오 세 형

요 약

정지 비행하는 장수풍뎅이의 공기 역학적 특성을 수치적-이론적으로 조사하였다. 날갯짓은 고속 카메라를 통해 측정되었으며, 정지 비행하는 장수풍뎅이 주변의 유동을 수치해석하는 데 사용되었다. 수치해석 결과는 준주기적 상태일 때 속날개로부터 발생되는 힘(특히 양력)과 공기 역학적 요구전력이 첫 번째 날갯짓 동안의 힘 및 공기 역학적 요구전력과 상당히 다르다는 것을 보여준다. 이는 날개-후류 간 상호작용이 준주기적 상태동안 속날개의 공력 특성에 크게 영향을 미친다는 것을 나타낸다. 또한 속날개의 날개 길이 방향에 따른 비틀림은 편평한 속날개와 비교할 때 전체 힘 생성에 크게 기여하지 않으며 공기 역학적 성능에 대한 겉날개와 몸통의 역할은 적어도 현재의 정지 비행에 대해 매우 작음을 확인하였다. 기존의 공력 모델을 바탕으로 날개-후류 간 상호작용의 효과를 고려하여 정지 비행하는 편평한

속날개에 대해 어떠한 모델 상수도 없는 개선된 예측적 공력 모델을 제안하였다. 이 공력 모델에서 후류를 비균일의 정상 또는 비정상 하강기류로 간주하고, 준정상 블레이드 요소 이론과 비점성 운동량 이론을 결합하여 후류의 세기를 구하였다. 현재의 공력 모델로 예측된 양, 항력 및 공기 역학적 요구전력은 수치해석으로부터 얻어진 결과와 매우 잘 일치하였다.

개발된 준정상 공력 모델을 기반으로, 최소 전력 소비를 위한 정지 비행하는 장수풍뎅이 속날개의 최적 평면 형상 및 움직임을 조사하였다. 먼저, 최소 공기 역학적 및 양의 기계적 전력 소비를 위해 측정된 날개 평면 형상으로 날개 움직임을 최적화하였다. 또한 날개 움직임의 최적화를 위해 수행된 것 처럼 측정된 날개 움직임으로 날개 평면 형상을 최적화하였다. 최적화 결과로부터 측정된 날개 형상은 공기 역학적 요구전력 측면에서 최적이 아니며, 양의 기계적 전력 소비를 최소화하는 날개 모양과 움직임이 측정된 것들에 가깝다는 것을 확인하였다. 최소 공기 역학적 전력 소비를 위해서는 날개 면적의 첫 번째 모멘트의 반경은 약 0.5이며, 날개의 피칭 축이 시위 길이의 1/4 지점과 1/2 지점 사이에 있어야함을 확인하였다. 최소 양의 기계적 전력 소비를 위해서는 최소 공기 역학적 전력 소비를 위한 날개보다 날개 면적이 날개 뿌리 근처에 모여있어야하며, 피칭 축은 선단과 시위 길이의 1/4 지점 사이에 있어야함을 확인하였다.

주요어: 장수풍뎅이, 정지 비행, 수치해석, 준정상 블레이드 요소 운동량 이론, 날개-후류 간 상호작용, 최적화

학 번: 2014-21560